Investigation of an ECR Plasma Thruster and Plasma Beam Interactions with a Magnetic Nozzle

Thesis by
David A. Kaufman

In Partial Fulfillment of the Requirements
for the Degree of
Doctor of Philosophy

California Institute of Technology
Pasadena, California
1995
(Submitted September 12, 1994)

Acknowledgments

Lots of people helped make my time at Caltech a great experience. To everyone I mention here and to more I don't, thanks. I don't think I would have made it without the support and distraction provided by my friends.

First, to Elizabeth, you are the most important part of my life. Without you I don't what I'd do, but I know I certainly wouldn't be having so much fun. I look forward to our future adventures together. To Mom, thank you for all the love and support you gave me growing up. Your encouragement and belief in me made anything seem possible. Thanks to Super Nick Glumac. With you for an office mate, I broke several ordinances for laughing more than the law allows. To Dave Goodwin, I appreciate your guidance as my research advisor not only in technical subjects but in the whole process of becoming a scientist. I think I'm a better engineer because of you.

Lots of friends have made Caltech a fun place to be for five years. One of the hardest parts of grad school is seeing everyone take off for different parts of the country. Thanks to Jim and Maria Mason, Kevin Otto, Ginger Sturcken, Don Kendrick, John Blandino, and Stephanie Leifer. I'm also thankful for the friends who are staying: Nancy and Elana Goldheimer, Steve Fryer and Craig Martinelli.

I had the opportunity to do some of my research in the electric propulsion laboratory at JPL. The people there were great to work with. Thanks to Joel Sercel for getting this work started and being a valuable resource for my research. Thanks in no particular order to Bill Thogmartin, Lew Pless, Al Owens, Bob Toomath, Raul Perez, John Brophy, Chuck Garner, Keith Goodfellow, Jay Polk, Juergen Mueller, and John Anderson.

Finally I would like to thank Kim West, all of the RA's, the Residence Life staff, and the undergrads of Marks and Braun. Being part of such a great bunch of people makes it very hard to leave.

Abstract

The results of an experimental study of an electrodeless electric propulsion device using electron cyclotron resonance (ECR) heating for plasma production are presented. The effects of pressure, propellant flow rate, and microwave input power on the plasma properties were examined. In addition, the effect of a magnetic nozzle on a plasma beam were examined experimentally and computationally.

A laboratory ECR thruster was operated with argon propellant in a vacuum tank at pressures in the 10^{-5} torr range using a 2.115 GHz microwave beam at power levels up to several kilowatts. Several movable plasma diagnostics were used to measure the spatial variation of various plasma properties in the plume of the thruster.

At low pressures, ion flux profiles showed an unexpected annular plasma plume with a depressed ion flux along the thruster axis. The ion energy measurements indicate that the ion kinetic energy is invariant with input microwave power. However, increases in pressure cause the plasma to lose kinetic energy due to friction with the background neutrals in the vacuum tank. Propulsion parameters were calculated from the ion flux and energy data. The results are greatly affected by additional ion flux due to entrainment of the background gas. The plasma potential and electron temperature both decreased with increasing pressure in the tank but were invariant with changes in microwave power. Microwave power reflected from and transmitted through the ECR region was measured and the results indicate that inefficient absorption may contribute significantly to energy losses in the laboratory device.

Plasma detachment from the magnetic nozzle was identified as a critical issue for ECR and other applied-field thrusters. A collisionless model was used to calculate the trajectories of plasma rings in a magnetic nozzle. The code predicted that the plasma will detach under certain conditions and that the acceleration due to the force on the dipole moments of the electrons is inconsequential to the plasma trajectories. The radii of 90° deflection were calculated for several plasma initial conditions, and it was shown that the nozzle configuration can be manipulated to reduce beam divergence

and increase the useful radius of the thruster.

An attempt was made to experimentally examine detachment using an ion thruster in an applied magnetic nozzle. The magnetic field could then be varied independent of the ion energy. The grids of the thruster were masked to extract a thin ring of plasma coaxial with the magnetic nozzle, and the ion flux density profile was measured to determine the effect of the magnetic field on the trajectory of the annular plasma. A radial electric field was established in presence of the magnet nozzle that caused the annulus to spread and decrease in radius making detachment unobservable. It is believed that the magnetic field inhibited neutralization of the ion beam causing the electric field to develop.

Contents

List of Figures

Chapter 1

Introduction

1.1 Motivation and the ECR Concept

Electric propulsion offers several advantages over conventional chemical propulsion which make it an attractive option for some space thrust applications. The primary advantage of electric propulsion is that the energy imparted to the propellant is not limited to the energy available in the chemical reaction between the fuel and oxidizer. Examples of three different classes of electric thrusters are shown in Figure 1-1 [1]. While the devices differ in the methods of accelerating the propellant, the common goal is to transfer energy from an external power supply to the kinetic energy of the propellant gas. Since the exhaust gas attains a higher velocity than attained in a chemical rocket, more thrust is produced for a given mass of fuel. Specific impulse ranges for three types of electric thrusters are shown in Figure 1-2 [1] as a function of input power. Approximate performance requirements are also shown in the figure for several missions. With a higher specific impulse, an electric rocket can accomplish the same mission with less fuel, allowing larger operational payloads and longer mission life for the same total spacecraft mass. Because of the enormous weight savings for electric propulsion, many believe that it is the only real option for long, manned space missions such as the proposed voyage to Mars [27].

Since electric rockets have a single propellant, fuel system mass is reduced because

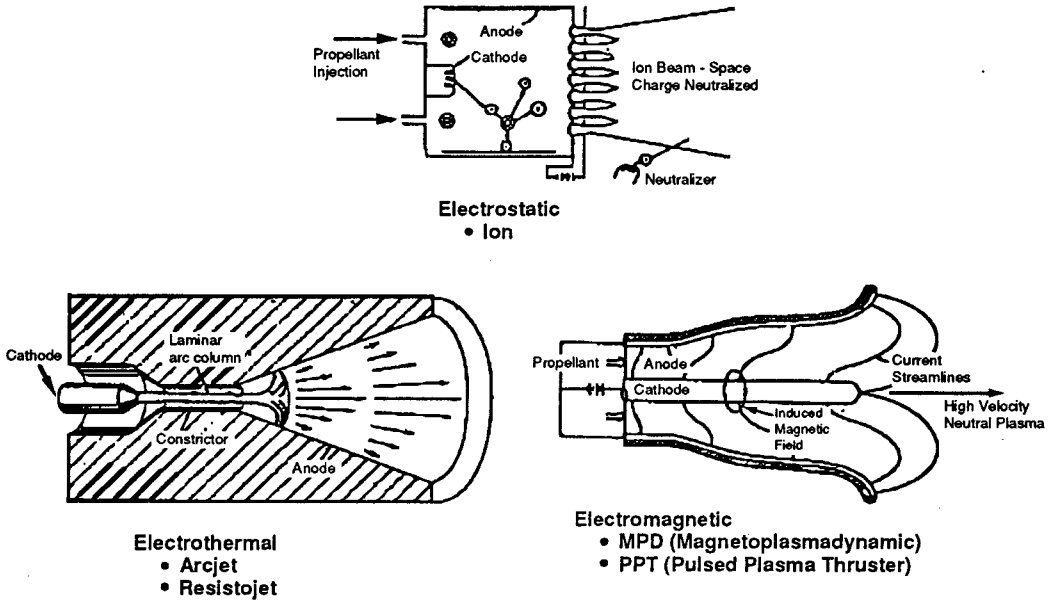

Figure 1-1: Examples of electric propulsion thrusters.

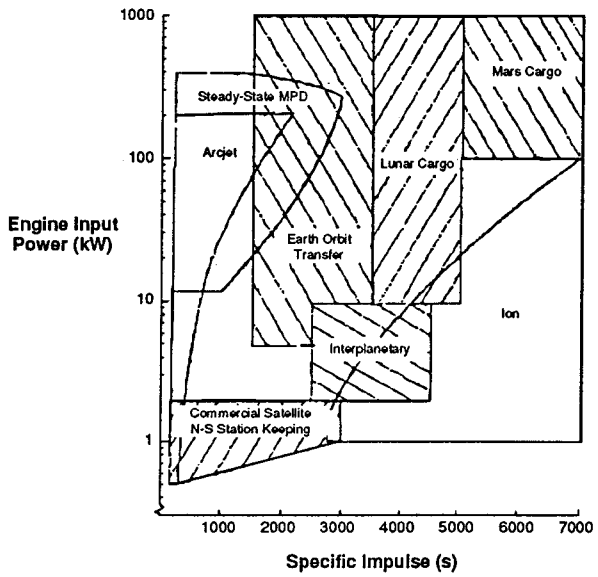

Figure 1-2: Demonstrated electric propulsion engine performance levels with major mission application regions.

only one set of fuel delivery ducts is necessary instead of one each for fuel and oxidizer in the liquid chemical rockets typically used on satellites. The stable propellants used in electric propulsion devices, often noble gases, are easily stored and safe to transport. The recent loss of the Mars Observer, which was apparently due to an explosion caused by inadvertently mixing fuels, is a dramatic demonstration of the advantage of monopropellant thrusters.

One disadvantage of electric propulsion is the need for an auxiliary power supply to run the thruster. If the added mass of the power supply is greater than the mass savings in fuel, electric propulsion will not be an attractive alternative to chemical propulsion. For some applications, such as geosyncronous communications satellites, extra weight can be minimized by utilizing the existing power supplies needed for the transmitters. Station-keeping thrusters operate only periodically, so the power normally reserved for communications can be briefly diverted to electric thrusters [22].

Even with decades of research [42] and the benefits mentioned above, until recently electric propulsion devices had only limited actual flight time on spacecraft. Simple resistojets are still the only electric thrusters in widespread use in the West. However, flight programs in the former Soviet Union show great promise for the Stationary Plasma Thruster (SPT) with over fifty SPT's having flown on Soviet spacecraft [5].

The success of these projects is partly responsible for recent increased interest in electric propulsion. In December 1993 the first advanced electric propulsion system used on a commercial communications satellite was launched by Martin Marietta [3]. Twelve hydrazine arcjets built by Olin Aerospace Corp. are used on an AT&T Telstar 401 satellite for attitude control and station keeping. The Institute for Spaceflight Systems (University of Stuttgart) has developed a 0.7 kW ammonia arcjet which will provide primary propulsion for a radio amateur satellite. A German RF Ionization Thruster was tested in 1993 on EURACA 1, the European space test platform. In the U.S., NASA is working on ammonia arcjets for the Electric insertion Transfer Experiment and Xenon Ion engines for the Solar Electric Propulsion Technology Application

Readiness program [2].

There are several reasons why electric thrusters have not been more widely used on spacecraft. Because of the size of the power supplies, extremely high-power thrusters are not feasible; this means that thrust levels are necessarily low. Low thrust means that trip times are longer than for other thrusters. For example, electric thrusters would take a few months in a spiral path to move a satellite from low earth orbit to geosynchronous orbit while a chemical rocket would take only a few hours [40]. For communications satellites, radiation from the high energy plasma may interfere with RF transmissions rendering the satellites unusable during rocket discharge. Another drawback is the size and weight of the power system. A high-power thruster would need a large, heavy solar array or a nuclear reactor with the associated contamination risks during launch and orbit [41]. In addition, using solar energy would be difficult for missions to the outer planets due to the decrease in solar power density [22].

One problem that limits the life of many electric propulsion devices is erosion of the electrode. The metal surfaces in contact with the plasma degrade over time from melting or sputtering. In addition, the erosion process degrades the performance of the thruster. For instance, as the grids in an ion engine erode, the shapes of the holes change. This leads to more ions impinging on the grid, reducing the number that are accelerated as intended and increasing the divergence angle. Even in the absence of an actual structural failure, erosion can incapacitate a thruster, since small flakes of sputtered metal can form an electric short across the electrodes. Plating of the sputtered electrode material can also be a problem for the spacecraft itself. Even a thin layer of metal coating a solar panel will greatly reduce its power output.

The problems associated with the electrodes provide some of the motivation for investigating electron cyclotron resonance (ECR) thrusters. A schematic of an ECR thruster is shown in Figure 1-3. A microwave beam is used to ionize and energize a gas in a magnetic nozzle. In the presence of a magnetic field, the free electrons in the plasma orbit around the field lines in a right-hand sense at the electron cyclotron

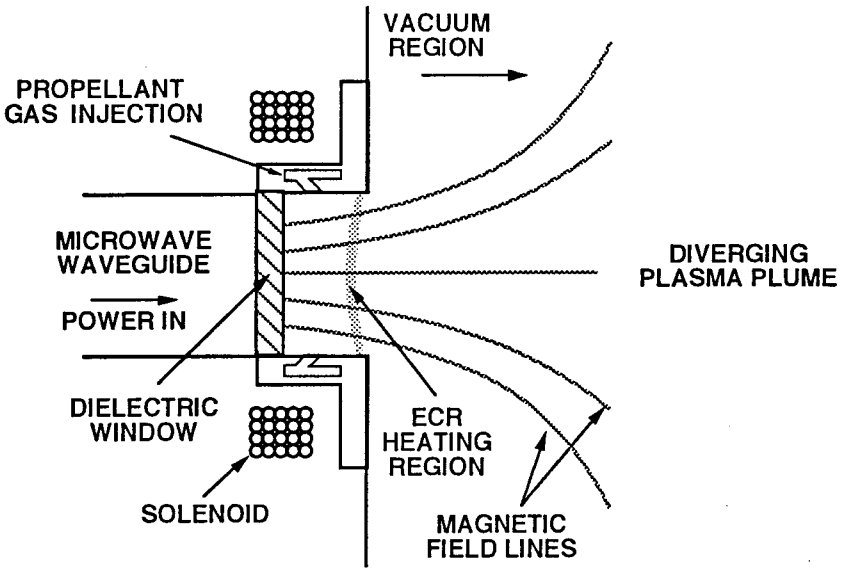

Figure 1-3: Schematic representation of an ECR Plasma Thruster.

frequency given by eB/m. The magnetic field strength is chosen such that the electron cyclotron frequency equals the microwave frequency in a thin energizing zone. The microwave beam is right-hand circularly polarized so that the electric field rotates with the electrons and accelerates them in their orbiting motion. The circular motion of the electrons creates a dipole magnetic field oriented opposite the applied field of the nozzle, and the dipole moment force accelerates the electrons along the magnetic field lines. An ambipolar electric field is then set up which accelerates the unmagnetized ions and in turn produces thrust.

ECR thrusters have no electrodes and therefore none of the problems of erosion, plating, and shorting. Besides eliminating some of the drawbacks of more conventional electric propulsion devices, ECR offers some added capabilities that could make some new missions possible. Because there is minimal surface contact between the plasma and the thruster, even reactive gases such as oxygen and carbon dioxide are potential propellants. This opens up the possibility to use substances available in space as

fuel for a return trip from an asteroid or planet. Extra equipment would be needed to provide microwave power for the thruster, but for applications such as station keeping, the power system could be adapted to use the same microwave generator as the communications in a microwave communications satellite.

Despite the attractive features and possibilities for electrodeless plasma propulsion with ECR [29, 36], several technical challenges must be overcome before ECR thrusters can be considered for propulsion applications. Advances must be made in spacecraft systems such as developing low mass microwave power conditioning and magnet equipment. Thruster advances are also needed to develop an efficient thruster with performance comparable to that of electrostatic ion engines. In particular, the plasma beam divergence must be made small in order to extract the maximum thrust. The magnetic nozzle, which is vital to producing the plasma and restricting its initial radial diffusion, guides the plasma well downstream of the plasma generation zone. As the magnetic field lines curve and eventually return to the nozzle, the plasma tends to follow. For the beam divergence to be small, the plasma must detach from the magnetic nozzle in a well-defined beam. In following chapters we examine the plasma of an ECR thruster experimentally and computationally in an effort to discover more about the ECR thruster and the process of plasma detachment from a magnetic nozzle.

1.2 Related Research

Work on ECR thrusters was initiated in the 1960s by research groups at General Electric Company [29] and NASA Lewis Research Center [25]. This early research identified areas of promise for ECR thrusters, along with some of the problems that have so far prevented ECR devices from developing into usable space thrusters. One problem at the time was that microwave sources were very large. Space application of a high-power microwave thruster was unrealistic because of the weight of the necessary

microwave source. In addition, advances in electrostatic and electrothermal electric propulsion devices made these thrusters more attractive than ECR-based systems. As a result, research on ECR thruster ceased until 1987 when improvements in microwave sources and the prospect of superconducting magnets prompted Sercel [38] at JPL to resume the investigation into ECR propulsion.

Today, much of the interest in ECR plasma sources comes from the materials processing community. For precision etching of silicon wafers in the manufacture of computer chips, a high density plasma with low ion energy is desired [35]. The beam must also be highly collimated for maximum anisotropy in the etch rate. Electrodeless plasma sources have longer operating lifespans than plasma sources such as arcjets in etching applications where the plasma densities and tank pressures are orders of magnitude higher than in propulsion environments [11].

In some of the first ECR work performed at GE, Miller, Bethke, and Crimi [29] tested several thruster designs. The designs varied gas injection methods, antennae and waveguide orientation, and the shape of a plasma chamber surrounding the ECR region in an effort to improve thruster efficiency. The magnetic field strength at resonance was 3800 gauss, corresponding to a microwave frequency of 10.7 GHz. The thrusters were operated using both argon and xenon as propellants with flow rates as high as 0.42 mg/s.

A thrust stand was used to measure the thrust produced by the various thrusters, while a calorimeter recorded the energy absorbed by the plasma. Extremely high efficiencies were measured for the thrusters, with power efficiencies up to 0.79 and thrust efficiencies reaching 0.4 [29]. The maximum thrust recorded was 26 mN, and the specific impulse reached 3200 s. Since the calorimeter measured all the energy in the plasma including the ionization energy, frozen flow losses are not included in the power efficiency figure. Even so, the apparent performance of the thrusters was very promising.

In addition to propulsion parameters, the GE group used intrusive plasma di-

agnostics to measure the plasma parameters at a fixed point in the plasma plume. Diode probes recorded the plasma flux and power density, emissive probes measured the plasma potential, and a gridded energy analyzer was used to measure ion energies. With these diagnostics, they found ion energies which were lower than expected. They suspected that an unexplained mechanism caused a loss of ion thermal energy before the plasma could be accelerated by the magnetic field. They also theorized that entrainment of the background gas resulted in artificially high thrust measurements by increasing the effective propellant flow rate.

Crimi [10] attributed the energy losses to line radiation caused by inelastic collisions and calculated an actual thrust efficiency of only 7-10% for argon. He also contended that additional losses resulted from the production of multiply-charged ions. In later analysis, Sercel [38] concluded that the losses in the GE experiments were due to plasma cross-field diffusion to the walls of the plasma chamber. The design of the thruster used in Sercel's work (also used in the current study) attempts to reduce diffusion losses by eliminating the plasma chamber.

The problem of plasma detachment from the magnetic nozzle was considered for the first time by Kosmahl [25]. Applying a collisionless, cold-plasma model, he computed the trajectories of plasma particles accelerating due to the diamagnetic force on the electrons. He found that even in the collisionless approximation, plasma will cross magnetic field lines and may emerge as a well-defined beam under certain conditions. He found that trajectories are independent of ion mass, but are greatly affected by varying the initial plasma energy. Sercel [37] followed Kosmahl's work and suggested that manipulating the magnetic nozzle configuration would aid in detachment of the plasma.

Resuming the experimental work on ECR after a two-decade hiatus, Sercel [36] constructed a laboratory thruster with a lower magnetic field strength and microwave frequency than that in the GE work. The resonance field strength and RF frequency were 750 gauss and 2.115 GHz respectively. Lower energy ions would be expected in

Sercel's thruster than those in the earlier studies, but the intent of the chamberless design was to reduce radial diffusion. Sercel carried out some preliminary studies on the altered thruster using intrusive plasma diagnostics and examined the applicability of the ECR device to spacecraft from a systems perspective.

Sercel's theoretical work focused on a steady-state, quasi-one-dimensional plasma model which predicted plasma potential, ion velocity, and propulsion parameters such as thrust and I_{sp} for an ECR thruster similar to the laboratory device. The code models microwave absorption, ionization, and several loss mechanisms as well as effects of background neutral gas. Using the model, Sercel qualitatively predicts the reduction in plasma potential and ion kinetic energy with increasing tank pressure seen in his experiments although the pressure used in the model to approximate the background neutral gas is much lower than that actually observed in the experimental apparatus. The model predicts the power efficiency for the laboratory device to be approximately 0.3. Comparing the calculated plasma characteristics to those found in the experiments, the model overestimates plasma potential and energy. Sercel attributes the discrepancy to unknown loss mechanisms such as plasma instabilities or inefficient microwave absorption in the experimental thruster.

Following Kosmahl's and Sercel's collisionless trajectory calculations, Hooper [18] modeled a cold flowing plasma by ignoring the acceleration mechanism and initiating the plasma with an initial velocity along the field lines. In this work he found a non-dimensional variable, he denoted G, that governs plasma detachment. He showed that for a plasma initiated in the plane of a single coil magnet, separation occurs only for plasma initiated within a hybrid electron-ion Larmor radius of the axis. Hooper suggests that an annular plasma between coaxial magnets may be advantageous for detachment. Hooper has recently begun experimental research on a thruster that uses ECR heating to create a plasma in a magnet nozzle [19]. In this device, microwave radiation is coupled to the plasma with an elliptical antenna designed to enhance absorption. The RF beam travels through a magnetic nozzle in the whistler mode

to the ECR region at a point where the magnetic field is 20% of the maximum field. The large mirror ratio is intended to reduce backstreaming of the plasma to the body of the thruster. Only preliminary results of these experiments are available.

Finally, Gerwin et al. [31] at Los Alamos National Laboratory address plasma detachment from a magnetic nozzle in their work using an ideal MHD code. They speculate that for resistive separation to occur, a strong downstream temperature drop in the plasma would be necessary to cause a sufficient increase in electrical resistivity. However, they found that longitudinal electron thermal conduction prevents such a temperature reduction. In addition they found negligible crossing of the magnetic field even considering plasma resistivity because axial drag forces negated resistive separation. Their other suggestions for improving separation include changing conditions to enhance recombination and the Rayleigh-Taylor instability and using a dense plasma with a sharp boundary, so the external field cannot penetrate the plasma.

1.3 The Present Study

The body of work related to ECR plasma propulsion is not extensive, leaving many questions unanswered. The purpose of the work described below is to further examine an ECR plasma thruster and increase the experimental information about the plasma plume. A secondary goal is to evaluate the ECR concept as a potential thruster for space applications. In addition, we investigate the detachment of plasma from a magnetic nozzle as it relates to the ECR plasma thruster and other applied-field electric thrusters.

The limited amount of data on the plasma characteristics of ECR plasma thrusters suggests a need to map the spatial variation of plasma parameters as a function of the thruster operating variables of flow rate, microwave power, and vacuum tank pressure. The results of these experiments are used as a base for modeling and experimental investigations into plasma detachment in addition to their use as a tool for evaluating

the performance of an ECR thruster. An MHD simulation code is used to estimate the effects of electrical resistivity and background gas in the vacuum tank on the results produced in the ECR experiments

To directly examine plasma behavior in a magnetic nozzle, a reasonable first step would be to perform a simplified analysis of how the plasma travels in the presence of a magnetic field. The information gained in this modeling work which assumes a collisionless plasma is used in the design of experiments on plasma detachment. Insight is also gained into the separation mechanism of a collisionless plasma from a magnetic field.

The collisionless analysis sets the baseline for experimental investigations into plasma detachment. The experiments examine the effects of resistive detachment as well as detachment due to collisionless mechanisms. Comparison of the model to experiment should provide some knowledge of the role of resistivity in plasma detachment.

The end result of this study is the identification of key issues relevant to the development of plasma thrusters utilizing applied magnetic fields. The study also provides an evaluation of the ECR concept as a thruster.

1.4 Outline of this Report and Summary of Results

In Chapter 2 the experimental apparatus for the ECR plasma thruster experiments are described along with the experimental methods. The plasma diagnostics and data reduction procedures are also presented. The noteworthy features of the setup include the movable diagnostics which allow measurements of the spatial variation of the plasma parameters. Also, the automated data acquisition system stores the collected information on a computer, making data reduction possible even for the gridded energy analyzer and Langmuir probe which require large amounts data for

each measurement.

The results of the experiments on the laboratory ECR plasma thruster are presented in Chapter 3. In Sections 3.1 and 3.2 ion flux and energy measurements are shown for a range of thruster operating conditions. Three-dimensional plots of the ion flux in the plasma plume reveal that at low pressures, the plasma is annular. It is believed that secondary electrons from the thruster lip cause the plasma to be denser near at the edges of the plume. At low pressures, radial electron motion is restricted by the strong magnetic field, so the annular plasma propagates along the field lines. As the pressure increases, collisions increase radial diffusion of electrons causing the maximum flux density to occur at the thruster axis where the microwave intensity is greatest. The ion energy is nearly invariant as microwave power is increases, and only a slight increase is realized as the pressure decreases. It is suspected that collisions retard the ion energy and that the energy would increase at pressures lower than could be attained in the present facility.

Propulsion parameters calculated from the flux and energy data are presented in Section 3.3, and the thruster performance is compared to that of a small ion engine. The laboratory ECR thruster proved to have poor performance in comparison to the ion engine. The thrust, and efficiency increased as the flow rate and microwave power were increased. The increase in performance was entirely due to additional ion flux because the ion energy was nearly constant over the range of operating conditions studied. The performance was artificially enhanced by entrainment of the background gas in the vacuum tank especially at high flow rates. The measured ion flux exceeded twice the inlet gas flux at the highest flow rate of 10 sccm.

Emissive probe measurements of the plasma potential are shown in Section 3.4. A Langmuir probe was used to measure the electron temperature in the plume for various plasma conditions, and the results are presented in Section 3.5. The plasma potential decreases in the axial direction away from the thruster but varies little in the radial direction. The vacuum pressure was found to greatly affect the magnitude of

the plasma potential. As the tank pressure decreases, the plasma potential increases at all locations in the plume. The higher plasma potential is beneficial for thrust production because the ions fall through the potential field to ground far from the thruster.

Studies of the microwave reflection and transmission in the plasma are described in Section 3.6. A microwave antenna was placed in the plume to measure the microwave power transmitted through the ECR region, and a directional coupler recorded microwave power reflected back through the waveguide. Microwave absorber was positioned in the vacuum tank during the transmission studies to reduce reflection from the tank surfaces. The transmission measurements indicate that as the propellant flow rate increases, a smaller percentage of the input microwave power reaches the vacuum tank. At very high flow rates only a small fraction of the microwave beam is transmitted through the ECR region.

The reflection studies reveal similar results. At low pressures and flow rates, less than 5% of the input power is reflected back through the waveguide, but as the propellant flow rate increases, a sharp increase in reflection is noted at approximately 1×10^{-4} torr. At higher pressures and flow rates the reflected power reaches 23% of the input power. Considering the results of both microwave studies, it is likely that a large portion of the microwave power is not absorbed by the plasma in the ECR region.

Chapter 4 describes the results of a collisionless cold plasma trajectory model similar to those of Kosmahl, Sercel, and Hooper. The model is applicable to several applied-field electric thrusters in addition to ECR thrusters. The affect of plasma acceleration is examined, and non-dimensional parameters are calculated to determine the conditions necessary for plasma detachment. The influence of changes in the field geometry on plasma separation is also examined. The collisionless model showed that the plasma detaches from the magnetic field even without resistive detachment. The mechanism for collisionless detachment is electron inertia, and is discussed in

Appendix A. However, the magnetic field deflects the plasma significantly and leads to large divergence losses. Manipulating the magnetic field can reduce these losses. Moving the plasma generation region axially away from the magnet reduces deflection. The diameter of the usable plasma generation region (The region in which the plasma is deflected by less than 90°.) reaches the coil diameter when the plasma initiation region is 4 to 5 coil radii from the plane of the magnet. However, when the ECR region is moved away from the magnet, the field strength must increase to maintain the ECR condition. Losses resulting from plasma deflection in the magnetic nozzle present a serious barrier for applied-field thrusters that must be better understood before such devices can be considered for space application.

Using the results of Chapter 4 and considering the difficulty in accurately modeling resistive plasma detachment, the experiments described in Chapter 5 attempted to experimentally examine plasma detachment. An ion engine was placed in the field of a magnetic nozzle, and the grids were masked to emit an annular plasma beam. The effect of the magnetic nozzle on the plasma was evaluated using the plasma diagnostics from the ECR experiments. Since the plasma from an ion engine is created independent of the applied field, unlike an ECR plasma, the magnetic field can be any strength. We could then compare the trajectories as we altered the field.

The experiment did not work as planned because the magnetic nozzle restricted the radial motion of the neutralizer electrons and prevented full neutralization of the ion beam outside the thruster. As a result, a radial electric field, seen in the plasma potential measurements, developed in the plume. The trajectories of the unmagnetized ions were then determined by the potential gradients instead of the magnetic field lines. When the magnet was turned off, the beam was efficiently neutralized, and no radial potential gradient was observed.

The effect of the radial electric field can be seen in the ion flux profiles. Instead of deflecting the plasma annulus, the magnetic field causes the beam to spread out and actually constrict in radius. Because the magnetic field prevents electrons from

moving to the ions, the ions move to the regions of lower potential. The low energy ions in the plume are deflected through the greatest angle, resulting in the region of low energy ions along the thruster axis. When the propellant flow rate increases, collisions increase radial electron diffusion across the magnetic field, and the effects of inhibited neutralization are decreased.

The mechanism for collisionless plasma detachment from a magnetic nozzle is discussed in Appendix A. An explanation of the behavior of a uniform ring of plasma in a magnetic field is derived using a Lagrangian analysis. In Appendix B efforts to model the collisional detachment of the plasma with a two-dimensional MHD code are described. The goal of this modeling work was to examine the effects of the vacuum tank on the trajectory of a plasma beam in a magnetic nozzle. Due to difficulties in adapting the code to a steady-state problem, the results did not meet the objectives of the work.

Chapter 2

Experimental Apparatus and Diagnostics

2.1 Laboratory Vacuum System

A general schematic of the experimental apparatus is shown in Figure 2-1. The vacuum facility was designed for research into electric propulsion devices at pressures as low as 4×10^{-5} torr.

The main body of the vacuum chamber is a horizontal stainless steel cylinder which is 2 m long and 1.5 m in diameter. A stainless steel end cap opposite the thruster moves on a wheel assembly to allow access to the interior of the tank. Vacuum pressure seals the back end cap to the tank during tank operation. The front end cap holding the thruster contains a smaller cylindrical section (1 m diameter, 70 cm length) which is parallel to the main body of the tank, but the axes of the two sections are horizontally offset by 10 cm. A cross section of the tank showing the front end cap is shown in Figure 2-2. The total distance from the inside of the back end cap to the inside of the front end cap is 2.7 m.

Vacuum in the system is provided by a roughing pump - diffusion pump system as Figure 2-1 shows. The tank is pumped to a rough vacuum of 200 millitorr by a mechanical roughing pump with a rated pumping speed of 300 cubic feet per minute. High vacuum is achieved with a 22 in. diameter silicon oil diffusion pump with a rated pumping speed of 18,000 liters per second. The baffle system of the diffusion

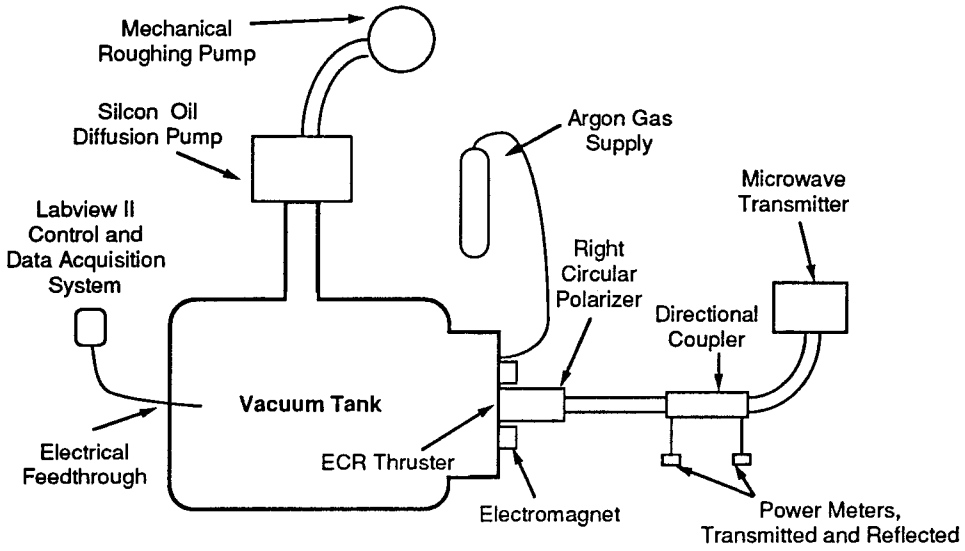

Figure 2-1: General schematic of experimental apparatus.

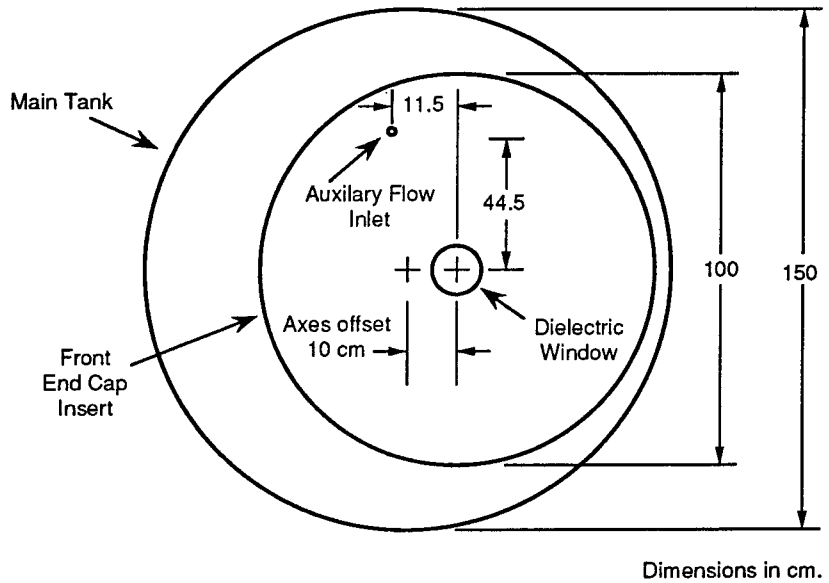

Figure 2-2: Diagram of front endcap.

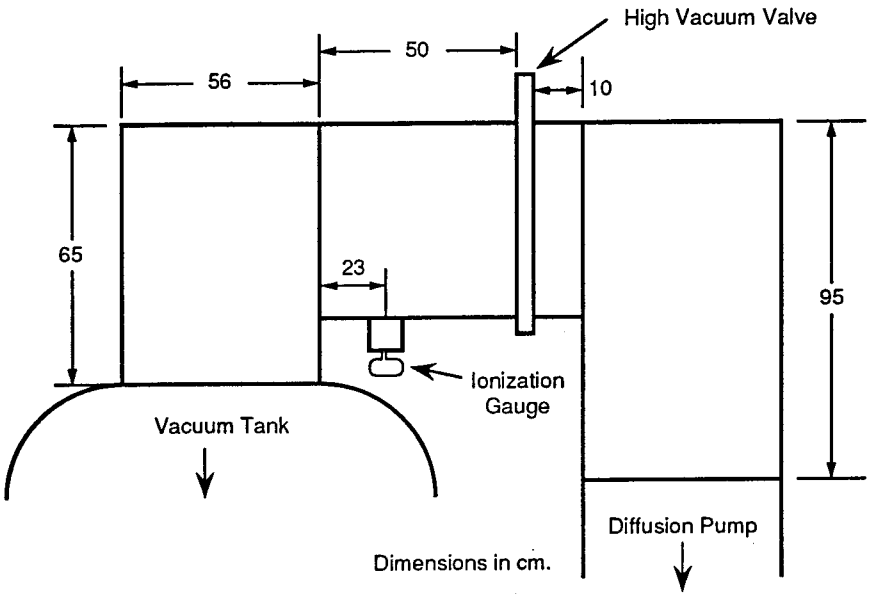

Figure 2-3: Schematic of diffusion pump duct system.

pump is cooled by refrigerated liquid alcohol to minimize pump oil backstreaming. Gas enters the diffusion pump through a port in the top of the main body of the tank centered 1.7 meters from the face of the front end cap. As Figure 2-3 shows, gas exiting the tank passes through a 22 in. diameter "U" shaped conduit before entering the diffusion pump. Pressures are measured with an ionization gauge near the entrance to the diffusion pump as shown in the figure. While the pumping efficiency is lowered slightly by the elongated path the gas must take, space considerations in the laboratory necessitate this geometry. The mechanical roughing pump provides auxiliary pumping for the diffusion pump exhaust. With no gas addition to the system, pressures as low as 9×10^{-5} torr have been achieved in the facility.

Vacuum feedthroughs for electrical connections include two 16-pin feedthroughs for data collection and control of the stepper motors and a coaxial feedthrough for microwave radiation measurements. Other feedthroughs include the ionization gauge, and two argon gas feedthroughs in the front end cap for the main thruster and auxil-

iary flows. Visual access to the tank is provided through five glass viewports. Stainless steel screens are welded over the viewports to prevent escape of microwave radiation.

Argon gas is provided from a compressed gas cylinder. The main flow is supplied directly to the thruster for injection upstream from the ECR region. The auxiliary flow enters the tank through a remote port shown in Figure 2-2. The purpose of the auxiliary flow is to increase the pressure in the tank without supplying additional propellant to the thruster, so pressure can be controlled independently of propellant flow rate. The flows originate at the same argon cylinder, but they are controlled by separate mass flow controllers. The flow rates are set manually on the controller unit and are read remotely by the data acquisition system described below. The flow controllers have a rated accuracy of 0.5% of the full scale of 100 standard cubic centimeters per minute (sccm). Typical flow rates used in the experiments range from 3 to 20 sccm.

The applied magnetic nozzle is provided by a solenoid coil of 0.5 inch diameter copper tubing electrically insulated with fiberglass sleeving. Two coils are connected in parallel to reduce electrical resistance in the circuit. The coil has a mean diameter of 23 cm and consists of approximately 150 turns. A constant current DC welding power supply rated for 400 A at 36 V supplies current for the electromagnet. Up to 180 A pass through each branch of the magnet circuit during operation. The coil is cooled by water circulating through the tubing. The solenoid is mounted to the front end cap coaxially with the smaller section of the tank and the waveguide [38].

A microwave transmitter using a klystron amplifier tube supplies microwave power to the thruster. The microwave beam emitted from the transmitter is linearly polarized and has a frequency of 2.115 GHz to match the electron cyclotron frequency for a magnetic field of 750 gauss. Power output can be varied up to 20 kW. As Figure 2-1 shows, a rectangular waveguide carries the beam through a directional coupler where microwave power meters measure transmitted and reflected power in the waveguide. The linearly polarized beam then passes through a polarizer which converts the beam

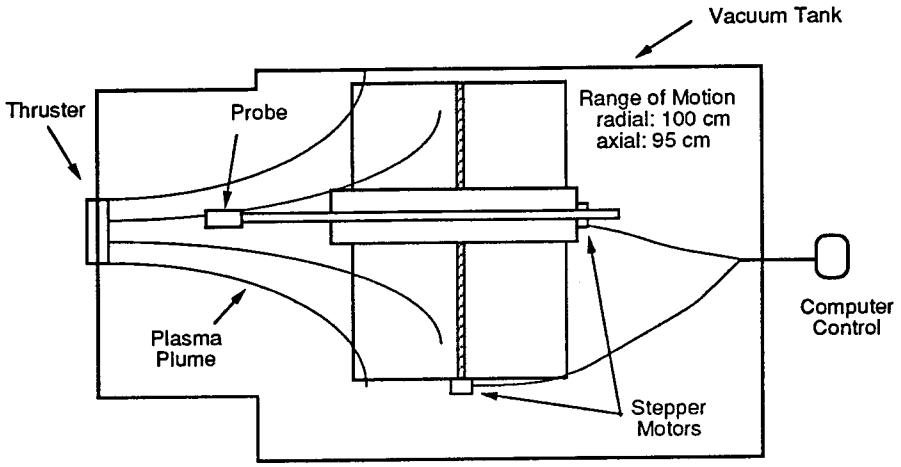

Figure 2-4: Schematic of probe actuator.

to right circular polarization which is desired for the thruster.

To measure spatial profiles of plasma characteristics, diagnostic probes move in the axial and radial directions on a diagnostic arm shown schematically in Figure 2-4. Computer-controlled stepper motors inside the tank rotate 1.8° per step driving axial and radial lead screws which move the arm. The pitch of each lead screw is 5 threads per inch, so the minimum linear positioning increment is 0.001 inch. The computer records the probe position relative to a known position by incrementing the linear position of the arm every time the motors turn. The arm can move a total of 100 cm in the radial direction and 95 cm in the axial direction to map the plasma parameters throughout the plume. Foil coverings protect the stepper motor wires from damage due to the plasma and microwave radiation.

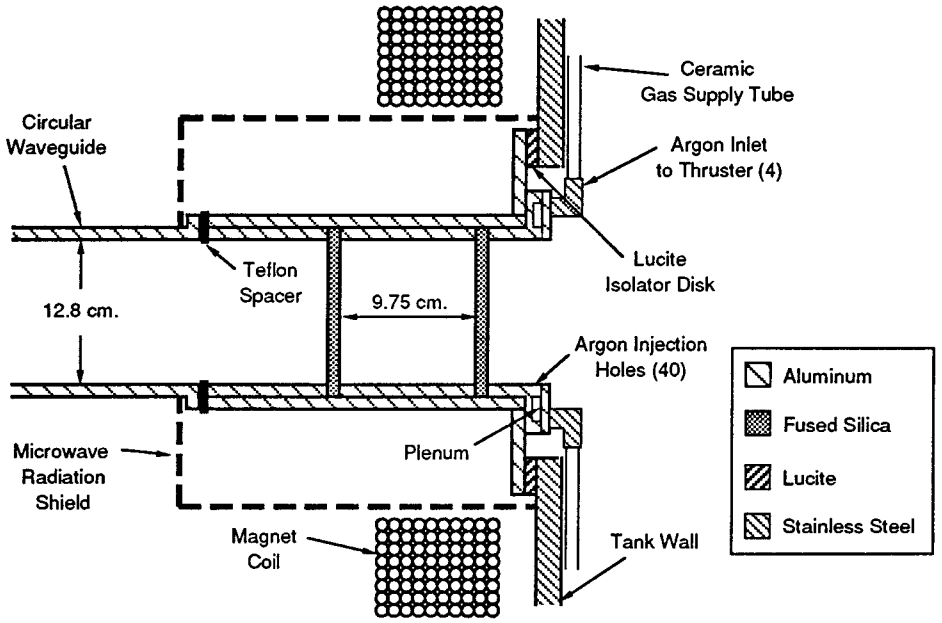

Figure 2-5: Schematic of experimental ECR plasma source.

2.2 Experimental ECR Thruster

The ECR plasma thruster used in the experiments detailed in the following chapters is shown schematically in Figure 2-5. The right circularly polarized microwave beam enters the thruster through two fused silica windows. A numerical model was used to determine the ideal separation distance between the dielectric windows to minimize microwave reflection. Less than 1% of the incident power is reflected with no plasma present.

Argon is supplied to the thruster through a manifold system seen in Figure 2-6. The gas enters the thruster in four azimuthal locations and passes to a plenum to equalize pressure in the azimuthal direction. The argon is then injected radially upstream from the ECR region through 40 equally spaced 0.04 in. injector holes. The injected gas is ionized in a thin region where the electron cyclotron frequency

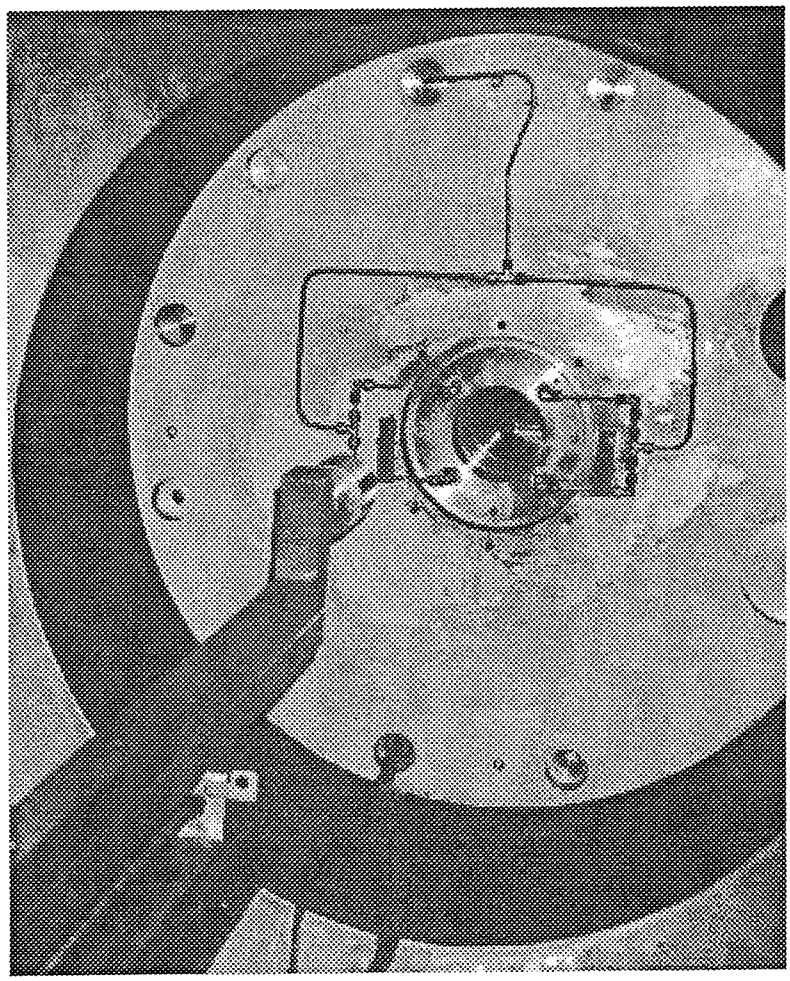

Figure 2-6: Photograph of ECR thruster showing dielectric window, argon supply system, and probe arm.

and the microwave frequency are equal. The solenoid magnet coil described above is mounted coaxial to the waveguide, so the plasma is created in an axisymmetric magnetic nozzle. The face of the second dielectric window is 4.2 cm downstream from the center plane of the magnet, so the magnetic field decreases monotonically as the plasma travels away from the ECR region. The mirror ratio between the dielectric window and the ECR region is approximately 0.7.

During thruster operation, the plasma appears to be attached to the lip of the thruster downstream from the gas injection holes. In the laboratory the plasma attachment region can be seen as a polished region around the edges of the central waveguide hole. Since the plasma is attached, the thruster must be electrically isolated to ensure that the plasma potential is not grounded. Ceramic gas feed tubes between the manifold and the inlet to the thruster isolate the argon supply from thruster. As Figure 2-5 shows, insulating gaskets secured by nylon bolts isolate the thruster from the tank walls and from the upstream waveguide. Because microwave radiation can escape through the insulators, a safety shield is placed over the end of the waveguide.

The plasma source has been operated for power levels up to 3 kW and tank pressures up to 2×10^{-4} torr. A typical plasma plume is shown in Figure 2-7. The plasma has a bright white-blue color which increases in intensity with increasing flow rate and microwave power. For high flow rates, a distinct, curved margin can be seen at the edge of the plume presumably following the magnetic field lines (not visible in the photograph).

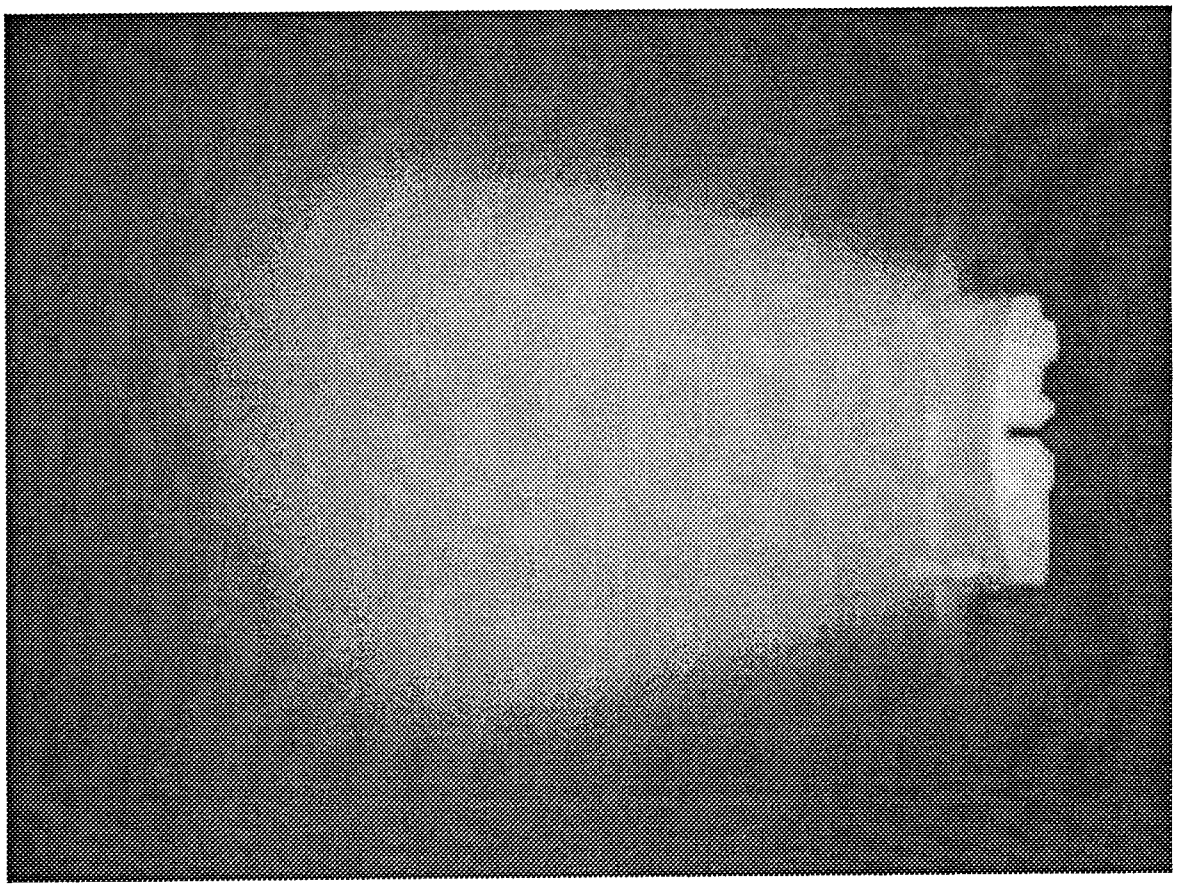

Figure 2-7: Photograph of the plasma plume emitted from the laboratory ECR thruster.

2.3 Plasma Diagnostics

2.3.1 Faraday Cup

A diagram of the Faraday cup used in the experiments is shown in Figure 2-8. The cup is secured to the movable arm and the probe is oriented parallel to the thruster axis. The outer case is grounded at laboratory ground, and a negative potential of 200 V is applied to the inner cup to repel the electrons, allowing only ions to reach the surface of the cup. To choose the voltage applied to the inner cup during the experiments, the current was measured as a function of the cup bias. As the negative potential increases, more electrons are repelled, so the cup current increases as fewer electrons are collected while the ion current remains constant. When the cup potential is large enough, only ions can reach the cup, so additional increases in cup potential result in no additional current. The cup bias is set to the voltage at which the cup current becomes nearly constant [30]. The majority of secondary electrons are recollected by the probe because of the tubular geometry, so the current collected at the inner cup is approximately the ion saturation current. The aperture area is 1.0 cm^2, so the cup current measured by the ammeter is actually the ion current density per cm^2 [39].

2.3.2 Gridded Energy Analyzer

The gridded energy analyzer (GEA) is shown schematically in Figure 2-9. A series of screens charged to different potentials alters the plasma beam, so only ions with energy larger than the ion decel voltage are collected at the collector plate. The case and attenuator grid are grounded. The attenuator allows a plasma beam of diameter 0.7 cm to enter the body of the GEA which has a 5 cm diameter. Attenuation of the beam is necessary to insure that the Debye length inside the GEA is longer than the grid spacing. This prevents the plasma from shielding the electric field between the screens.

A potential of -200 V (the same potential that was used for the Faraday cup) is

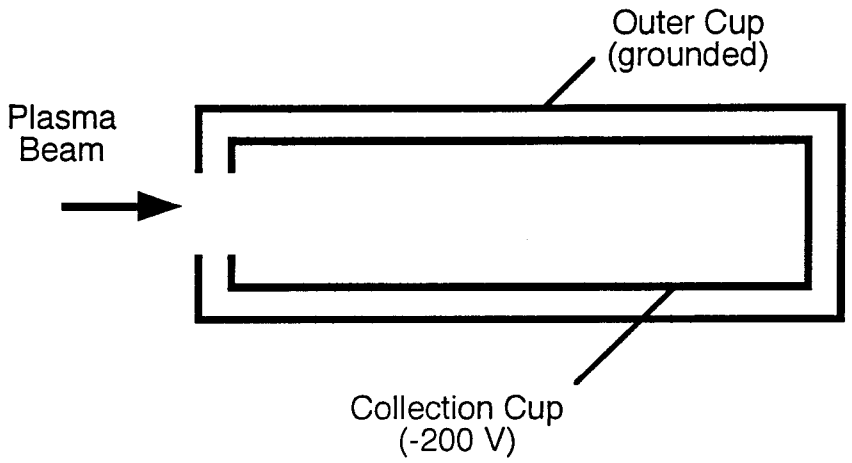

Figure 2-8: Diagram of Faraday cup.

applied to the electron repel screen to prevent the electrons from continuing into the GEA with the ions. A variable positive potential from 0 to 100 V is applied to the ion decel grid. Only ions with energy sufficient to overcome the ion decel potential are able to pass through the second screen. The final screen is the suppressor, which is biased negatively to deflect secondary electrons back to the collector plate. The collector plate is biased slightly negative to attract the ions that pass through the ion repel screen. The current is measured at the collector plate.

To obtain the ion energy distribution, the potential on the ion decel screen is increased from zero volts in several volt increments. At each step, the current through the collector plate is measured. The result is a monotonically decreasing function of current versus voltage as shown in Figure 2-10. Below 15 V the curve is relatively flat, since the potential on the ion repel screen is less than the plasma potential. All the ions fall from the plasma potential to ground at the GEA case, so all ions are able to reach the collector plate when the bias voltage is less than the plasma potential. At about 15 V the bias voltage equals the plasma potential, and the current begins to

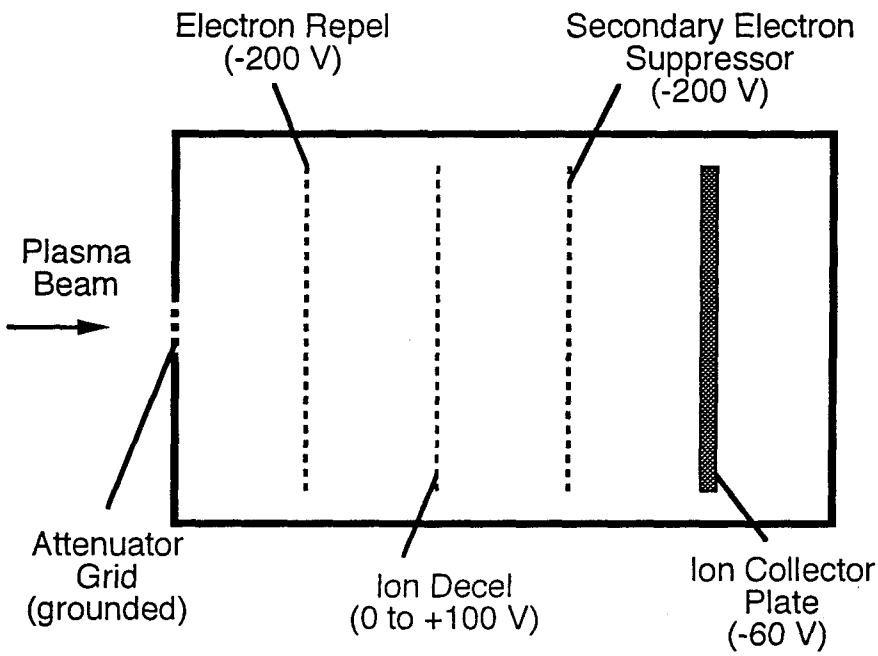

Figure 2-9: Diagram of gridded energy analyzer.

drop as more ions are repelled by the increasing ion decel grid potential. The curve flattens out at about 60 V when only the highest energy ions can pass through the decel screen. To smooth small variations in the data, we fit a fifth order polynomial to the curve. The derivative of the polynomial yields the unnormalized, one-dimensional energy distribution for the ions' axial motion. A typical distribution function is shown in Figure 2-11. The energy of peak number density calculated from the polynomial (27.3 eV in the figure) is taken as the kinetic energy of the ions [34, 26, 4].

2.3.3 Emissive Probe

A diagram of the emissive probe used to measure the plasma potential in these studies is shown in Figure 2-12. The tungsten filament and power supply are electrically isolated from the laboratory and are allowed to float. A DC current is applied to the filament, so that electrons are emitted from the glowing probe tip. If the probe is negative with respect to the plasma potential, electrons emitted from the filament will escape. However, if the probe is positive, the emitted electrons will be attracted back

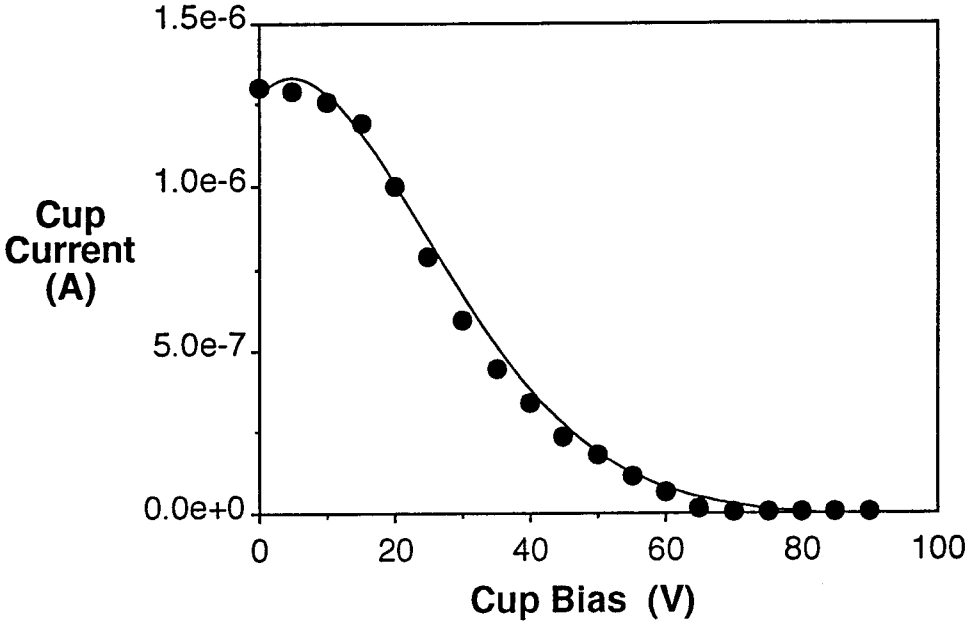

Figure 2-10: GEA current vs. ion repel voltage with fifth order polynomial curve fit.

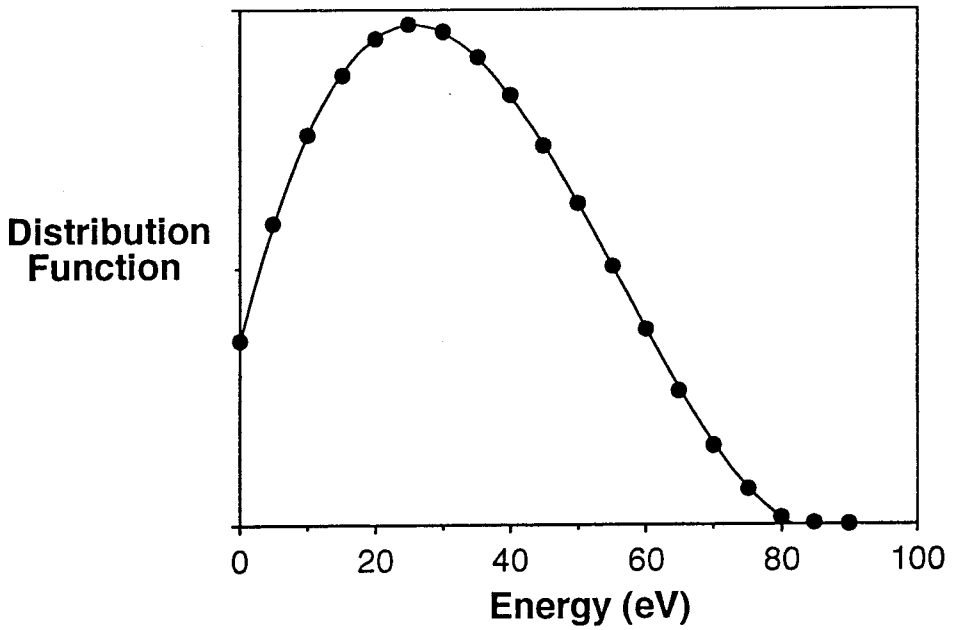

Figure 2-11: One-dimensional ion distribution function.

to the filament. If the probe is allowed to float, the probe potential of a sufficiently emitting probe will therefore be near the plasma potential. Unfortunately, because the temperature of the plasma electrons is much greater than that of the electrons emitted from the filament, the emitted current will not be able to compensate for the electron current collected from the plasma and the floating probe potential will therefore not be equal to the plasma potential. As a result a small sheath forms at the filament resulting in a probe potential which is slightly negative with respect to the plasma potential. While the probe potential is not strictly the same as the plasma potential, in this report we will refer to the measured potential at the probe as the plasma potential because the depth of this sheath is small compared to the plasma potential [8].

The probe potential relative to laboratory ground is measured on the copper connection wire approximately 4 in. from the filament on the positive side of the power supply. To determine the power supply voltage needed for the probe to emit sufficiently, the probe potential was measured as a function of the power supply voltage. As the power supply voltage increases, more electrons are emitted from the filament and the depth of the sheath around the probe begins to decrease. When the probe potential is near the plasma potential, the curve of probe potential vs. power supply voltage flattens out, resulting in a "knee" in the data. The power supply voltage is chosen as the voltage at which the "knee" occurs, and therefore the filament floats at approximately the plasma potential. This procedure was repeated each time the filament was replaced. The filament is oriented so that it points toward the oncoming plasma.

2.3.4 Langmuir Probe

A diagram of the Langmuir probe is shown in Figure 2-13. Two probes on the same mounting are used to independently obtain the electron temperatures perpendicular and parallel to the magnetic field. The collecting surface of each probe is a 0.025 in.

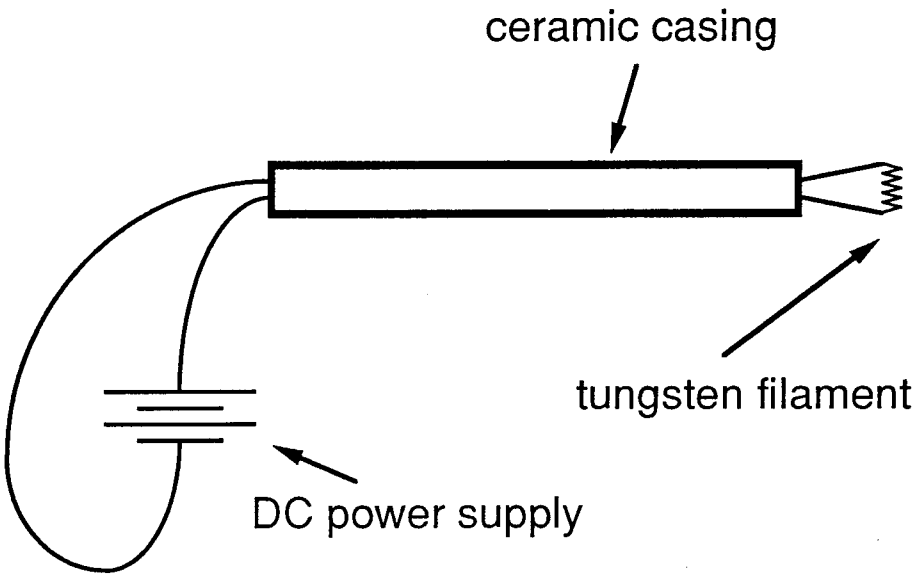

Figure 2-12: Diagram of Emissive Probe.

diameter, 0.54 in. long tungsten probe. A variable-voltage power supply is used to apply a known positive potential to the probe relative to ground. The potential is incremented from zero to +120 V, and the probe current is measured as a function of the voltage applied. A typical curve of current vs. voltage is shown in Figure 2-14. At large positive voltage, the probe is saturated and collects only electron current. The "knee" in the curve (at approximately 40 V in the figure) where saturation occurs is at the plasma potential. The probe oriented across the magnetic field lines measures the component of T_e parallel to the magnetic field ($T_{e_\parallel}$) because most of the electrons that reach the probe must travel along the field. Conversely, the probe oriented along the magnetic field lines measures the perpendicular component of T_e because electrons travel perpendicular to the field lines to reach the probe.

The conditions of the experiment (low pressure and high magnetic field) lead to inaccurate calculations of plasma density using Langmuir probe data. The area of the probe is needed to calculate the density, but since the electron Larmor radius is not much greater than the probe dimensions, the effective area of the probe is

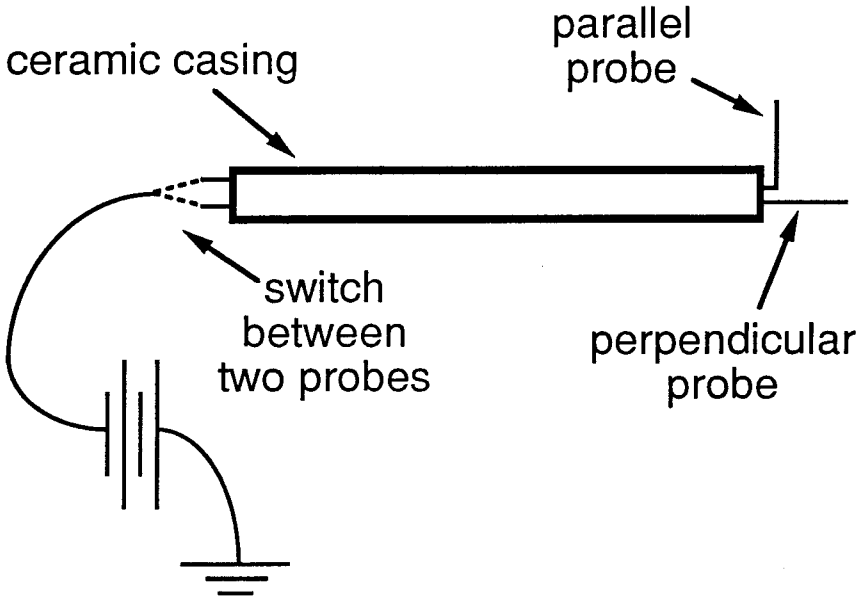

Figure 2-13: Diagram of Langmuir Probe.

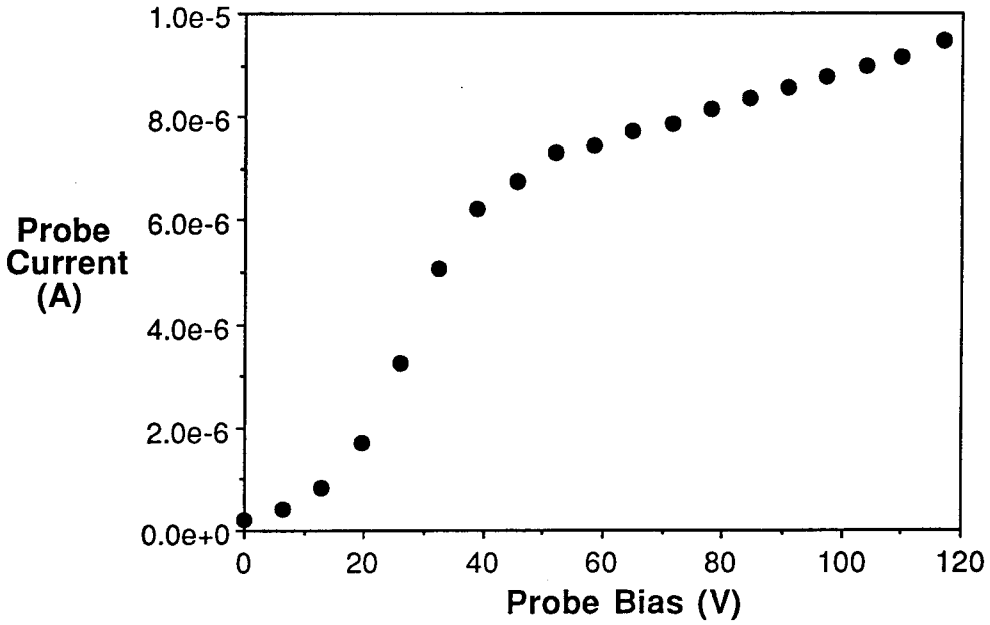

Figure 2-14: Langmuir current vs. probe voltage.

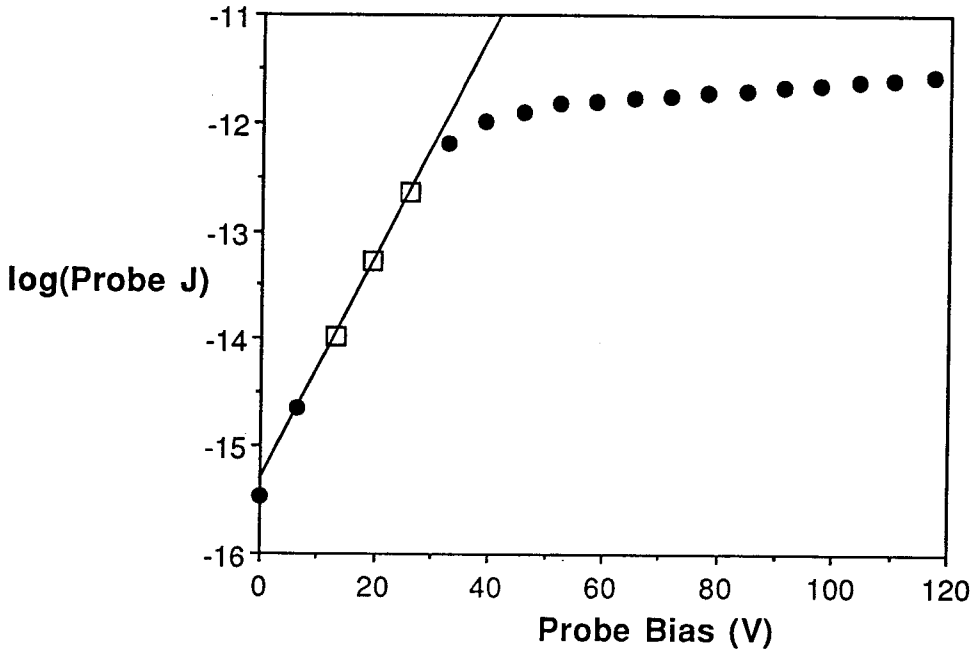

Figure 2-15: Log of Langmuir probe current vs. probe voltage with linear fit to selected points.

less than the actual area by an unknown amount. However, it is still possible to calculate electron temperature using standard Langmuir probe theory [10]. We use the logarithmic determination of the electron temperature here. When the probe potential is between ion saturation and electron saturation, the current collected by the probe as a function of the probe potential is given by the equation

$$J = J_0 \exp\left(\frac{e\Theta_{pr}}{kT_e}\right), \tag{2.1}$$

where J is the electron current collected by the probe, J_0 is the electron saturation current, Θ_{pr} is the probe potential, and T_e is the electron temperature [26, 10]. In using Equation 2.1 we assume that the plasma is quasineutral, the electrons and ions are Maxwellian, $T_e >> T_i$, and the electron and ion mean free paths are much longer than the dimensions of the probe and the Debye length. It is seen from Equation 2.1 that in the probe potential range applicable for the equation, a plot of $\log(J)$ vs. Θ_{pr} is a line whose slope is inversely proportional to T_e. As shown in Figure 2-15, when

the probe potential is less than the plasma potential, the $\log(J)$ vs. Θ_{pr} curve is also linear for the data. To obtain the electron temperature from the data we fit a line to the three data points just before the probe reaches electron saturation. Since the data is a time average, inaccuracies arise due to fluctuations of the plasma potential at the RF frequency. The plasma potential fluctuations result in overestimation of T_e, but using data points near electron saturation produces the best estimate of T_e when using time averaged data [43, 9, 20, 26, 15].

2.4 Labview Data Acquisition System

Information about the vacuum system and thruster operating conditions and all data from the diagnostics are collected by a Macintosh computer running Labview II software. In addition, Labview controls the position of the probes and the voltage supplied to the probes by two remote-controlled power supplies.

Through the serial port in the computer, Labview II communicates with an American Precision Industries SAC-560 smart axis controller which in turn controls a P41 stepper motor driver that actuates the motors. The computer causes each motor to turn a given number of 1.8° steps in either direction. A text file holds the current axial and radial position of the probe, and the position is incremented by the number of steps each time a motor is instructed to move. Before moving the motors, the computer checks whether the intended position is outside the range of the lead screw. To move to a given position in the tank, the computer calculates the number of steps necessary and moves the motors accordingly.

Several external devices are controlled through the GPIB card in the computer. The computer sets the voltage and current supplied to the probes by two HP 6030 series power supplies with a range of 0-500 V. The voltage can be increased from 0 V to full scale in 300 ms. The resolution of the current read from the power supply is 1 mA. Since the currents measured from the diagnostics are often less than 50 μA, probe

currents are measured independently by a picoammeter described below. The GPIB card also reads the transmitted and reflected microwave power through a HP 438 2-channel power meter.

Other voltages and currents in the experiments were measured with a 16-channel A/D converter (backplane) connected to a digital I/O card in the computer. Since the power supplied to the probes can only be incremented once every 300 ms, the fastest possible measurement of the probe current is approximately 3 Hz. Therefore, a sweep of the voltage and current is always slower than the microwave frequency, so all currents shown below are averages over many microwave periods. With such a slow sampling rate already, no information is lost by averaging the data further, so each value that the computer records is the average of several measurements. In addition to measuring probe voltages and currents, the backplane measures the output from a picoammeter, the flow meters, the electromagnet ammeter, and the pressure transducer D/A converter. All the data is saved in text files on the Macintosh, and the probe data is processed with various mathematical programs to reveal the desired information about the plasma.

Chapter 3

ECR Experimental Results

This chapter describes experiments conducted on the plasma plume of the ECR thruster experimental device discussed in Chapter 2. Measurements of the ion current density, ion energy, plasma potential, and electron temperature are presented in the following sections. The theory behind the diagnostics and the experimental method are described in Section 2.3. From the ion flux and energy measurements, thrust, specific impulse, and propulsive efficiency were calculated for the laboratory thruster, and the results are shown in Section 3.3. Microwave transmission and reflection measurements are presented in Section 3.6.

3.1 Ion Current Measurements

Profiles of the plasma ion current for different operating conditions are shown in Figures 3-1 and 3-2. These measurements were made by traversing the probe in a grid pattern in the plasma. The plasma is generated in the upper left region in the plots, with the plume extending toward the lower right. The center plane of the magnet is located at axial position 0 in all the figures in this report, and the dielectric window is 4.2 cm downstream from magnet at axial position -4.2 cm. The negative numbers in the three-dimensional plots are needed to obtain the desired orientation in the graphing program.

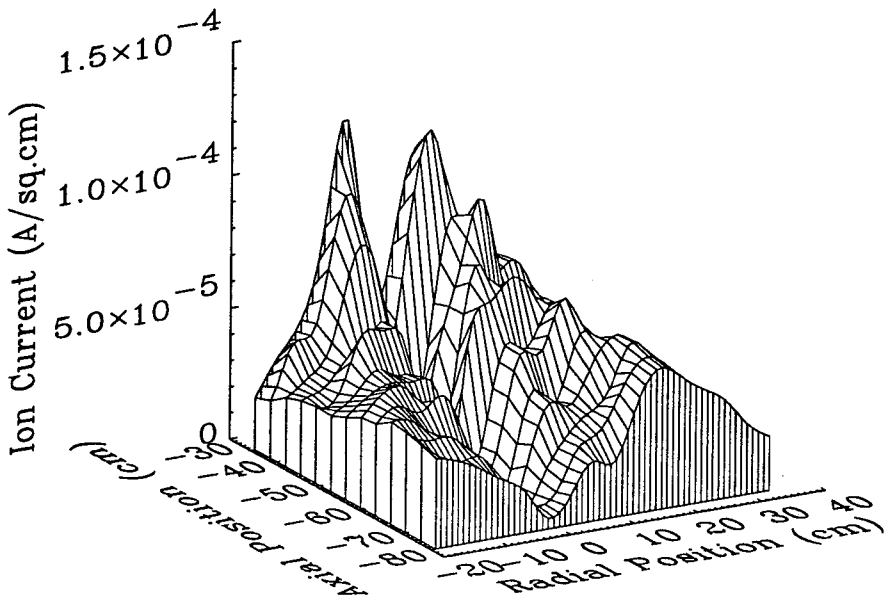

Figure 3-1: Ion current density profile for 3 sccm, 300 W.

An unusual profile featuring a region of low ion current on the thruster axis is seen in Figure 3-1. A depression in the ion flux density profile was observed using a similar experimental device in the 1960s by Miller, Bethke, and Crimi [29]. The region of depressed ion current is absent in the results shown in Figure 3-2, which were obtained at higher flow rate, pressure, and microwave power.

The cause of the lower ion flux on the thruster axis at low pressures is unclear, but several possibilities exist. One possibility is that secondary electrons from the waveguide are needed to help sustain the argon plasma at low pressures. Collisions provide the only mechanism for radial diffusion, and at low pressures (4.8×10^{-5}torr in Figure 3-1) diffusion may be retarded enough that the secondary electrons are not able to reach the center of the waveguide. The resulting plasma would then be annular with the densest plasma on the edges of the waveguide. Without sufficient diffusion the plasma will be held within a Larmor radius of the magnetic flux surface

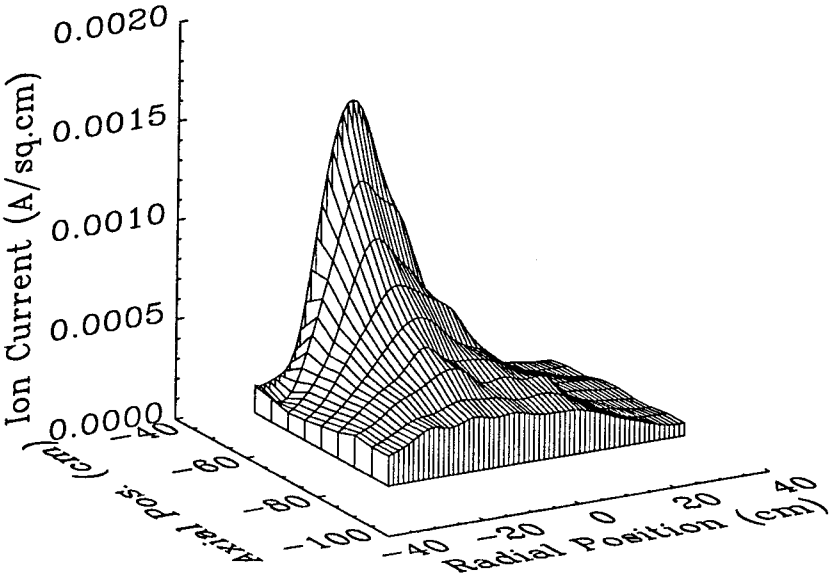

Figure 3-2: Ion current density profile for 8 sccm, 600 W.

at which it was created as it accelerates downstream, resulting in an annular plasma propagating downstream.

When the flow rate (and therefore pressure) is higher, as is the case in Figure 3-2, the increased collision frequency enhances radial diffusion. Electrons may then be able to diffuse across the ECR region to create a more uniform plasma. With sufficient cross-field diffusion the plasma density should also be maximum on axis since the microwave power density is maximum on axis. Figure 3-2 with a sharp peak on axis suggests that the plasma in the ECR region does indeed have maximum density on the thruster axis.

From observations of the laboratory thruster, the argument that secondary electrons support the plasma seems likely. At low pressures such as the conditions in Figure 3-1, the plasma is difficult to initiate. An emissive element inside the tank is occasionally needed to maintain the plasma. When the plasma is on, it is clearly

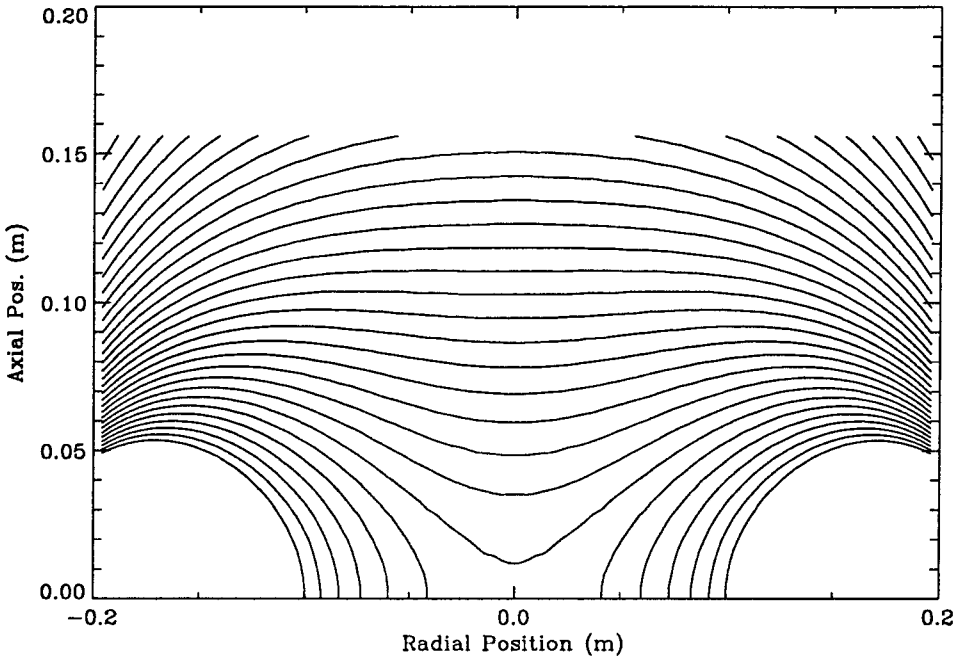

Figure 3-3: Calculated contours of constant magnetic field strength.

attached to the tank at the end of the waveguide. This part of the tank has been polished by the plasma even on the face of the tank slightly outside the waveguide where the plasma would be shielded from the microwave beam. Visual observations of the plasma did not reveal any obvious annular structure to the generation region at high or low pressures, but the plasma was more uniform in brightness across the face of the window at higher pressures.

Another possible explanation for the annular ion flux is that insufficient magnetic field strength would cause the ECR region to intersect the dielectric window resulting in no plasma production in the center of the waveguide. In Figure 3-3 calculated lines of constant magnetic field strength are shown for a cross section through the axis of a current loop with a radius of 0.23 m, the mean radius of the magnet coil in the laboratory. As the figure shows, the surfaces of constant magnetic field strength near the dielectric window are convex toward the window. Therefore, some of these

surfaces will intersect the window on a circle at the thruster axis. If the magnetic field is slightly weaker than necessary, the electron cyclotron frequency will match the microwave frequency on an intersecting surface, and an annular plasma will be formed. Again, reduced cross-field diffusion at low pressures would be necessary for the annular ion flux to persist as the plasma moves into the tank. At higher pressures, the increased radial diffusion may eliminate the annular flux profile. However, if this is the case, at high pressures we would expect a relatively uniform profile rather than one that is maximum on centerline like Figure 3-2.

To test this explanation further, we extrapolated the peaks of the ion flux in Figure 3-1 back to the dielectric window along the magnetic field lines calculated for the same current loop used in Figure 3-3. The peaks were found to intercept the window at a radius of approximately 2.5 cm from the axis. Let us assume that the ECR region ($B = 0.075$ T) intersects the window along a circle of radius 2.5 cm during normal operation. Let us further assume that the plasma is extinguished when the ECR region intersects the window at the radius of the waveguide, 6.4 cm. Using the calculated magnetic field we found that a 4% drop in current through the coil would move the intersection of the window with the ECR region from $r = 2.5$ cm to $r = 6.4$ cm. The plasma in the laboratory thruster does not extinguish until the magnet current is under 80% of the normal operating current. While the field for the magnet in the thruster may be slightly different from that of a single coil with the same mean radius, it seems unlikely that the plasma intersects the dielectric window during normal operation of the laboratory device.

The annular flux profile is exaggerated when the input power is increased. As Figure 3-4 shows, the valley in the flux on the thruster axis becomes more pronounced as the microwave beam power increases at a fixed flow rate. The additional power creates a denser plasma at all radial positions, but the radial diffusion is still low enough that the plasma remains mostly near the wall. Annular flux distributions have been observed for flow rates and pressures as high as 8 sccm and 8.0×10^{-5}torr

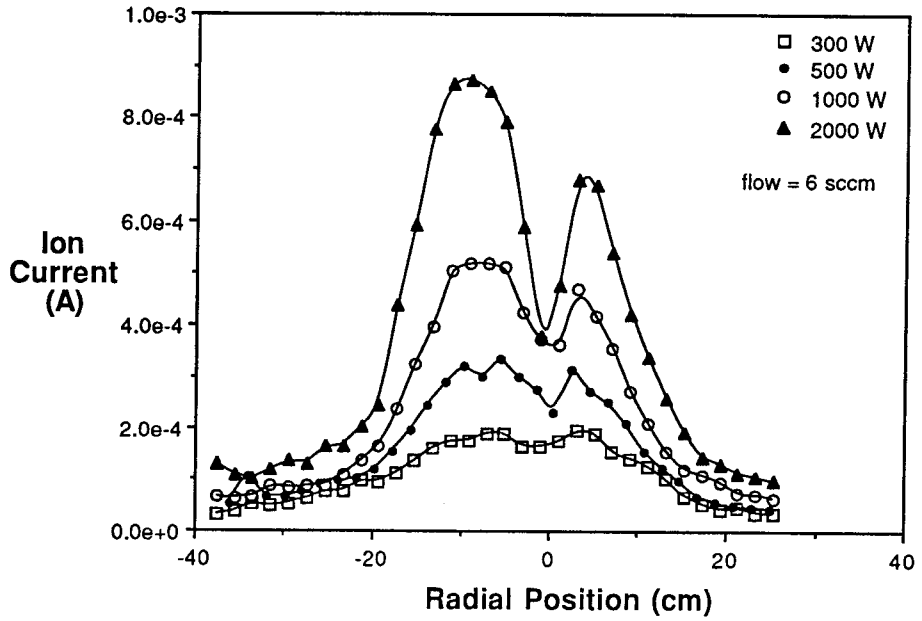

Figure 3-4: Total ion flux at 44 cm from the magnet centerplane as power increases at fixed flow.

in our experimental apparatus. It seems likely that annular plasmas would occur for even higher flows rates, but in our experiment the background pressure increases with flow rate causing the diffusion rate to increase as well.

The background pressure adds an additional false "flow rate" to the ECR region, and increases the collision rate to the point that annular flow no longer occurs. As Figure 3-5 confirms, the background pressure in the tank is the governing parameter affecting the ion current density. In the first curve the pressure is controlled by increasing the inlet flow to the thruster. For the other curve the initial pressure of 5.5×10^{-5}torr is set by the inlet flow to the thruster, but the pressure is increased by introducing an auxiliary flow of argon to the tank away from the thruster. As Figure 3-5 shows, the extra background neutrals seem to be incorporated into the plasma flux just as if they were injected directly into the thruster.

If, as we conjecture, inadequate electron radial diffusion is the cause of the annular ion flux at low pressures, it seems likely that this phenomenon would occur for even

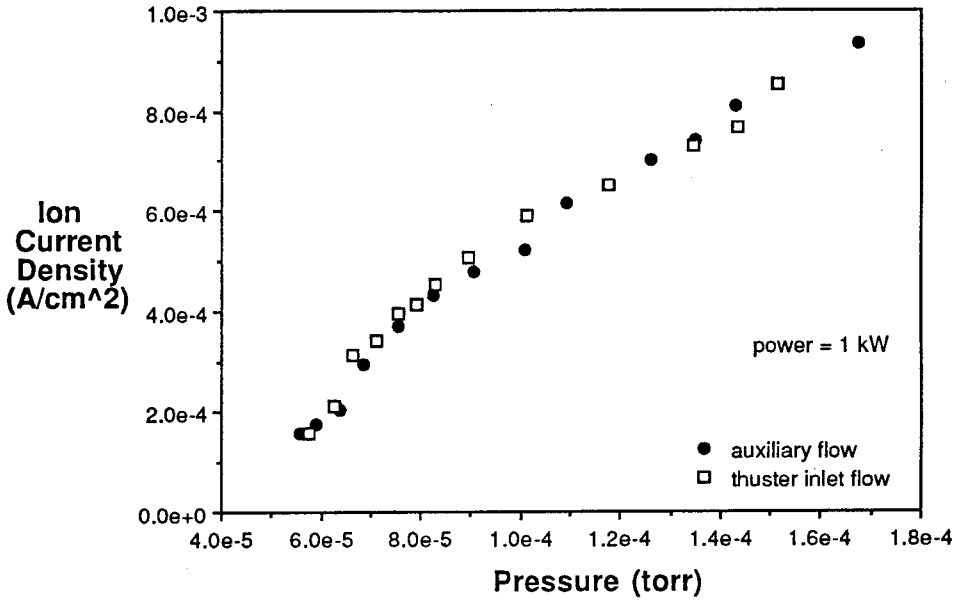

Figure 3-5: Ion current density at the thruster axis 45 cm from the magnet centerplane as tank pressure increases. A comparison of the effect of background pressure due to thruster inlet flow and auxiliary flow remote from the thruster.

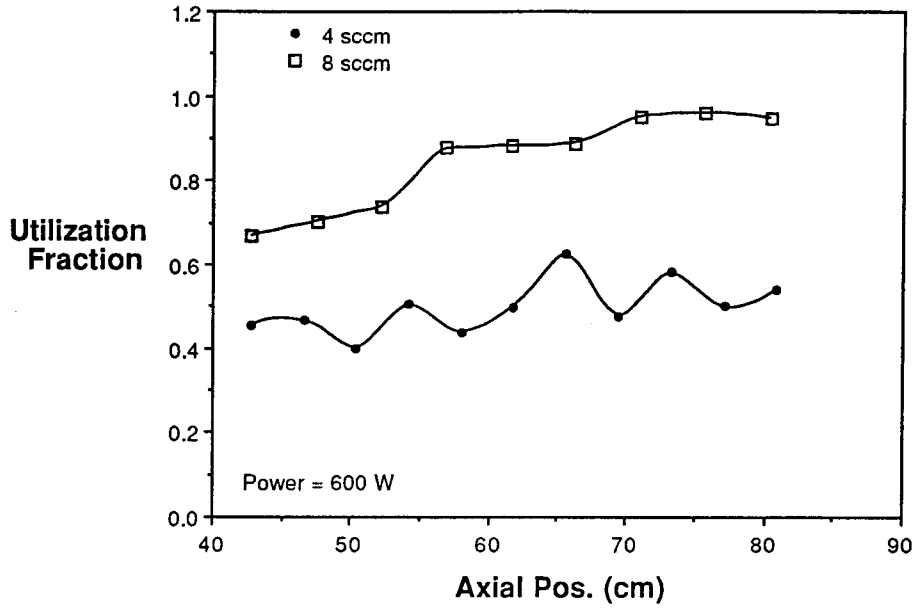

Figure 3-6: Evidence of background gas entrainment at high flow rates.

very high flow rates if the tank pressure could be kept below 5.0×10^{-5}torr. The plasma is deflected least by the magnetic nozzle, and divergence losses are minimized if the plasma density is maximal on the axis as in Figure 3-2. The microwave power will also be best utilized if the plasma has maximum density on axis. For these reasons annular flow must be avoided for a working ECR thruster. More study of this effect is needed in a vacuum facility capable of lower pressures than the facility used in these tests before this thruster concept can be fully evaluated.

Background gas is entrained by the plasma downstream in the plasma plume in addition to being ionized in the ECR zone. Evidence of this entrainment is shown in Figure 3-6. The ion flux density was integrated in the radial direction to obtain the total ion flux at several axial positions in the plasma plume. For the 4 sccm case the data are inconclusive, but for the 8 sccm case, the total flux increases as the plasma travels axially, indicating a source of plasma downstream from the ECR region.

We also calculated the total ion flux at a fixed axial position to evaluate the effect

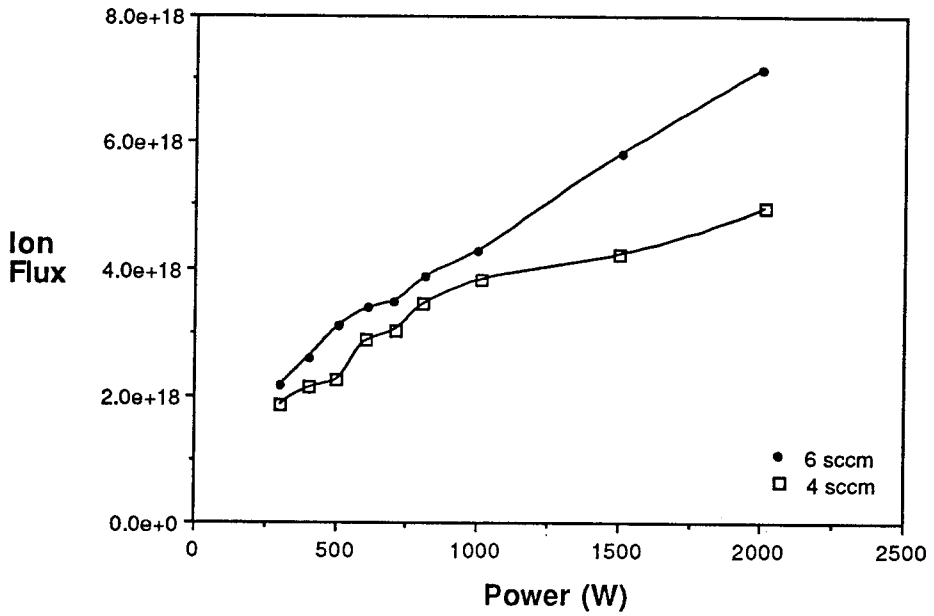

Figure 3-7: Effect of input power on integrated ion current at the thruster axis, 44 cm from the magnetic centerplane.

of changes in flow rate and power. As shown in Figure 3-7, ion flux increases as power increases. The flux increase levels off above 1000 W for the 4.0 sccm case. This implies that there is a limit to the amount of energy that is transferred to the plasma. Below 1000 W increases in power result in a greater degree of ionization and a steep flux vs. power curve. Above 1000 W additional power is dissipated in other ways, resulting in a flatter curve of flux vs. power. This leveling-off is not present in the 6.0 sccm case. The added pressure from the higher flow rate means that more background gas is available to be incorporated into the plasma. Additional power ionizes the extra background gas, resulting in a continued steep increase in ion flux with power. A leveling-off may occur at a power level higher than shown in Figure 3-7.

The effect of flow rate on total ion flux is shown in Figure 3-8. There is a steep rise in flux at low flow rates when the gas flow increases at constant power. The sharp increase levels off when a saturation flow rate is reached. It appears that below the saturation flow rate the plasma remains at a fixed ionization fraction, and increases

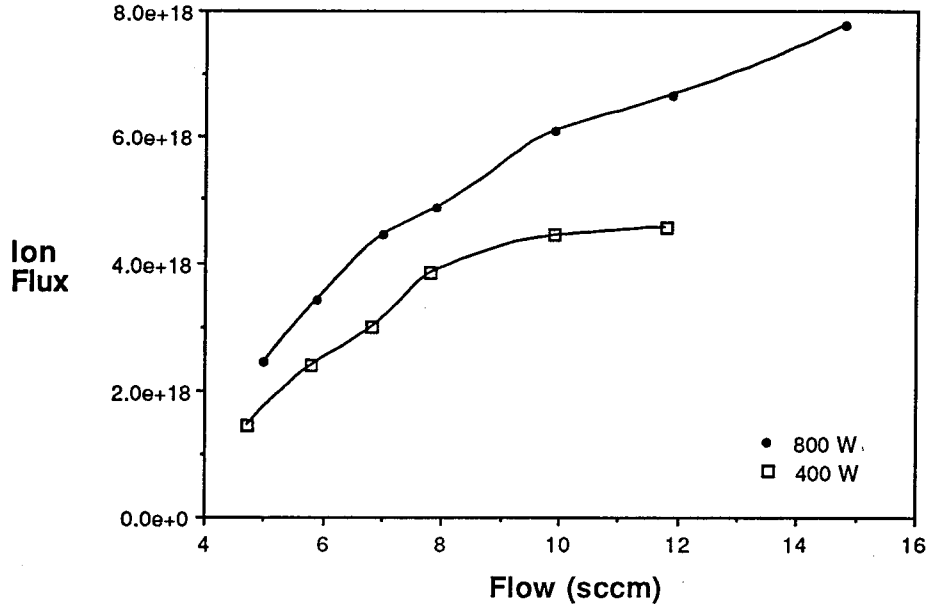

Figure 3-8: Effect of flow rate on integrated ion current at the thruster axis, 44 cm from the magnetic centerplane.

in flow result in a greater ion flux. At the saturation flow rate the input power does not ionize the same fraction of the additional gas, and increases in flow result in more neutrals in the plasma. The total ion flux continues to increase as the flow increases above saturation but at a reduced rate. Later data suggest that microwave reflection may contribute to this reduced rate of increase (See Section 3.6).

The effects of increasing power and flow rate are combined in Figure 3-9, which shows the fraction of the argon atoms injected into the thruster which appears in the total ion flux. As we can see, at higher flow rates and power levels, a large portion of the total ion flux is from ionization of the background neutrals. The mirror ratio between the dielectric window and the ECR region is approximately 0.7, so 23% of the electrons have velocities in the loss cone. Without the ionization of extra neutrals, the maximum propellant utilization fraction would be 0.77. As Figure 3-9 shows, enough background gas is ionized to make up for the mirror losses and increase the propellant utilization above unity at high power and pressure. This increase in plasma

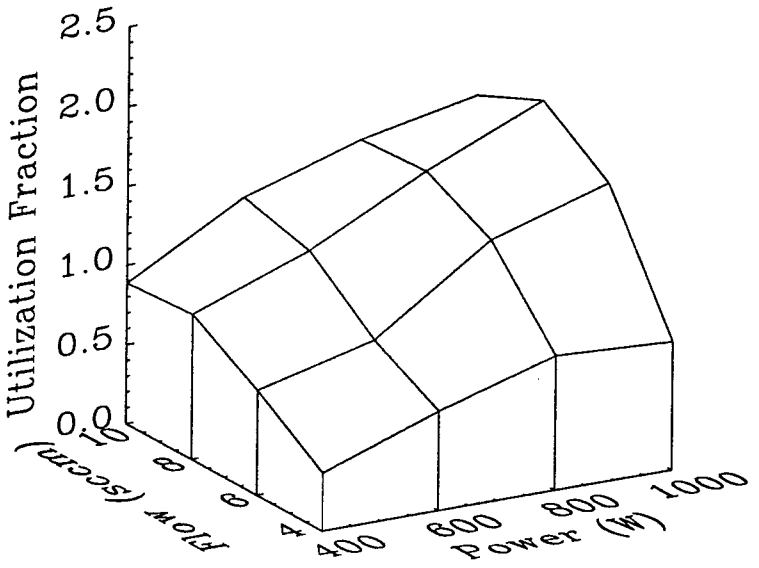

Figure 3-9: Propellant utilization.

flow due to the imperfect vacuum in the tank will greatly affect our calculations of the propulsion parameters in Section 3.3.

3.2 Ion Kinetic Energy Measurements

A gridded energy analyzer (GEA) was used to measure the kinetic energy of the ions directed axially. The GEA device and data analysis methods are discussed in Section 2.3. The GEA was used similarly to the Faraday cup. Spatial profiles of ion energy were made for a range of operating conditions by traversing the probe axially and radially inside the tank on the movable diagnostic arm. As we see in the following figures, the GEA data contains more scatter and uncertainty than the Faraday cup data due to the nature of the probe. The slope of the current collected vs. the voltage on the ion decel screen is needed to compute the ion energy in contrast to the ion

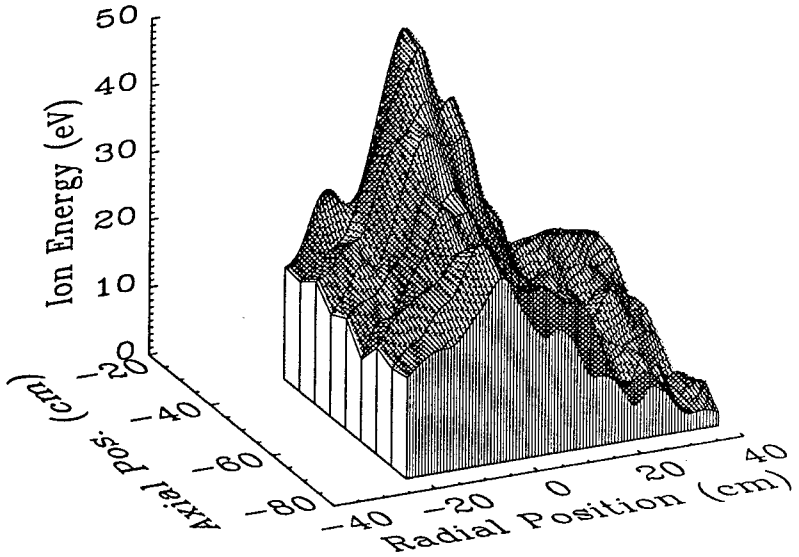

Figure 3-10: Ion energy profile for 6 sccm, 560 W.

current which requires only the magnitude of the current which can be averaged over many samples.

A plot of the ion kinetic energy profile in the plasma is shown in Figure 3-10. As the plasma moves axially away from the ECR region (off the axial scale of the graph at approximately -10 cm), the ions lose energy in collisions, resulting in a decrease in kinetic energy. In the radial direction, the energy drops off sharply at the edge of the plasma. The lower energy at the edge the plume may be due to friction with the background gas at the edges of the plasma beam or to deflection of the plasma by the magnetic nozzle which decreases the axial component of velocity in favor of radial velocity or to a combination of these effects. The ion energy falls to nearly zero in far right region of the figure where the plasma density drops outside the plasma plume.

In Figure 3-11 the effect of input microwave power on the kinetic energy of the plasma is shown. The data were taken at a fixed position and at a fixed flow rate of

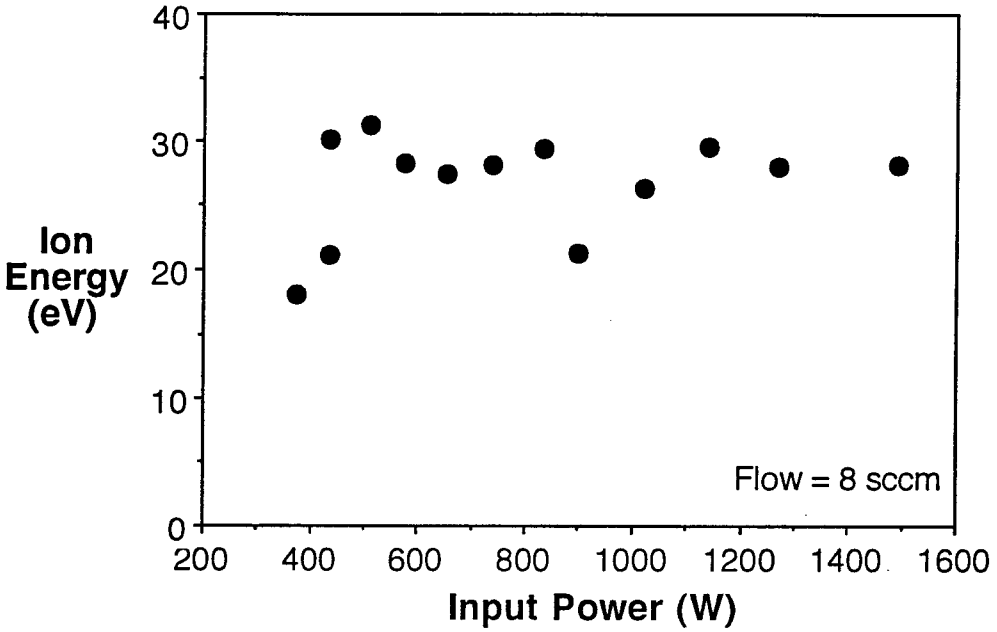

Figure 3-11: Effect of varying input power on ion energy at the thruster axis, 58 cm from the magnetic centerplane.

8 sccm. It appears that increasing the applied power has a negligible effect on the energy of the ions. This implies that there is a limit on the amount of energy that is transferred to the axial motion of the ions. As we saw with the ion flux, the extra power goes into added ionization of neutrals up to a saturation level, beyond which additional power results in a reduced ionization fraction and a slower increase in ion flux. Since the added power is not transferred into ion kinetic energy or completely into increased ion flux, it must be dissipated. Possible reasons for the limit on ion energy are the failure of the electrons to absorb all the input microwave energy, collisions with the background gas, or the inability of the electrons to transfer all their cyclotron energy to axial motion of the ions.

The effect of increasing flow on ion energy is shown in Figure 3-12. The energies were measured in a fixed position with constant microwave power input. As we might expect, increasing the flow rate and pressure results in lower ion kinetic energy. As the density of neutrals and ions increases with greater flow, collisions cause ions to

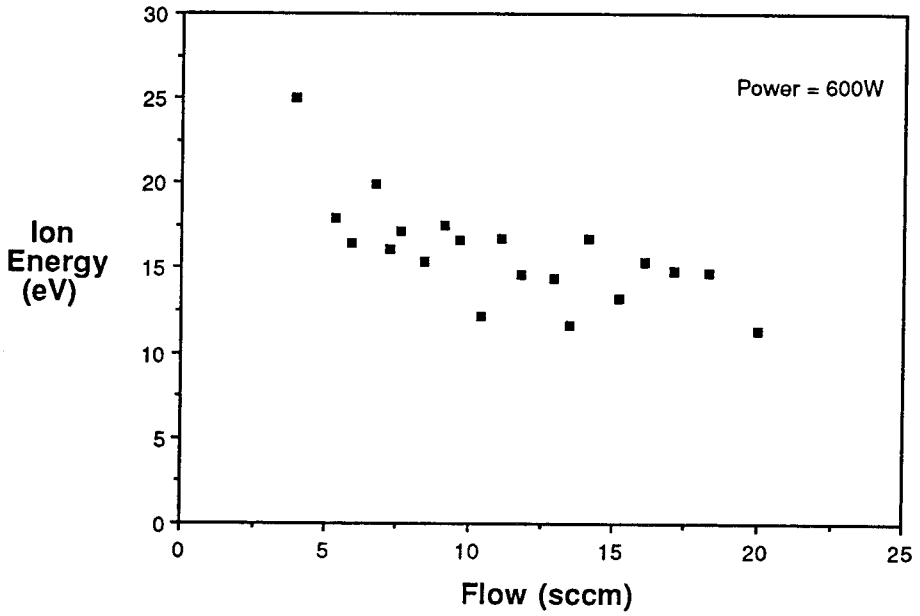

Figure 3-12: Effect of varying propellant flow rate on ion energy at the thruster axis, 58 cm from the magnetic centerplane.

lose kinetic energy. As we saw in Figure 3-8, increasing the flow rate increases the number of ions, but the energy of those ions is decreased.

In earlier research on an ECR thruster, Miller, Bethke, and Crimi observed similar trends in ion energies. Increasing the propellant flow rate in their device lowered the ion energy, but increasing the microwave power level had little effect on ion energy. Ion energies in their experiments averaged approximately 60 eV [29], which is about three times greater than ion energies found in the current work. The larger ion energies observed in the earlier research may be due to the larger magnetic field strength in the ECR region, since the plasma potential is approximately proportional to the magnetic field strength in an ECR device [29]. Since the ion energies recorded for our device and by Miller, Bethke, and Crimi were both measured at a fixed position downstream where the magnetic field was very small, the ions had fallen through most of the total potential drop, so we can fairly compare the results. The maximum field strength in the earlier experiment was 3000 G, approximately four times the maximum field

strength in the present research, 750 G. So the ions accelerated through a potential that was also approximately four times greater and subsequently achieved higher average energy than in the work presented here.

3.3 Calculated Propulsion Parameters

Using the GEA and Faraday cup data, the thrust, propulsive efficiency, and specific impulse can be calculated. The thrust is given by

$$\text{thrust} = 2\pi \int_0^{r_{max}} \frac{\dot{m}}{A}(r)\, v(r) \cos\left(\Theta(r)\right) r dr. \tag{3.1}$$

where $\dot{m}/A(r)$ is the mass flux density of the ions measured by the Faraday cup, $v(r)$ is the axial component of the ion velocity calculated from the measured ion energy, and $\Theta(r)$ is the final divergence angle that the ions achieve after being deflected by the magnetic field. All quantities in Equation 3.1 can be determined from the measured ion current and energy, except for $\Theta(r)$. For an initial estimate of thruster thermodynamic performance desired here, we ignore the nozzle divergence losses. These losses will be substantial, as discussed in Chapter 4, but are not clearly understood for a fully collisional plasma [24, 37, 13, 18]. For simplicity, and to smooth out uncertainties in the ion energy measurements, we will approximate the axial velocity, $v(r)$, by an average ion velocity, v, computed from the average of the energies measured across the plume by the GEA. Making the stated assumptions and integrating Equation 3.1, we can calculate the propulsion parameters discussed below.

The thrust is shown as a function of flow rate and power in Figure 3-13. As expected, thrust increases with both power and flow rate. The increase in ion flux with increasing flow rate offsets the decrease in ion energy at higher flow rates. Comparing the thrust of the ECR device to that of a 15 cm ion engine in use at the Jet Propulsion Laboratory, the ECR device falls short of the 20 – 30 mN produced by the ion thruster at 500 – 900 W of input power [7]. The thrust must be increased if this concept is to

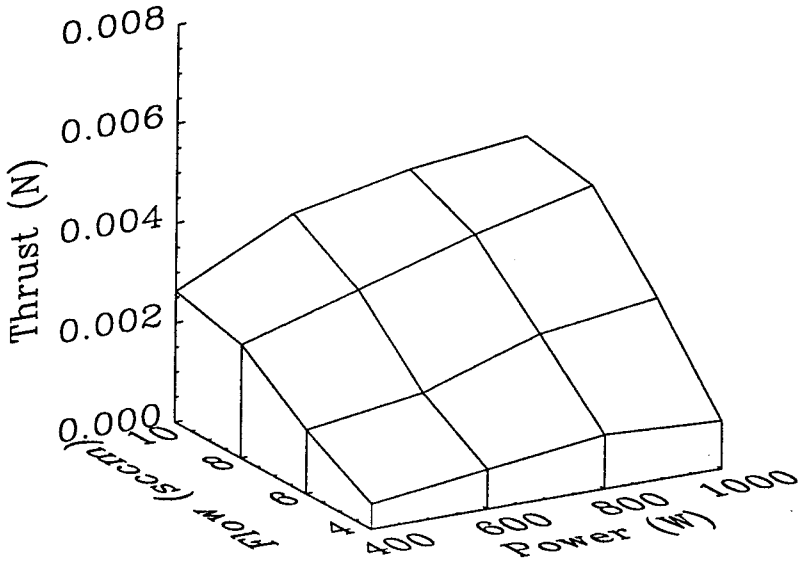

Figure 3-13: Thrust

compete with ion engines for interplanetary missions. Increasing flow and microwave power input may increase the thrust to desired levels.

The specific impulse of the laboratory thruster is shown in Figure 3-14. Note the similarity between Figures 3-14 and 3-9. Ionization of background gas is not considered in the I_{sp} calculations, so the I_{sp} increases as the propellant utilization increases. Since the propellant utilization fraction is nearly two at high flow and power levels due to entrainment of the background gas, the specific impulse shown is up to twice the actual value. If we use the mass flow of the measured ion flux from the data in Figure 3-9 to calculate I_{sp}, the dependence on the utilization fraction is eliminated, and we get the results shown in Figure 3-15. The flat profile shown in Figure 3-15 reflects the near invariance of the ion energy with both power and flow rate. Again comparing the ECR thruster to the JPL 15 cm ion engine, the specific impulse of the ion engine is 2.5×10^4 m/s – 4.0×10^4 m/s for an input power

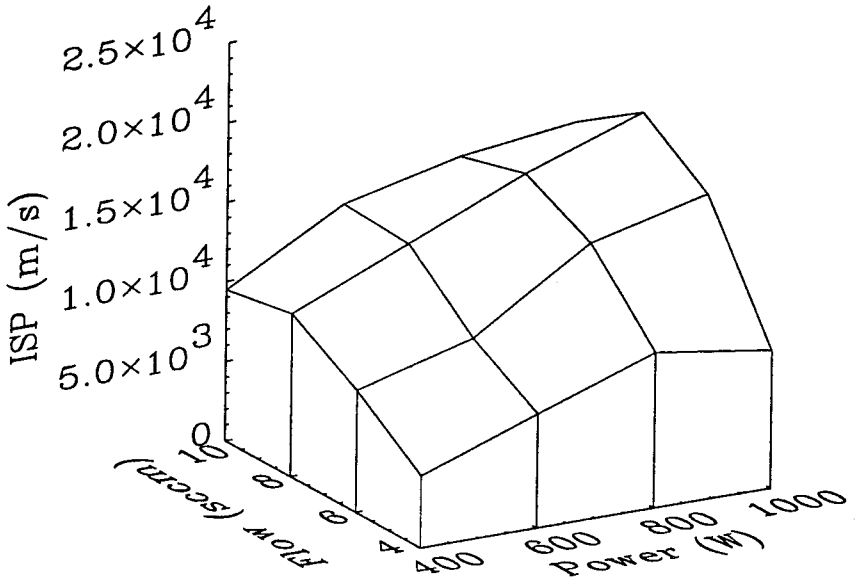

Figure 3-14: Specific impulse.

range of 500 – 900 W, so the ECR device is again less desirable as a propulsion device [7]. To increase the I_{sp} in a significant way, we would have to increase the ion energy by increasing the magnetic field strength at the plasma origin. However, as Chapter 4 shows, a stronger magnetic field would increase nozzle losses which were not considered in the calculations presented in this chapter.

As Figure 3-16 shows, the propulsive efficiency[1] for this experimental thruster is quite poor, especially considering that nozzle losses have been ignored. For comparison, the JPL 15 cm ion engine has an efficiency of 0.52 – 0.66 when operated in a range of I_{sp} from 2.5×10^4 m/s – 4.0×10^4 m/s [7]. The low efficiency of the ECR laboratory device is somewhat expected because the design is intended only for preliminary investigation into the plasma characteristics and is not an iteratively-

[1]The propulsive efficiency is defined as the ratio of the actual thrust to the maximum thrust possible at the given power level and flow rate, the thrust that would occur if all the power were perfectly absorbed by the inflowing gas and converted to axially directed flow.

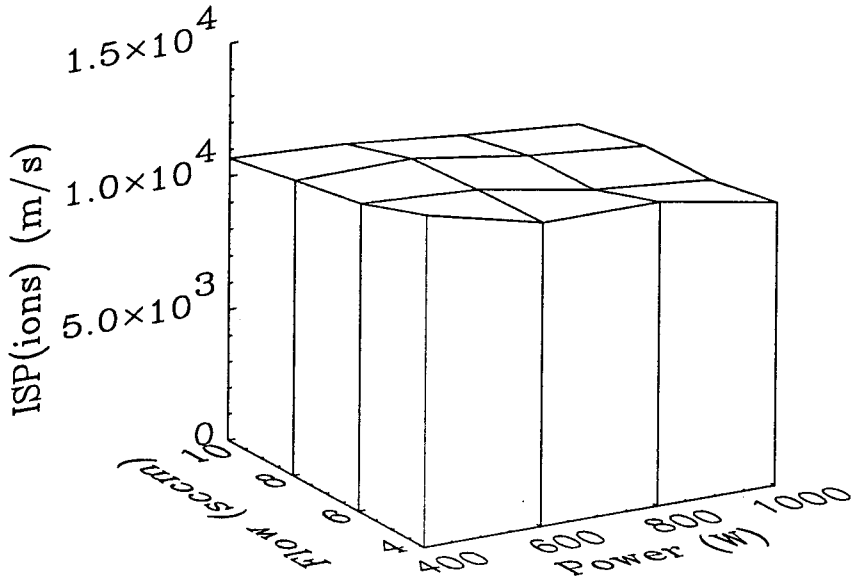

Figure 3-15: Calculated specific impulse using the measured ion mass flux.

developed thruster like the ion thruster in the comparison. Loss mechanisms for the ECR device include upstream loss of plasma due to the low mirror ratio between the ECR region and the dielectric window, radial diffusion to the tank walls, and loss of microwave power through reflection and transmission through the plasma. It appears that the microwave power level has little effect on the propulsive efficiency.

It is difficult to judge the accuracy of the calculated performance parameters due to the effects of the background pressure in the vacuum tank. The background gas artificially increases thrust and efficiency by increasing the plasma flux, but it also retards the ion energy through collisions. It is suspected, however, that the overall effect of elevated tank pressure is to increase the apparent efficiency of the thruster. Further tests of the ECR concept in a vacuum facility with a greater pumping capacity are necessary to provide a better estimate of thruster performance. Despite the advantages of an electrodeless thruster, much improvement in performance must be

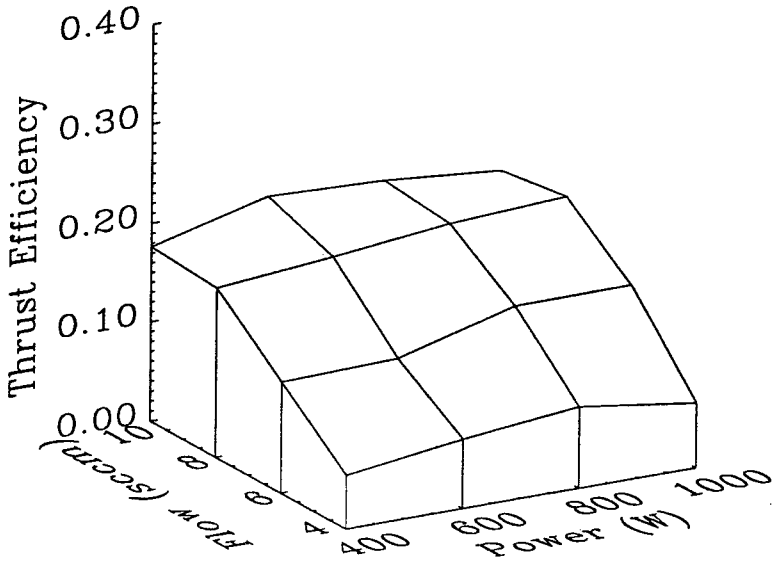

Figure 3-16: Propulsive efficiency.

realized before the ECR concept can compete with electrostatic thrusters for low-thrust, high I_{sp} applications.

3.4 Plasma Potential Measurements

To further investigate the ECR plasma thruster, an emissive probe was used to measure the plasma potential over a range of thruster operating conditions. A typical plasma potential profile is shown in Figure 3-17. These measurements were made by traversing the probe in a grid pattern in the plasma. The scatter in the data is believed to be the result of momentary fluctuations in the plasma. The plasma is generated in the upper left region in the plot, with the plume extending toward the lower right. As Figure 3-17 shows, the plasma potential has little variation in the radial direction and decreases steadily in the axial direction. The slope of the plasma

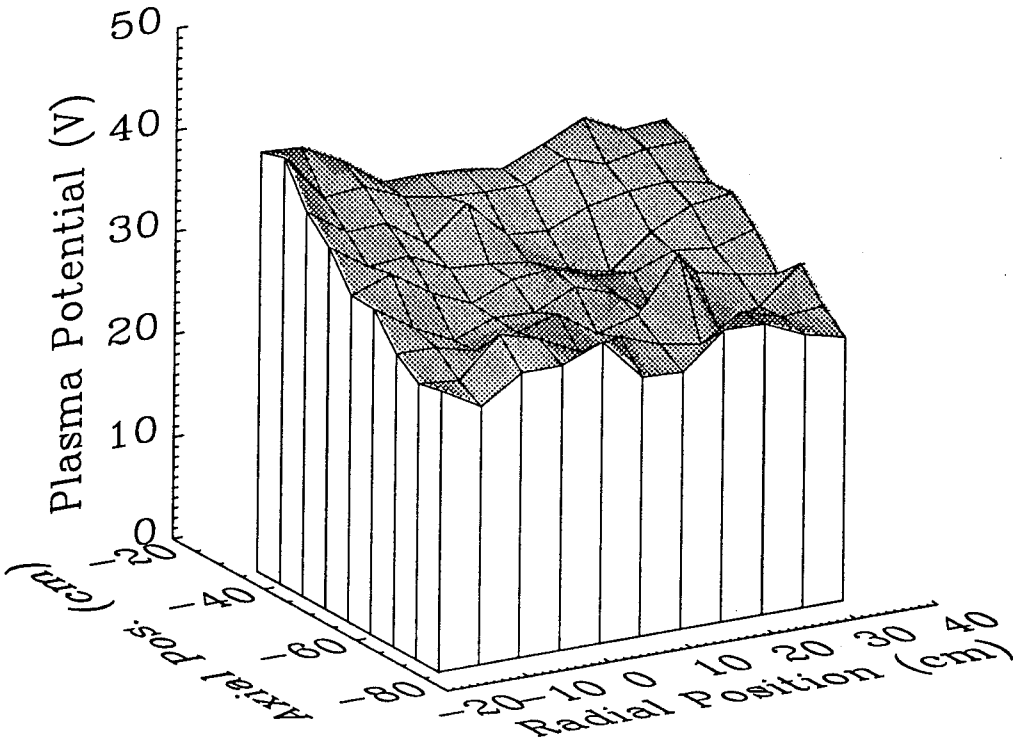

Figure 3-17: Spatial map of plasma potential.

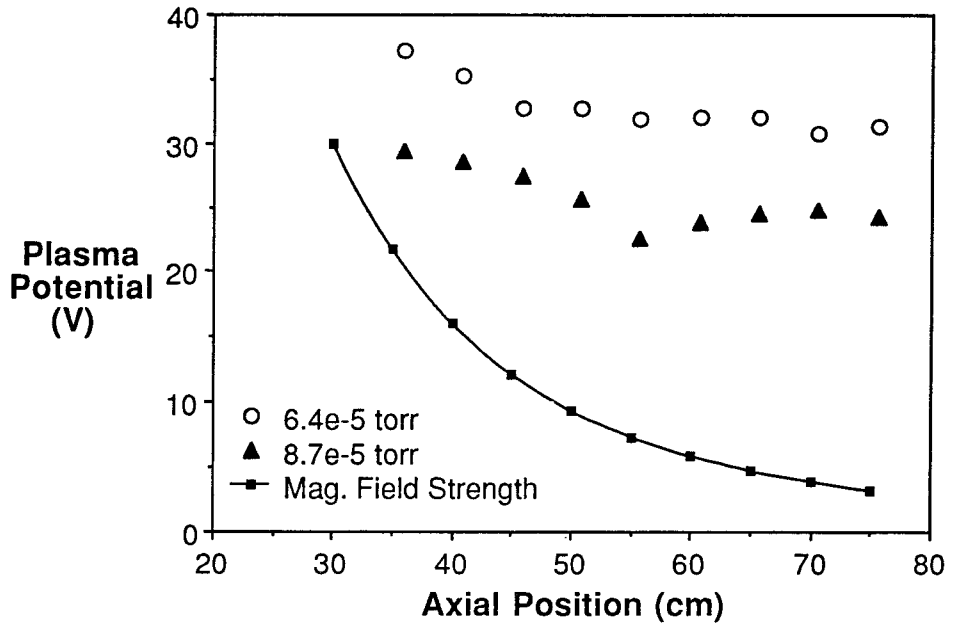

Figure 3-18: Axial variation in plasma potential on the thruster axis for different pressures.

potential appears to be constant away from the ECR region, indicating a constant axial electric field which accelerates the ions. The general shape of this profile seems not to be affected by the pressure or microwave power level. In similar experiments with different operating conditions, the radial invariance and axial slope of the profile is very similar to that shown in Figure 3-17, but the plasma potential at all locations may be shifted higher or lower by some factor determined by the conditions of the experiment.

The global shift in the plasma potential can be seen in Figure 3-18. The plasma potential decreases at all axial locations as the pressure increases, but the slope of the potential drop appears unchanged by the pressure increase. In the absence of collisional losses, one would expect that the plasma potential would be proportional to the magnetic field strength. However, the plasma potential does not follow the magnetic field strength in Figure 3-18. It appears that collisions dominate the behavior of the plasma potential in the region shown in the figure. Others [29, 14] have found that

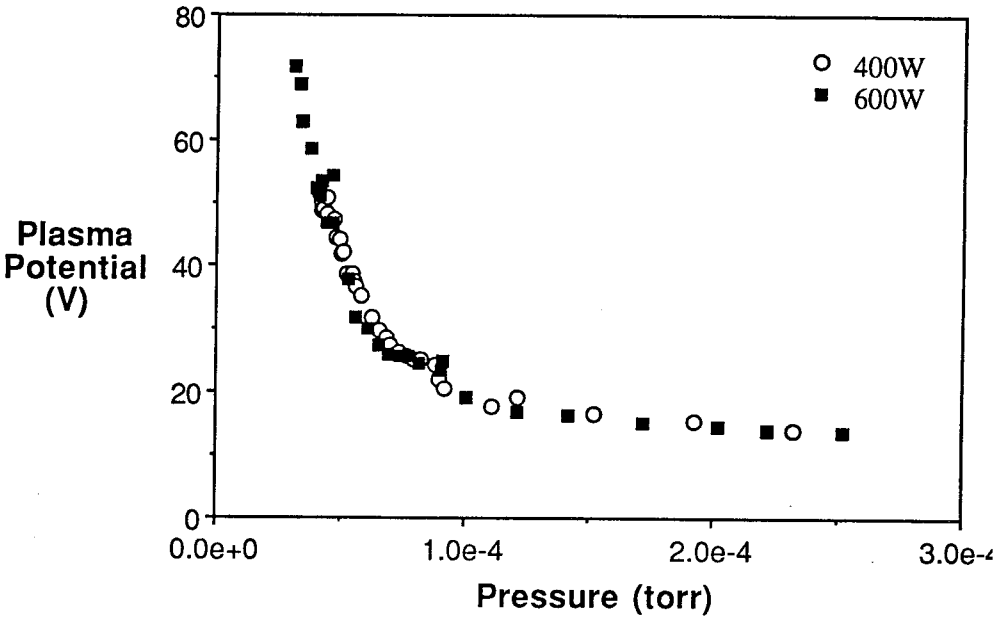

Figure 3-19: Effect of pressure on plasma potential at the thruster axis, 46 cm from the magnet centerplane.

near the ECR region the plasma potential drops proportionately to the magnetic field strength, but further into the expansion region the gradient in the plasma potential flattens out. It is believed that the data presented here represents the latter region only.

The effect of tank pressure is also evident in Figure 3-19 which was taken at a fixed location in the plasma while the flow rate increased. For both microwave power levels shown, the plasma potential decreases sharply as the vacuum pressure increases. Therefore, at extremely low pressure, we would expect much higher ion energies than we saw in Section 3.2. The ions would fall from the elevated plasma potential at the thruster to zero far away. Unfortunately, due to instability of the plasma at low pressures, measurements of the ion energy at pressures below 5.0×10^{-5} torr were unobtainable. Plasma potential measurements were possible to pressures below 4.0×10^{-5} torr because the plasma was apparently stabilized by the electrons from emissive probe. Further experiments with a vacuum facility capable of lower pressures

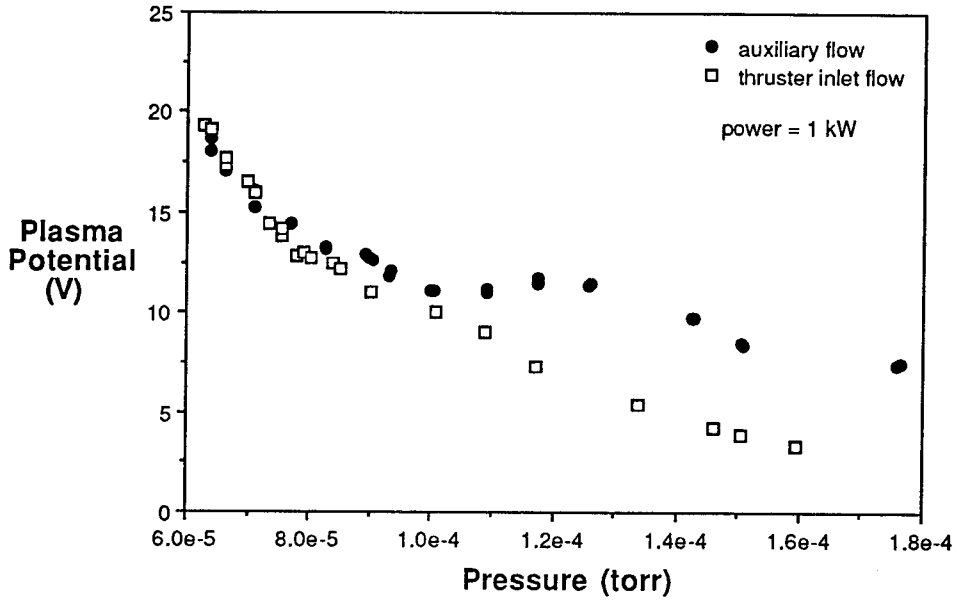

Figure 3-20: A comparison of the effect of pressure due to auxiliary flow and thruster inlet flow on the plasma potential at the thruster axis, 48 cm from the magnet centerplane.

are needed to obtain a better estimate of the plasma potential (and therefore ion acceleration) that could be attained in space.

In Figure 3-20 the effect of the background pressure in the vacuum tank is examined. In both sets of data the plasma potential is plotted against the pressure, but in one case argon gas was added to the thruster upstream from the ECR region, and in the other, the argon was added remotely through the side of the vacuum tank as described in Chapter 2. The two methods of controlling the pressure seem to be equivalent for low pressures, but when the pressure reaches 9×10^{-5} torr, the two curves diverge. The plasma potential is clearly higher when the inflowing gas is injected remotely than when it is added upstream from the ECR region.

The reason for this difference is unclear, but several possibilities exist. Near the ECR region the local density will be higher when the gas is injected at the thruster than when the inlet is away from the thruster. Therefore, the Debye length will

be shorter just downstream from the ECR region with thruster inlet flow. With a shorter Debye length, electric fields near the ECR region will be neutralized more effectively by the plasma. This may be the reason that the plasma potential measured downstream is lower when the gas is injected directly into the thruster.

However, as we saw in Section 3.1, the ion current was unaffected by the location of the gas inlet. To maintain the same ion flux when there is a remote gas inlet, plasma must be created downstream from the ECR region to make up for the decreased density in the ECR region. It may be that the downstream creation of plasma causes the plasma potential to remain higher than when the bulk of the plasma is created in the energizing zone.

The reason for the divergence of the curves at 9×10^{-5} torr may be the onset of a pressure gradient between the gas inlet and the pressure transducer. As the pressure increases inside the tank, the flow rate to the pump increases. At higher pump flow rates, a steeper pressure gradient will form between the gas inlet and pump, and the pressure drop between the gas inlet and the bulk of the plasma will be larger. We will assume that the measured pressures are approximately the bulk tank pressure. The pressure gradient between the gas inlet and the bulk may be large enough at 9×10^{-5} torr that for the same measured tank pressure, the local density in the ECR region is significantly higher when the gas inlet is at the thruster. With a difference in local plasma density at the thruster depending on the location of the gas inlet, the curves in Figure 3-20 diverge.

While pressure greatly affects the plasma potential, Figure 3-19 shows that the plasma potential is nearly the same for two different power levels over the whole range of pressures. The intensity of the microwave beam seems to have little effect on the plasma potential. This conjecture is confirmed in Figure 3-21 which shows that for a fixed flow rate, changes in input microwave power up to 3 kW negligibly affect the plasma potential. This corroborates the results of Section 3.2 in which we saw that the ion energy was independent of microwave power. The added power increases the

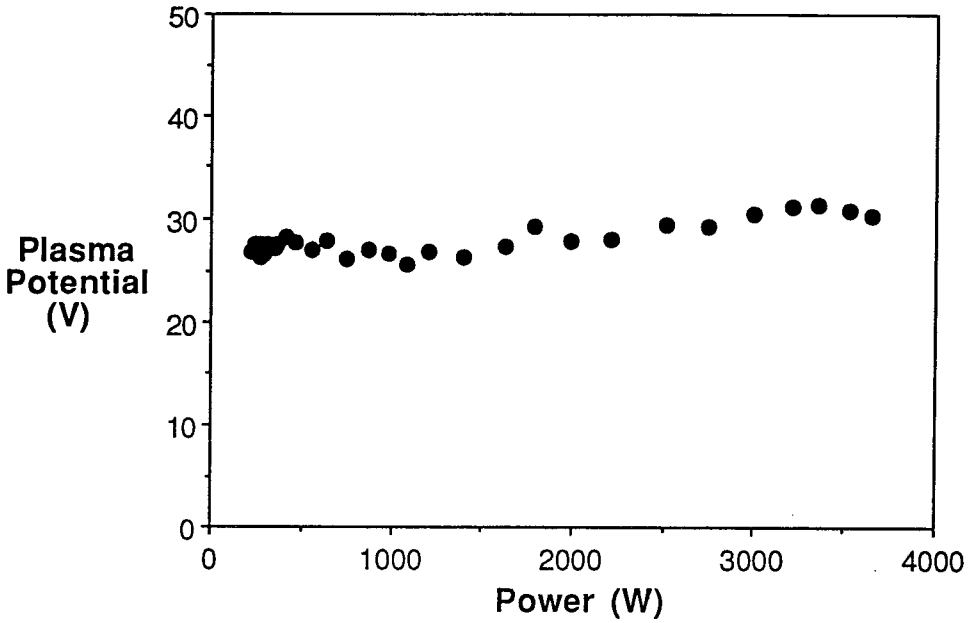

Figure 3-21: Effect of input power on plasma potential for 7 sccm propellant flow, at the thruster axis, 58 cm from the magnet centerplane.

plasma density as we saw in Section 3.1 or is dissipated without being transferred to the electrons or ions. We will see results of microwave reflection and transmission experiments in Section 3.6 that suggest that much of the power is lost by transmission of the microwave beam through the plasma and reflection from the ECR region.

3.5 Electron Temperature Measurements

Two cylindrical Langmuir probes were used to measure the parallel and perpendicular components of the electron temperature (T_e). A plot of the parallel electron temperature ($T_{e_\parallel}$) profile in the plasma is shown in Figure 3-22. Toward the ECR region (off the axial scale of the figure at approximately -10 cm), $T_{e_\parallel}$ is maximum on the thruster axis and decreases sharply in the radial direction. As the plasma diverges into the tank, $T_{e_\parallel}$ decreases in the axial direction. Spreading of the plume is evident as the radial drop in $T_{e_\parallel}$ disappears as the plasma moves into the tank. The

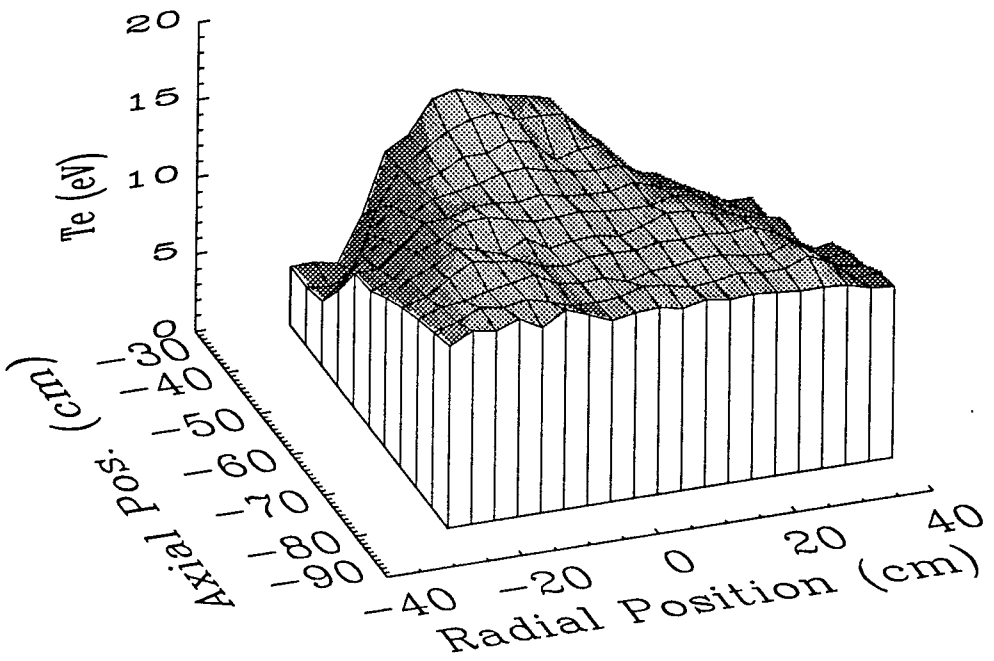

Figure 3-22: Parallel electron temperature profile for 6 sccm, 800 W.

axial drop in $T_{e\|}$ agrees with measurements taken along the axis of a similar device by Miller, Bethke, and Crimi [29].

In Figure 3-23 we see that the perpendicular electron temperature ($T_{e\perp}$) profile is similar to the $T_{e\|}$ profile. Near the ECR region, $T_{e\perp}$ is greater than $T_{e\|}$, but the difference disappears farther into the tank. The initial disparity and subsequent convergence of the two temperatures is shown more clearly in Figure 3-24. As the plume diverges into the tank, the gap between the temperatures shrinks, and at approximately 50 cm downstream from the centerplane of the magnet, the parallel and perpendicular temperatures are the same to within experimental uncertainty. It appears that perpendicular temperature is transferred to parallel temperature as the plasma moves downstream. A likely mechanism is energy transfer through collisions. In the collisionless case, as cyclotron energy was transferred to axially directed kinetic energy through the dipole moment effect, $T_{e\perp}$ would decrease while $T_{e\|}$ would increase.

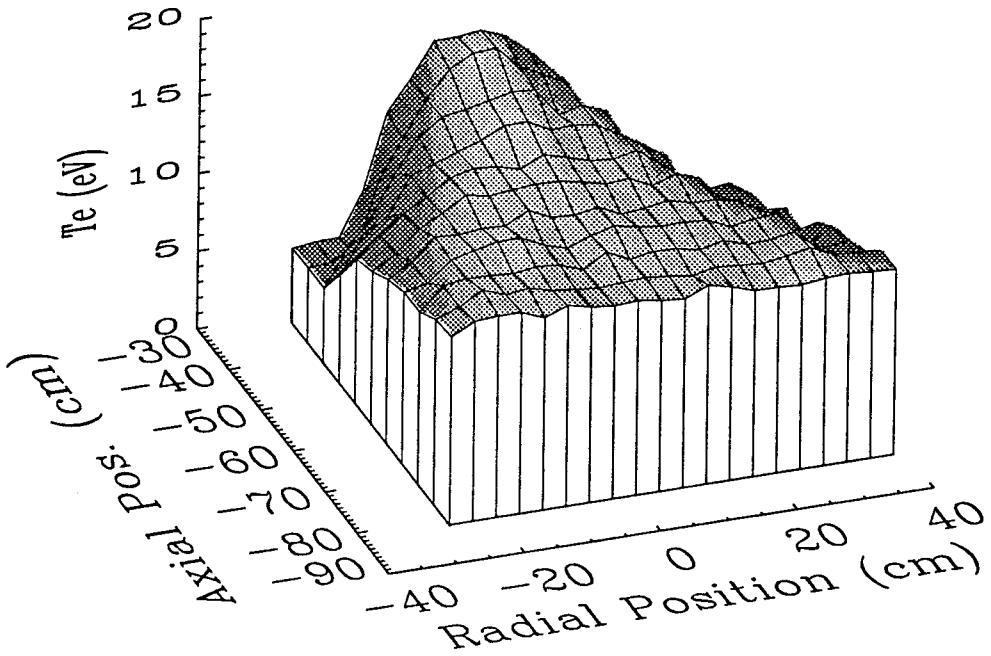

Figure 3-23: Perpendicular electron temperature profile for 6 sccm, 800 W.

Collisions are necessary to equilibrate the parallel and perpendicular components of T_e.

In Figure 3-25 we see that, like plasma potential and ion energy, both components of T_e decrease as the flow rate and pressure increase. The data in Figure 3-25 are for a fixed location in the plasma with variable flow rate to the thruster inlet. As the pressure increases, collisions become more frequent, and the electrons lose energy before they reach the probe resulting in a lower electron temperature at the probe. Further studies at lower pressure would be valuable in obtaining a better estimate of $T_{e_\parallel}$ and $T_{e_\perp}$ that could be attained in a working thruster.

In Figure 3-26 we examine the effect of changing the location of the gas inlet. The electron temperature (in this case $T_{e_\perp}$) seems to be independent on the source of the added flow. As Figure 3-26 shows, $T_{e_\perp}$ falls at approximately the same rate whether the gas enters the tanks at the thruster or the auxiliary inlet. It appears that the

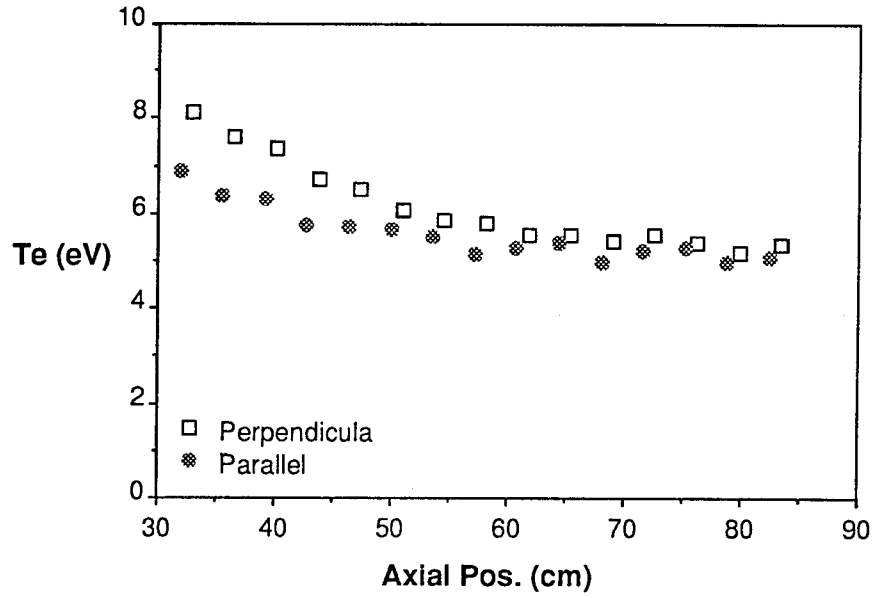

Figure 3-24: Comparison of axial variation in parallel and perpendicular electron temperatures at 6 sccm, 600 W.

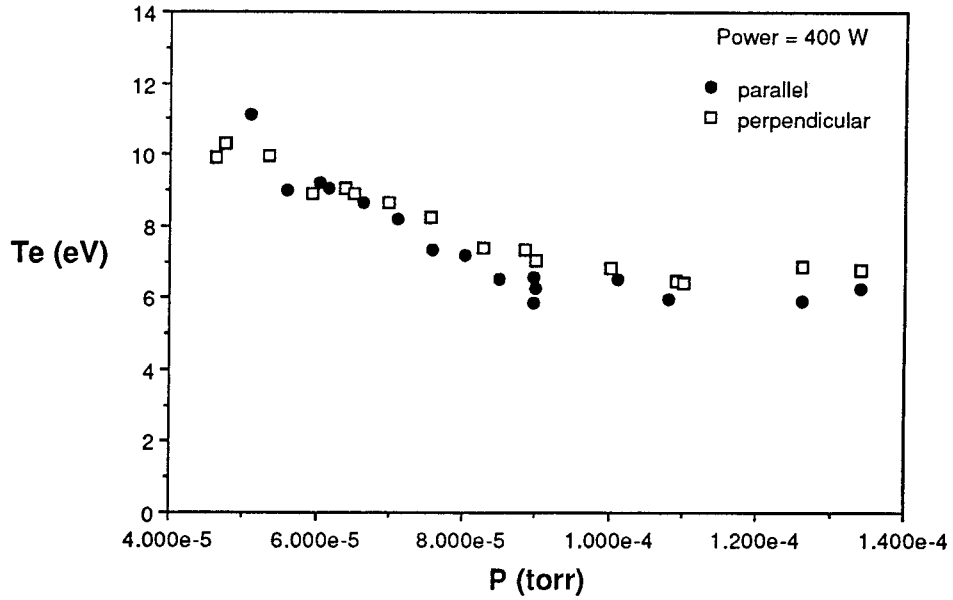

Figure 3-25: Effect of pressure on parallel and perpendicular components of electron temperature at 46 cm from the magnet centerplane.

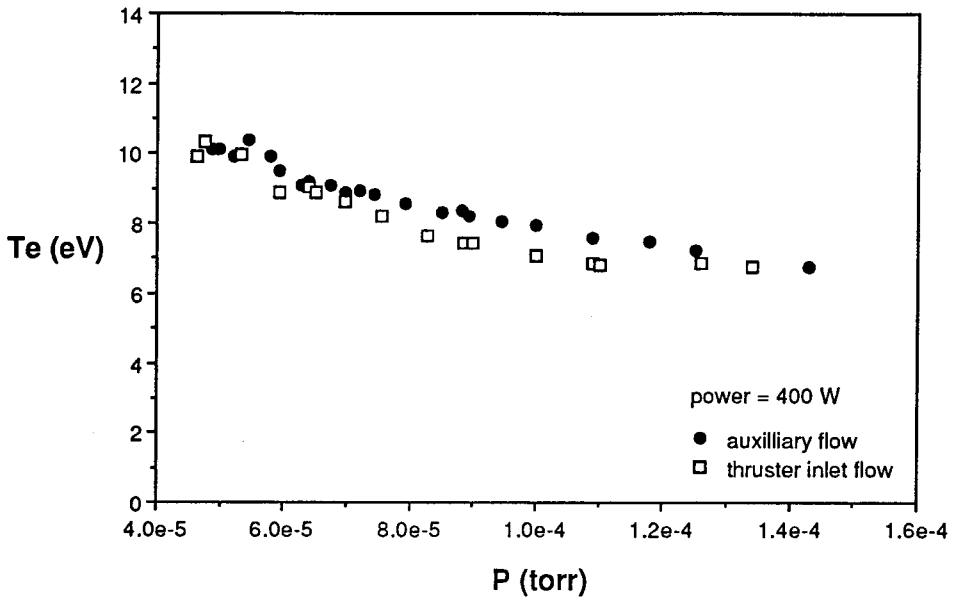

Figure 3-26: Effect of pressure on $T_{e_\perp}$ at the thruster axis, 46 cm from the magnet centerplane. A comparison of thruster inlet flow to auxiliary flow.

bulk pressure in the tank determines the electron temperature. This may be because the local density in the plume has little effect on electron temperature, or possibly because the difference in temperature is undetectable since $T_{e_\perp}$ is a weaker function of pressure.

The effect of power on both $T_{e_\parallel}$ and $T_{e_\perp}$ is shown in Figure 3-27. For low pressures both temperatures are invariant with power level, but as the power increases, both temperatures drop off rapidly. It may be that the decrease in temperature at the higher power levels is due to the increase in plasma density in the ECR region that occurs when the power increases. As the plasma density increases, the collision frequency increases resulting in a greater rate of heat transfer between electrons, ions, and neutrals. The electron temperature would then decrease as the power increases.

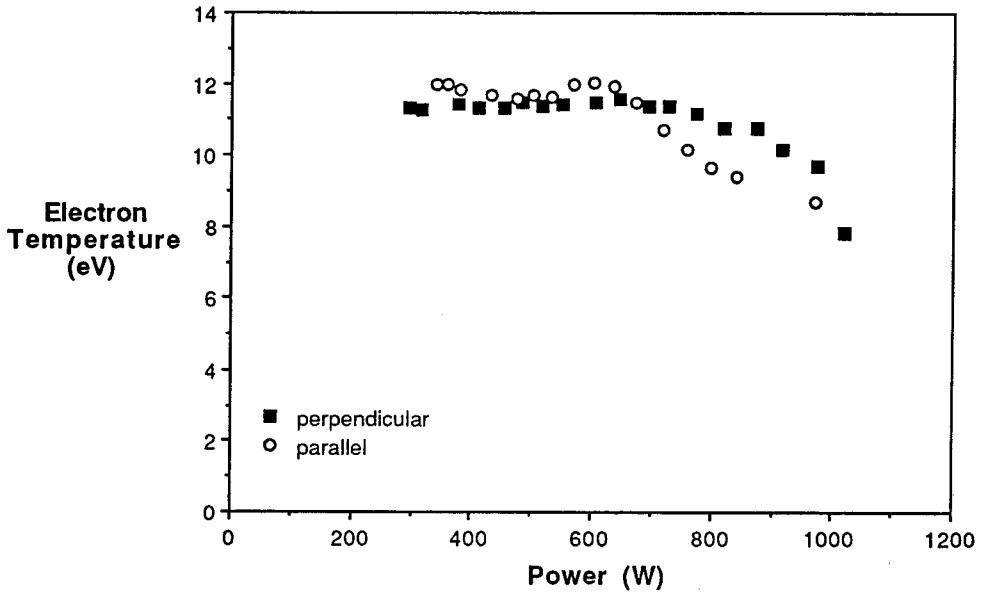

Figure 3-27: Effect of increasing power on T_e at the thruster axis, 46 cm from the magnet centerplane.

3.6 Microwave Power Reflection and Transmission Studies

3.6.1 Modifications to Experiment

Several alterations were made to the experiment for measurements of the microwave power transmitted through the ECR region. An aluminum microwave antenna, shown schematically in Figure 3-28, was mounted on the movable diagnostic arm. The antenna is designed to measure the microwave power at 2.115 GHz when mounted on the end of a rectangular waveguide. In this application the open end of the antenna housing was directed toward the microwave beam so that the axis of the antenna was parallel to the waveguide. The intent was to measure the power density of only the axially directed microwave radiation emitted from the waveguide and to exclude the radiation reflected from the metal vacuum tank surfaces.

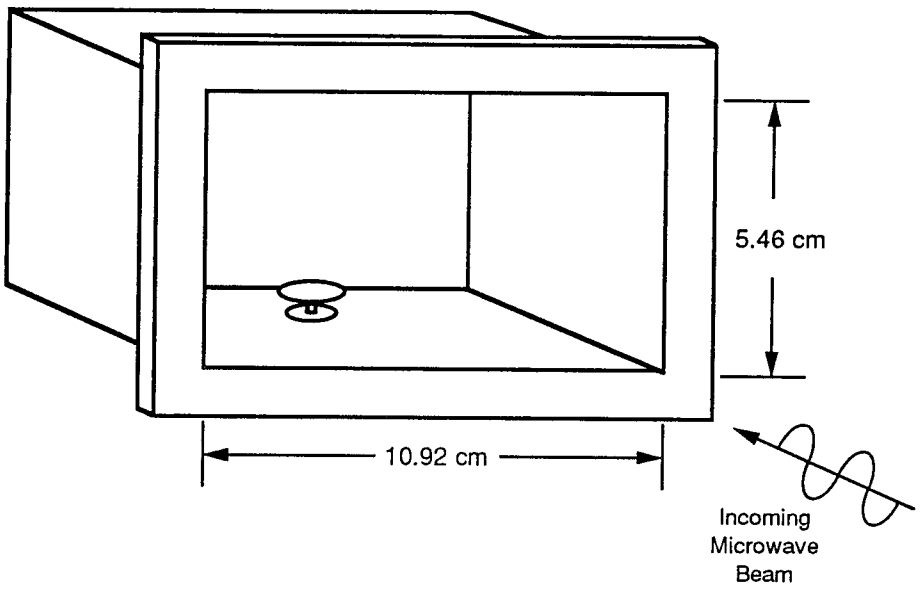

Figure 3-28: Schematic of microwave antenna.

To further reduce the effects of the radiation reflected inside the vacuum chamber, microwave absorber was placed inside the tank as shown in Figure 3-29. The absorber was composed of carbon foam pyramids (2 in. square base and 5.0 in. tall) mounted on foam padding. The absorber was secured to the face and walls of the narrow section of the vacuum tank around the thruster with double-sided tape. The absorber and tape were not designed for high vacuum use, and as a result, the pressure in the vacuum tank increased greatly due to outgassing. The ultimate vacuum with no propellant flow was approximately 1×10^{-4} torr with the absorber compared to approximately 1×10^{-5} torr without the absorber. Also, when the plasma plume was in operation, additional outgassing due to heating of the absorber caused the pressure to increase further. As a result, the results of the transmission studies are difficult to compare to the results of the reflection and other studies due to the disparity in pressures.

Regardless of its effect on the pressure, the absorber was necessary for the measurements of microwave transmission. Without the absorber, radiation reflected from

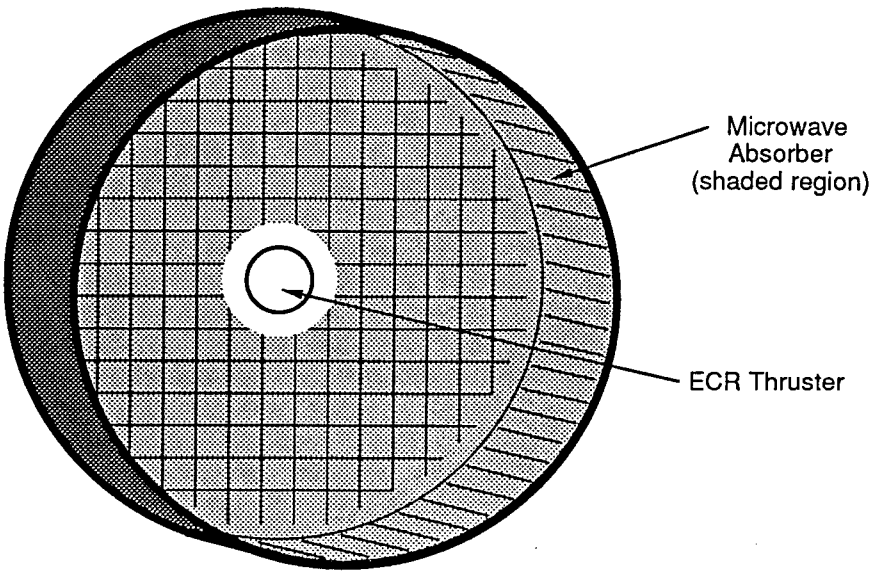

Figure 3-29: Schematic of microwave absorber in small portion of vacuum tank.

the back of the tank to the face of the tank and was eventually collected at the antenna. A comparison of the power density profile measurements with and without absorber is shown in Figure 3-30. The plasma and applied magnetic field were both turned off during the measurements. The power measurements were normalized by the total input power for the data presented in this figure and those below.

The erratic data seen in the no-absorber curve in Figure 3-30 contrasts sharply to the single peak obtained with the absorber. Ideally, in the absence of secondary reflection, the power density profile of the beam will peak at the center of the waveguide and decrease in the radial direction [32]. With the absorber, the power density measurement is similar to the expected profile as shown in the figure. Without the absorber the power density measurements are inconsistent with expectations indicating severe tank reflection effects. The absorber, while detrimental to the quality of the vacuum, significantly reduced the effects of secondary reflection on the power density measurements.

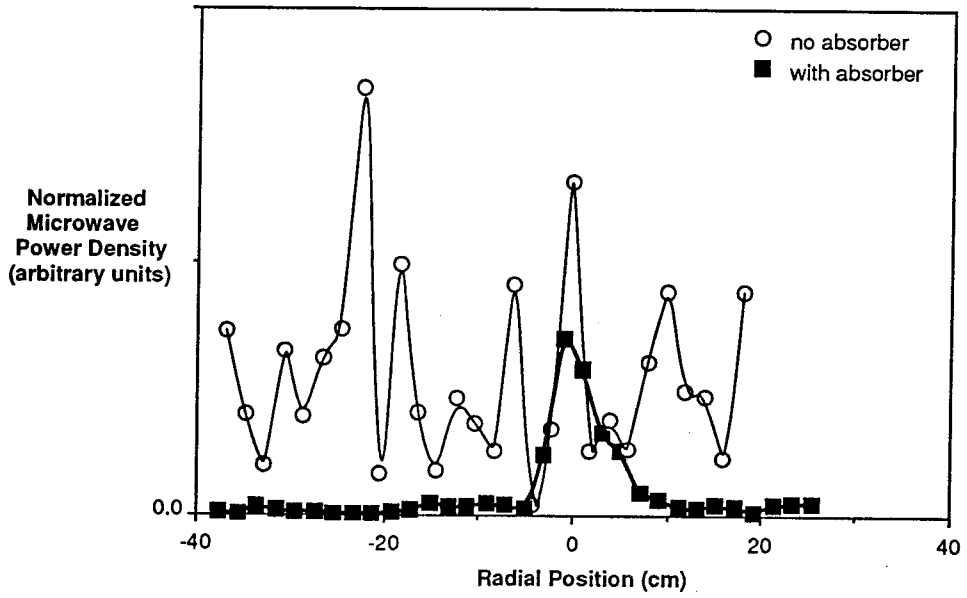

Figure 3-30: Comparison of microwave power measurements with and without absorber 38 cm from the window.

For measurements of the microwave power reflected from the plasma, no modifications to the experimental apparatus described in Chapter 2 were necessary. The reflected power was measured by the power meter at the directional coupler as shown in Figure 2-1.

3.6.2 Transmission Measurements

A normalized plot comparing the power density profiles measured with and without a plasma plume is shown in Figure 3-31. Since some of the input power is absorbed in the ECR region to create the plasma, the normalized power density must be lower when the plasma is activated. However, the curves in Figure 3-31 indicate that with a plasma plume, a larger fraction of the input power is transmitted to the antenna. The power density in the entire vacuum tank cannot be increased by the plasma, so the plasma must affect the microwave beam in such a way that the microwave

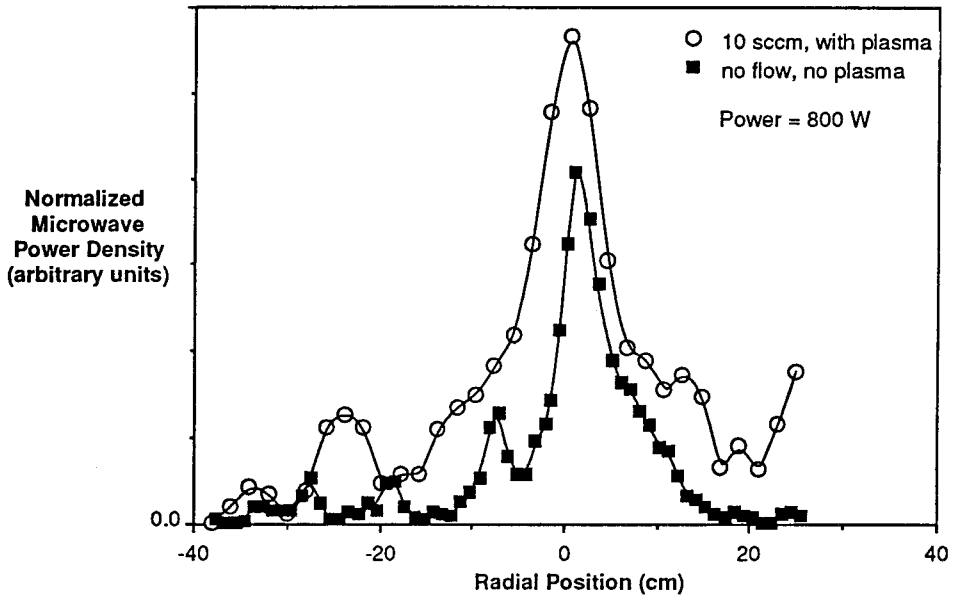

Figure 3-31: Evidence of excess transmission measurements when plasma is present. Measurements taken 42 cm from the window.

power density is increased at the antenna. Miller et al. [29] noted a similar increase in microwave power density in the vacuum tank when the ECR plasma was activated. They attributed the phenomenon to standing wave effects. While standing wave effects may contribute to the unexpected measurements, we suggest a different mechanism.

During these studies, a portion of the plasma was observed to be attached to the antenna. The plasma appeared brighter in a tube extending from the ECR region to the edges of the antenna housing. The reason for this is unknown. If the antenna were ferrous, the magnetic field would be altered by the metal and possibly cause a disturbance in the plasma. However, the antenna was confirmed to be aluminum throughout. Whatever the cause of the change in the plasma, it is believed that the altered plasma may have directed a portion of the transmitted microwave beam towards the antenna. With the microwave beam so altered, the measured microwave power density at all locations in the tank would be greater than

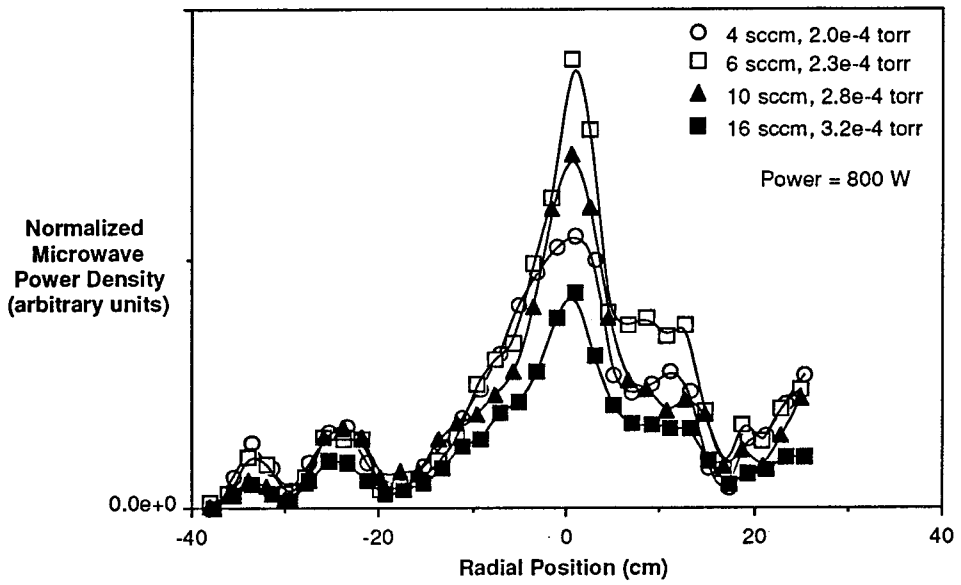

Figure 3-32: Effect of propellant flow rate on normalized microwave power density profile across the plume, 42 cm from the window.

the unaltered power density in the absence of the disturbance. This could explain the additional microwave power measured at the antenna in the presence of the plasma. Although the total fraction of the input power reaching the tank was lower when the plasma was activated, a larger fraction of that power may have been focused to the antenna by the plasma tube connected to the probe housing. Regardless, the cause of the excess power measurements, the results presented here may only be regarded as qualitative due to the observed effect of the plasma on the measurements of the transmitted microwave power.

The measured normalized power density across the plasma plume at several different flow rates is shown in Figure 3-32. We would expect that as the flow rate is increased, the plasma density would increase, and less microwave power would be transmitted past the ECR region. However, as the flow rate increases from 4 sccm to 6 sccm in Figure 3-32, the fraction of the input power measured at the antenna increases. It may be that this increase is the result of the same effect that caused the

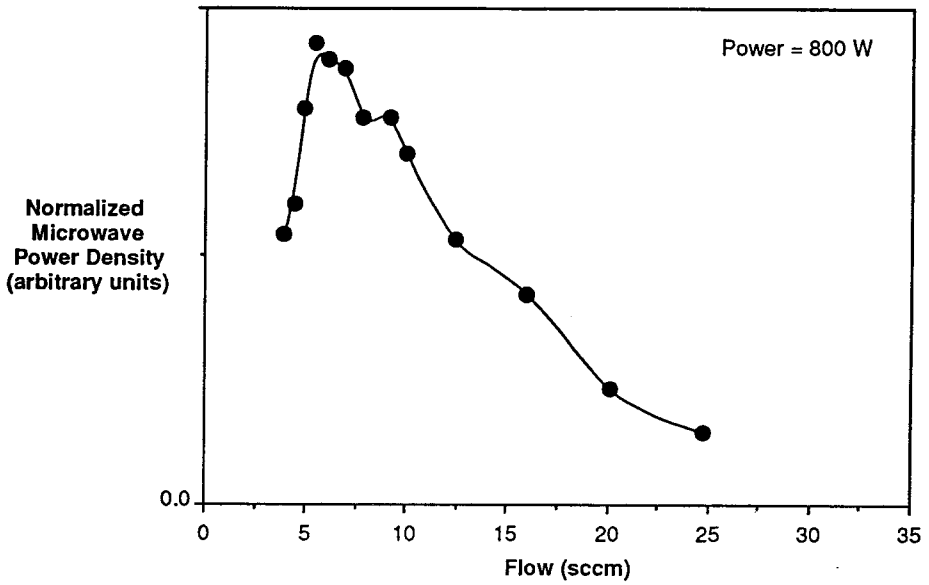

Figure 3-33: Effect of propellant flow rate on normalized microwave power density at the thruster centerline, 42 cm from the window.

excess power measurements seen in Figure 3-31 when the plasma was activated. Conversely, as the flow rate increases from 6 sccm to 10 sccm and 16 sccm, the measured power density decreases. It appears that at the higher flow rates a larger fraction of the microwave power is either absorbed or reflected at the ECR region.

The effect of increased flow rate and pressure can be seen in more detail in Figure 3-33. For the figure the position of the antenna was fixed along the thruster axis at 42 cm from the window while the propellant flow rate was varied. As the flow rate increases from 4 sccm, the measured normalized power density increases to a peak at approximately 7 sccm. Above 7 sccm the power density steadily decreases and appears to approach zero, indicating that only a small fraction of the microwave power is transmitted through the plasma at very high flow rates.

Since we have seen that the power density measurements are elevated by the effects of plasma, we may make only qualitative conclusions here. It appears that at lower flow rates and pressures (below approximately 10 sccm and 2.8×10^{-4} torr), a

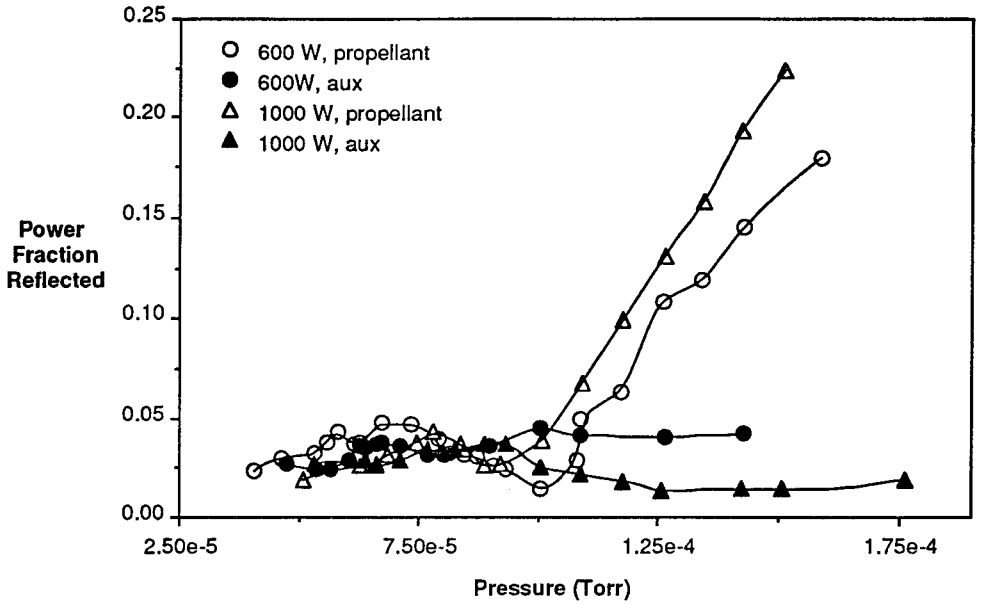

Figure 3-34: Effect of pressure on microwave reflection.

significant fraction of the input microwave power is transmitted through the plasma. However, when the propellant flow rate and pressure reach higher values, nearly all the microwave power is either reflected or absorbed by the plasma near the ECR region.

3.6.3 Reflection Measurements

The fraction of the input microwave power reflected back to the directional coupler is shown in Figure 3-34 for several conditions. In the curves marked "aux" the pressure was controlled by injecting argon flow through the remote auxiliary flow inlet. In the curves marked "propellant," the pressure was controlled by injecting the argon directly at the thruster through the propellant injector holes. The reflection was measured at two power levels for the two methods of increasing the tank pressure. As the figure shows, for the two runs in which argon gas was injected into the tank through the auxiliary flow port, the fraction of power reflected remains nearly constant

over the entire pressure range for both power levels. In contrast, when the argon is introduced at the thruster as propellant, the reflected fraction of the microwave power increases sharply at approximately 1×10^{-4} torr for both 600 W and 1000 W. At 1.5×10^{-4} torr and 1000 W, reflected power is approximately 23% of the total power supplied to the thruster.

It is believed that the reason for the difference between the auxiliary flow and propellant flow cases is the difference in pressure and density near the window. When the argon gas enters the tank through the auxiliary flow port, the pressure near the window should be approximately the bulk pressure of the tank. However, when the gas is injected through the inlet holes at the window as a propellant, the pressure at the window will be greater than the measured tank pressure. When the pressure reaches approximately 1×10^{-4} torr and the gas is injected directly to the thruster, the higher density plasma at the window reflects the microwave beam.

It may be that the plasma frequency at the ECR region reaches the microwave frequency when the bulk tank pressure reaches 1×10^{-4} torr. Any additional increase in plasma density (and therefore plasma frequency) would then decrease the penetration distance of the microwave beam into the plasma. As a result more of the microwave beam may be reflected causing the increase in the reflection seen in Figure 3-34 for the cases in which the flow is injected at the thruster. The plasma frequency is given by

$$\omega_p = \left(\frac{n_0 e^2}{\epsilon_0 m_e} \right)^{\frac{1}{2}} \tag{3.2}$$

where n_0 is the plasma density and ϵ_0 is the permittivity of free space. The plasma frequency increases with the plasma density, and it equals the microwave frequency, 2.12 GHz, when the plasma density is 5.5×10^{16} m^{-3}. If the temperature at the ECR region is 20 eV, the pressure would be 1.3×10^{-3} torr at a density of 5.5×10^{16} m^{-3}. For comparison the density in the bulk of the tank at 1×10^{-4} torr assuming a temperature of 293 K is 3.3×10^{18} m^{-3}. Considering these calculations, it seems possible that the plasma frequency at the ECR region equals the microwave frequency

when the pressure reaches approximately 1×10^{-4} torr and the gas is injected directly to the thruster.

3.6.4 Summary and Conclusions of Microwave Transmission and Reflection Studies

The measurements of transmitted microwave power were greatly affected by the presence of the plasma. The excess power received by the antenna in the presence of the plasma makes the results difficult to analyze. In addition, the elevated pressure due to the microwave absorption material makes quantitative conclusions difficult. Because of the effect of the plasma, it is unclear how much of the microwave beam is transmitted through the ECR region at low flow rates. However, the measurements indicate that as the propellant flow rate increases, a smaller percentage of the input microwave power reaches the vacuum tank. It appears that at very high flow rates only a small fraction of the microwave beam is transmitted through the ECR region.

The results of the reflection studies correlate with the conclusions of the transmission studies. At low pressures and flow rates, less than 5% of the input power is reflected back through the waveguide, but as the propellant flow rate increases, a sharp increase in reflection is noted at approximately 1×10^{-4} torr. At higher pressures and flow rates the reflected power reaches 23% of the input power. It may be that the plasma density is high enough that the plasma frequency equals the microwave frequency when the reflection begins to increase. When the pressure in the vacuum tank is controlled by injecting argon remotely from the thruster, no increase in reflection is observed.

Considering the results of both studies, it seems likely that a large portion of the microwave power is not absorbed by the plasma in the ECR region. The reflection studies indicate that at high flow rates a significant fraction of the input power is lost due to reflection. Unfortunately, since the transmission measurements are elevated by the plasma, we cannot directly make conclusions about the amount of transmis-

sion through the plasma. However, we can gain insight into transmission from the reflection data. At high flow rates much of the power is reflected from the plasma and is not absorbed, but we do not see a decrease in ion flux or energy at high propellant flow rates. Since the energy of the plasma is not noticeably affected by the increase in reflection, it appears that a fraction of the microwave power, similar to the maximum amount reflected, is transmitted through the plasma at low flow rates. In view of these results it seems likely that inefficient absorption of microwave power accounts for much of the energy losses noted in Section 3.3.

3.7 Summary of ECR Experiments

A Faraday cup was used to measure the ion current density in the plasma plume. An annular ion flux occurs at low pressures. As the vacuum tank pressure increases, the ion flux becomes maximum flux at the thruster axis. It may be that electrons from the thruster walls are needed for the plasma to exist at low pressures, but since the magnetic field restricts the electron radial motion at low pressures, the electrons are not able to diffuse to the thruster axis. An annular plasma results. As the pressure and collision frequency increase, the electron radial diffusion rate increases, and a plasma forms across the entire ECR region resulting in an axis-maximum ion flux.

The total ion flux density was obtained by integrating the ion flux density across the plume. The ion flux increases with flow rate and input power until at high flow rates and power levels, the total flux of ions actually exceed the total inflow of argon atoms indicating that background gas is ionized along with the in flowing propellant. For high flow rates, the total ion flux increases in the axial direction indicating that background neutrals may be entrained by the plasma downstream from the ECR region.

A gridded energy analyzer was used to measure the kinetic energy of the ions in the axial direction. The ion KE is maximum along the thruster axis and decreases in the radial direction. The ion energy also decreases as the plasma diverges into the tank apparently due to friction with the background neutrals. The ion energy is invariant with input microwave power, but it decreases with increasing pressure.

Propulsion parameters were calculated from the ion flux and energy measurements. The thrust and efficiency increase with tank pressure and input power. However, increases in the propellant utilization account for the improvement in thrust and efficiency. The performance of the laboratory thruster was poor compared to the JPL 15 cm ion thruster especially considering the enhanced performance of the ECR device due to the additional ion flux from the entrained background neutrals. To provide better projections of thruster performance in a space environment, further

tests at lower pressures are necessary.

An emissive probe was used to measure the plasma potential. The plasma potential decreases axially in the plume but exhibits little radial variation. The plasma potential decreases more slowly in the axial direction than magnetic field strength possibly due to collisions. The plasma potential is invariant with input power, but it decreases with pressure resulting in reduced ion acceleration and thrust.

Langmuir probes were used to measure temperature $T_{e_\parallel}$ and $T_{e_\perp}$ over a range of thruster operating conditions. Like the plasma potential, the electron temperature is unaffected by increasing the input power and decreases with increasing pressure. Near the ECR region, $T_{e_\perp}$ is greater than $T_{e_\parallel}$, but the two components equilibrate as the plasma moves axially away from the thruster.

The microwave power transmitted through the ECR region was measured with a microwave antenna. The measured microwave power at the antenna increases when the plasma is activated. It may be that additional microwave power is focused to the antenna by the plasma. Therefore, we are unable to make quantitative conclusions. However, qualitatively, the measurements indicate that a smaller fraction of the input microwave power is transmitted to the antenna as the propellant flow rate increases. Only a small fraction of the microwave beam is transmitted through the ECR region at high flow rates.

Microwave power reflection was measured at a directional coupler in the waveguide. At low pressures and flow rates, little input power is reflected. However, as the pressure increases, a sharp increase in reflection occurs at approximately 1×10^{-4} torr. Pressure increases above this level, result in reflection of a large fraction of the input power. The increased reflection may be because the plasma frequency reaches the microwave frequency at 1×10^{-4} torr. It seems likely that much of the microwave power is transmitted through the plasma at low pressures because the increased reflection at high pressure does not correspond to a similar decrease in plasma energy at high pressures.

Chapter 4

Collisionless Plasma Detachment Model

The goal of the work described in this chapter is to investigate the effect of a magnetic nozzle on the divergence of an ECR plasma plume. To accomplish this a collisionless cold-plasma model was developed which calculates the trajectory of a coaxial ring of plasma in the magnetic field of a current loop. Because the plasma is modeled as collisionless, electrical resistive effects that enhance detachment of the plasma from the magnetic field and fluid viscous effects that retard detachment are not considered [31].

4.1 Introduction

Applied magnetic nozzles in electric propulsion devices provide control, direction, and acceleration of plasmas without surface-to-plasma contact. Several types of proposed thrusters make use of magnetic nozzles, including applied-field MPD thrusters, coaxial plasma guns [13], and electron-cyclotron-resonance (ECR) thrusters [36]. The benefits include reduced surface degradation, radial containment of the plasma in the generation region, and acceleration of the plasma through the dipole-moment effect. However, for such devices to produce usable thrust, the plasma must detach from the magnetic field. If a portion of the plasma is trapped by the field, it will follow the field back to the spacecraft resulting in spacecraft contamination and no thrust production. In addition the plume must diverge as little as possible so that the entire

thruster is efficient enough for use on a spacecraft.

Finding conditions under which plasma separates sufficiently from the magnetic nozzle after it it leaves the thruster is important for evaluation and design of applied field devices. Because resistive effects enhance plasma detachment and fluid viscous effects retard detachment, it is unknown whether the collisionless model presented here provides conservative estimates of the conditions necessary for separation. We have used the model to calculate the efficiency of magnetic nozzles for different nozzle configurations and plasma conditions.

Others [18, 37] have studied the problem similarly and have found some important parameters which affect separation. Assuming a magnetic nozzle generated by a single current loop and a plasma originating in the plane of the loop, the previous studies suggest that only plasma near the axis of the thruster is able to detach from the field lines. Therefore, only a small fraction of the area of the current loop is available for plasma generation. In this chapter, we use the same cold-plasma model used previously [18, 37] to investigate the effect of other field configurations and ECR locations on detachment. We show that plasma separation can be enhanced by these modifications over that predicted in previous studies.

While detachment is relevant to a number of plasma thrusters, we focus our attention particularly on ECR thrusters. The primary difference between the plasma plume of an ECR thruster and that of other applied field thrusters is the elevated energy of the electrons in the plasma generation region. This energy is held in the electrons' cyclotron motion initially, and the electrons accelerate axially due to the force of the applied field on the induced field of the electrons. The energy is transferred from the electrons to the ions through the ambipolar electric field. As the following results show, by the time the plasma has traveled a few coil radii downstream from the energizing region, most of the energy is converted to ion kinetic energy. Therefore, downstream from the acceleration region, the ECR plasma is similar to plasmas in other devices in which the ions and electrons are closer to thermal equilibrium inside

the thruster.

4.2 Trajectory Equations

To calculate plasma trajectories in a magnetic nozzle, we need to integrate the dynamical equations of motion for the plasma. We will restrict attention to a cold, collisionless plasma and make the noted simplifying assumptions. We take two approaches to the equations. In the first, the plasma ring is initiated with a velocity along the field line without considering the method of acceleration. In the second the plasma is initially at rest and accelerates due to the dipole moment of the electrons. In both approaches, the magnetic nozzle is the field of a single current loop coaxial to the plasma plume, and the field vectors are calculated numerically [21].

Following Hooper [18] we use the simplest approach in modeling a cold plasma and simply start the plasma with an initial velocity $\mathbf{u}_0$ along the magnetic field lines, without specifying the acceleration mechanism. We are neglecting pressure gradient terms in the plasma momentum equation. We then begin with the momentum equation for a single particle (electron or ion) in the plasma.

$$m\mathbf{u} \cdot \nabla \mathbf{u} = q(\mathbf{E} + \mathbf{u} \times \mathbf{B}) \tag{4.1}$$

where $\mathbf{u}$ is the particle velocity, m the particle mass, q the charge on a particle, $\mathbf{E}$ the ambipolar electric field, and $\mathbf{B}$ the magnetic field.

To simplify the results, we impose local quasineutrality ($j_z = j_r = 0$). The ion and electron trajectories are then constrained to be the same except in the azimuthal direction. Therefore, the only currents possible are azimuthal. Hooper [17] has shown that this leads to

$$\tilde{\mathbf{u}} \cdot \tilde{\nabla} \tilde{\mathbf{u}} = -\tilde{\nabla} \left\{ \frac{e^2 \left[\Psi_0 - \Psi(r,z)\right]^2}{2 m_e M_i r^2} \right\} \tag{4.2}$$

where e is the fundamental charge, m_e the electron mass, M_i the ion mass, r the radial

position of the particle, Ψ the magnetic flux function, and Ψ_0 is the flux through a ring of radius r_0 at the initial plasma position (r_0, z_0). The tilde notation denotes a three-dimensional vector without the azimuthal component.

Writing Equation 4.2 in dimensionless form, dropping the tilde notation, and normalizing distances to r_0, following Hooper [18] we get

$$\mathbf{v} \cdot \nabla \mathbf{v} = -\frac{G}{2} \nabla \left[\frac{(1-\psi)^2}{(r/r_0)^2} \right] \tag{4.3}$$

where $\mathbf{v} = \mathbf{u}/u_0$ and $\psi = \Psi/\Psi_0$, and Hooper [17] defined

$$G = \frac{e^2 {\Psi_0}^2}{m_e M_i {r_0}^2 {u_0}^2}. \tag{4.4}$$

In the following results we have solved Equation 4.3 numerically for the velocity using the differential equation solver, LSODE [16].

The dimensionless parameter G is important in determining how a plasma ring will be deflected or trapped by the magnetic nozzle. To better understand this parameter, we examine G in a region in which the magnitude of the magnetic field is approximately constant across the disk bounded by the plasma ring, $B(r, z_0) \approx B_{z_0}$. We can then rewrite Equation 4.4 as

$$G \approx \frac{1}{4} \frac{eB_{z_0}}{m_e} \frac{eB_{z_0}}{M_i} \frac{{r_0}^2}{{u_0}^2}. \tag{4.5}$$

Rearranging further we get

$$G \approx \frac{e^2}{2m_e} (B_{z_0}^2 {r_0}^2) \left(\frac{1}{\frac{1}{2} M_i {u_0}^2} \right). \tag{4.6}$$

The last term in Equation 4.6 is the reciprocal of the initial ion energy, E_i, and we can express $B_{z_0}^2 r_0^2$ in terms of the energy of the applied magnetic field. Let M_b be the energy per unit thickness of an axisymmetric magnetic field, $B(r, z)$, contained in a

ring of radius r_0 at axial position z_0. Then M_b is given by

$$M_b = \frac{1}{2\mu'} \int_0^{r_0} B^2(r, z_0)\, 2\pi r dr \tag{4.7}$$

where μ' is the permeability. If we assume that $B(r, z_0) \approx B_{z_0}$ and $\mu' \approx \mu'_0$, then

$$M_b \approx \frac{\pi}{2\mu'_0} B_{z_0}^2 {r_0}^2. \tag{4.8}$$

So Equation 4.6 becomes

$$G \approx \frac{e^2}{2m_e} \frac{2\mu'_0 M_b}{\pi} \frac{1}{E_i} = \left(\frac{e^2 \mu'_0}{\pi m_e}\right) \left(\frac{M_b}{E_i}\right) = \left(3.54 \times 10^{-14}\,\mathrm{m}\right) \left(\frac{M_b}{E_i}\right). \tag{4.9}$$

For the assumptions given, G is proportional the ratio of the linear magnetic energy density of the nozzle at the plasma origin to the initial ion energy. Examining G at its limits, we see that as $G \rightarrow \infty$ for a given initial position, the magnetic energy is very large relative to the ion energy. The ions are unable to escape from the magnetic nozzle and are trapped. Conversely, as $G \rightarrow 0$ for a given initial plasma position, the plasma kinetic energy is large relative to the magnetic energy. The nozzle is too weak to hold the energetic plasma, and the plasma detaches with no deflection. We will see below how mid-range values of G affect the plasma trajectory, but in general lower values of G are desirable for detachment of the plasma.

We take a second approach to the equations of motion by adding a simple pressure term, $\mathbf{F}_\mu$, to the plasma momentum equation following Sercel [37]. For the electrons this force is given by

$$\mathbf{F}_\mu = \nabla(\vec{\mu} \cdot \mathbf{B}) \tag{4.10}$$

where $\vec{\mu}$ is the dipole moment vector of an electron and $\mathbf{B}$ is the magnetic field vector. The dipole moment vector is given by $-\frac{m_e {v_\perp}^2}{2B}\hat{\mathbf{B}}$ where $v_\perp$ is the component of the electron velocity perpendicular to the magnetic field line, and $\hat{\mathbf{B}}$ is the a unit vector along the magnetic field line. The ions have a large cyclotron radius relative to the

plume dimensions, and the force on their dipole moment is neglected. Since the dipole moment vector is constant in a field changing slowly in space and time and is always directed opposite the magnetic field vector, Equation 4.10 becomes:

$$\mathbf{F}_\mu = \nabla(-\frac{m_e {v_\perp}^2}{2B}\hat{\mathbf{B}}\cdot\mathbf{B}) = -\frac{m_e {v_{0\perp}}^2}{2B_0}\nabla B = -\mu_0 \nabla B. \tag{4.11}$$

With this pressure term (appropriate only for thrusters in which the initial electron dipole moment energy is much greater than the initial ion kinetic energy, such as an ECR thruster), we may start the plasma with zero velocity and allow it to accelerate to its final velocity. Adding the pressure term, following Sercel [37], Equation 4.1 for the electrons becomes

$$m_e \mathbf{u}_e \cdot \nabla \mathbf{u_e} = -e(\mathbf{E} + \mathbf{u}_e \times \mathbf{B}) - \mu_0 \nabla B, \tag{4.12}$$

and for the ions

$$M_i \mathbf{u}_i \cdot \nabla \mathbf{u}_i = e(\mathbf{E} + \mathbf{u}_i \times \mathbf{B}). \tag{4.13}$$

We again apply quasineutrality, following Sercel, so the electrons and ions must have the same radial and axial position as they accelerate away from their origin. We can then eliminate the unknown electric field from the axial and radial components of Equations 4.12 and 4.13. Solving for the three components of velocity for the ions and electrons, Sercel [37] has shown that Equations 4.12 and 4.13 yield:

$$\ddot{r} = \frac{erB_z(\dot{\theta}_i - \dot{\theta}_e) - \mu_0 \frac{\partial B}{\partial r} + r(m_e \dot{\theta}_e^2 + M_i \dot{\theta}_i^2)}{m_e + M_i} \tag{4.14}$$

$$\ddot{z} = \frac{erB_r(\dot{\theta}_e - \dot{\theta}_i) - \mu_0 \frac{\partial B}{\partial z}}{m_e + M_i} \tag{4.15}$$

$$\ddot{\theta}_e = \frac{e}{m_e r}(B_z \dot{r} - B_r \dot{z}) - \frac{2\dot{r}\dot{\theta}_e}{r} \tag{4.16}$$

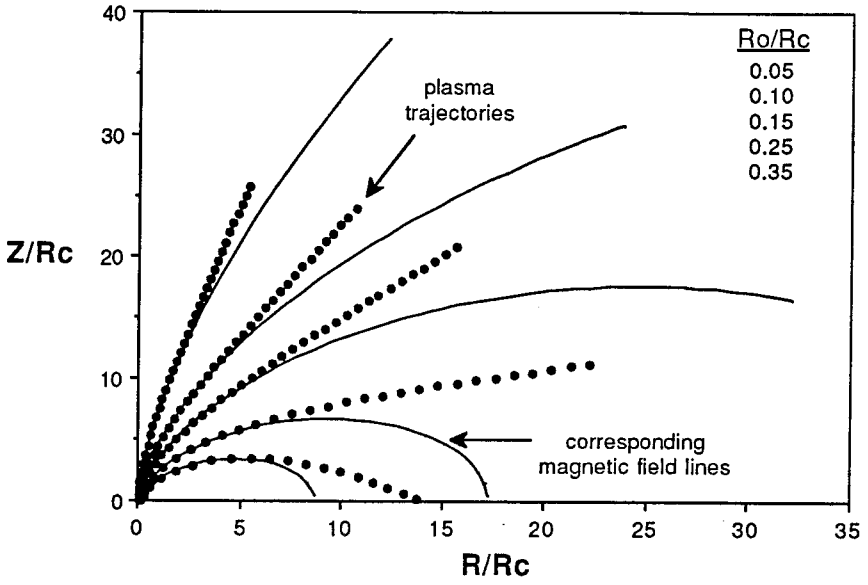

Figure 4-1: Plasma trajectories for 200 eV.

$$\ddot{\theta}_i = \frac{e}{M_i r}(B_r \dot{z} - B_z \dot{r}) - \frac{2\dot{r}\dot{\theta}_i}{r}, \tag{4.17}$$

where $r = r_e = r_i$ is the plasma radial position, $z = z_e = z_i$ the plasma axial position, and θ_e and θ_i the electron and ion azimuthal positions, respectively. We solve Equations 4.14-4.17 using LSODE [16] as before. We then obtain a second set of predictions for the trajectories of a plasma ring in a magnetic nozzle, but in this case diamagnetic acceleration of the electrons is included in the model.

We examine both approaches below, and show that the predicted trajectories and conclusions about plasma detachment from the magnetic field are the same for both models.

4.3 Results

Calculated plasma trajectories are shown in Figure 4-1 with distances normalized to the radius of the magnet current loop, r_c. Diamagnetic acceleration was included in

the calculations, and the initial energy and magnetic field strength were chosen to be similar to those found in an experimental ECR thruster [23]. The magnetic field is .072 tesla at the center of the magnet current loop with a radius of 20 cm. The initial energy is 200 eV, and the ion mass is that of argon. The plasma is initiated at an axial position of 5 cm with a different radial position for each trajectory shown. As Figure 4-1 shows, the trajectory of a particle on the plasma ring will fit into one of three categories depending on the initial radius of the ring.

First, for rings with a small initial radius relative to that of the current loop, the trajectories diverge from the field lines, and travel in straight trajectories in the downstream direction after some initial deflection of less than 90°. The origin of this collisionless detachment is shown in Appendix A to be electron inertia. The plasma in the first category contributes to thrust.

Second, plasma particles on rings initiated farther from the axis are deflected more than 90° before they escape from the field. They ultimately travel in straight trajectories in the upstream direction and produce negative thrust.

Third, plasma rings initiated farthest from the axis are trapped by the field and eventually return to the initiation region. Plasma in this category not only produces zero thrust but would also contaminate a spacecraft. Although Figure 4-1 was calculated including diamagnetic acceleration, the following results indicate that the acceleration term has no effect on plasma trajectories.

A comparison of the two methods of calculating trajectories is shown in Figure 4-2. To compare the two methods accurately, the initial energy must be the same in both cases. When the dipole moment is included, the initial energy is the kinetic energy of an electron in a cyclotron orbit, but when the plasma is injected with an initial axial velocity, the initial energy is the kinetic energy of an ion. To make G applicable to calculations including the dipole moment, E_i in Equation 4.9 is the initial energy of an electron. As shown in Figure 4-2, the trajectories coincide for the two approaches.

Additionally, most of the diamagnetic acceleration takes place in a short distance.

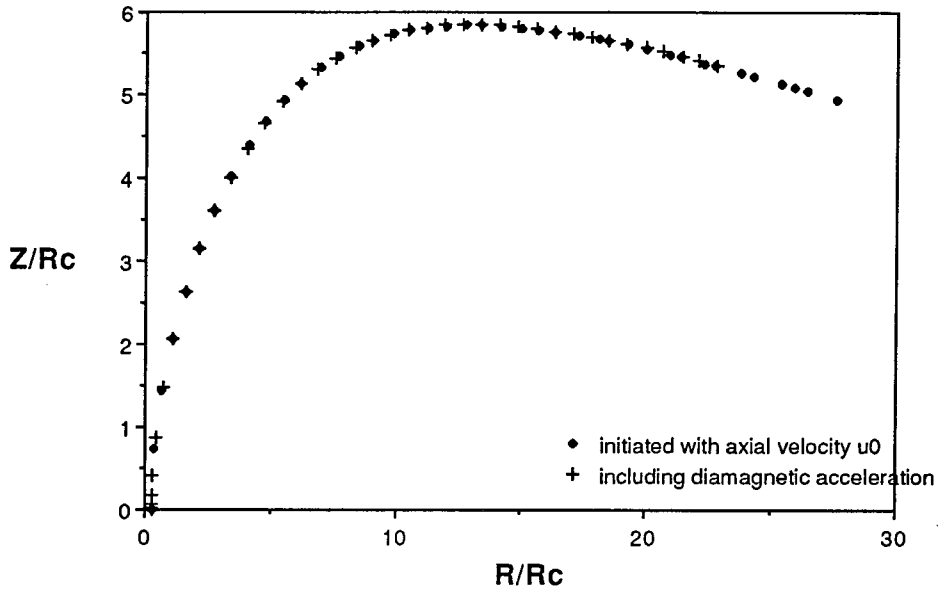

Figure 4-2: Comparison of the two methods of trajectory calculation.

This is shown in Figure 4-3 in which the velocity of the plasma following the innermost trajectory in Figure 4-1 is plotted. As shown in Figure 4-3, more than 90% of the energy initially in the electrons' cyclotron motion is transferred to the ions in two coil radii. Therefore, both the position and velocity are the same for the two approaches once the plasma travels a short distance downstream. In view of these results, neglecting the diamagnetic acceleration appears to be a good approximation for studies of plasma divergence in an ECR thruster.

Since we can ignore diamagnetic acceleration, the only variables that can determine plasma trajectories are G and the geometry of the nozzle. First, we will examine how G affects plasma trajectories. Plasma trajectories for several values of G are presented in Figure 4-4 normalized to the radius of the magnet coil, r_c. In each trajectory the plasma ring has an initial radius of 0.67 coil radii. We see in Figure 4-4 that, as expected, the larger the value of G, the more the magnetic field deflects the plasma until the trajectory and the corresponding field line coincide at about G =3000.

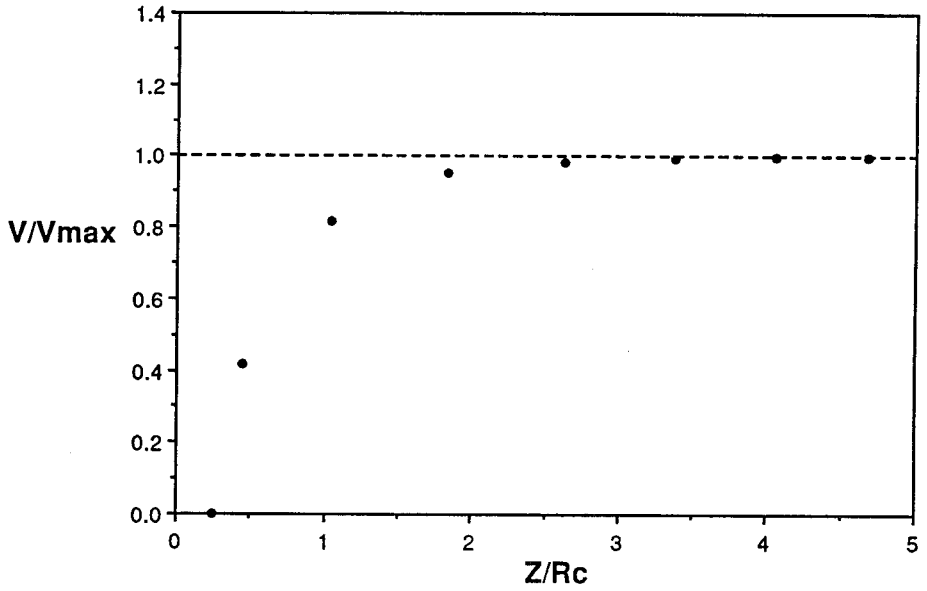

Figure 4-3: Normalized plasma velocity as the plasma travels downstream.

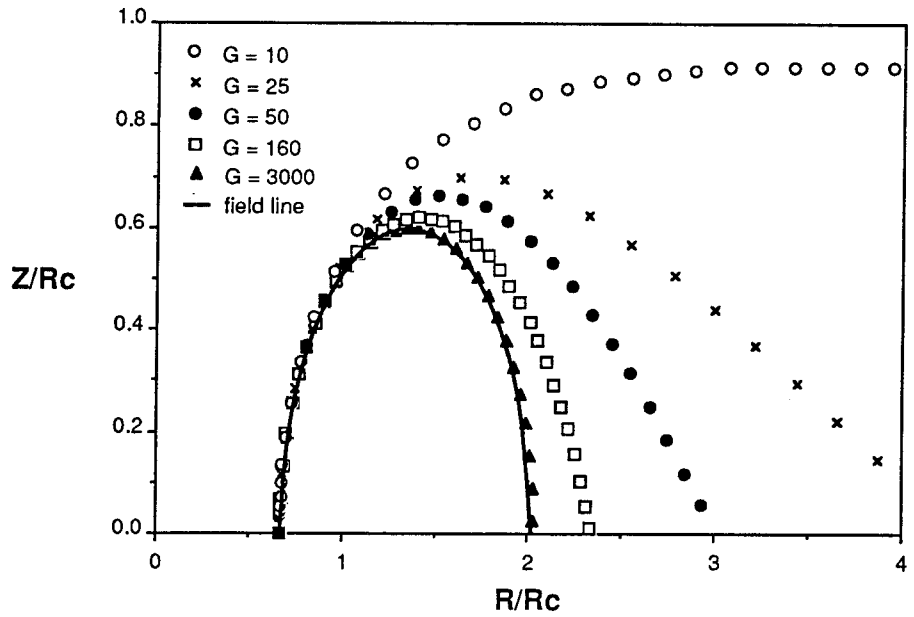

Figure 4-4: Trajectories at a fixed initial radius.

When G is approximately 10 in Figure 4-4, the magnetic field deflects the plasma by 90°. We will call this critical value G_{90}. Plasma generated with G less than G_{90} will have a trajectory in the first category discussed above. The plasma will detach from the nozzle and produce positive thrust. Plasma with G greater than G_{90} will have a trajectory in the second or third categories and will either detach but produce negative thrust or be trapped by the field and collide with the spacecraft. Therefore, G_{90} represents the boundary between plasma rings with trajectories which are beneficial and detrimental to thrust.

Values of G_{90} are shown in Figure 4-5 for a single current loop nozzle with the plasma initiated in the plane of the magnet. The results are graphed as a function of the initial plasma radius normalized to the magnet coil radius, (r_0/r_c). When the initial radius of the plasma ring is large, G_{90} is small, indicating that the plasma ring must have high kinetic energy compared to the magnetic flux energy for separation to occur. When the radius of the plasma ring is small, G_{90} is large, and detachment can occur even when the ion energy is small compared to the magnetic flux energy.

The value of G_{90} is a function of the initial radius and axial position of the plasma ring, (r_0, z_0), and the shape of the nozzle. We can see how the trajectories also depend on the initial plasma position in Figure 4-6. For the same value of G, the trajectories of plasma initiated farther from the axis diverge more than the trajectories of plasma initiated closer to the axis.

As we saw before, if the plasma separates from the field lines, it reaches a final velocity with some fixed angle of divergence from the thruster axis. The variation in the divergence angle with initial radial position is shown in Figure 4-7 where the cosine of the divergence angle is plotted as a function of the normalized injection radius. Maximum area under the curve is desired for maximum thrust. As expected, with higher energy ions, the curve for 200 eV has a larger area than for 2 eV. The curve enclosing the greatest area was also calculated with an initial ion energy of 200 eV, but the initial axial position of the plasma was moved one magnet coil radius

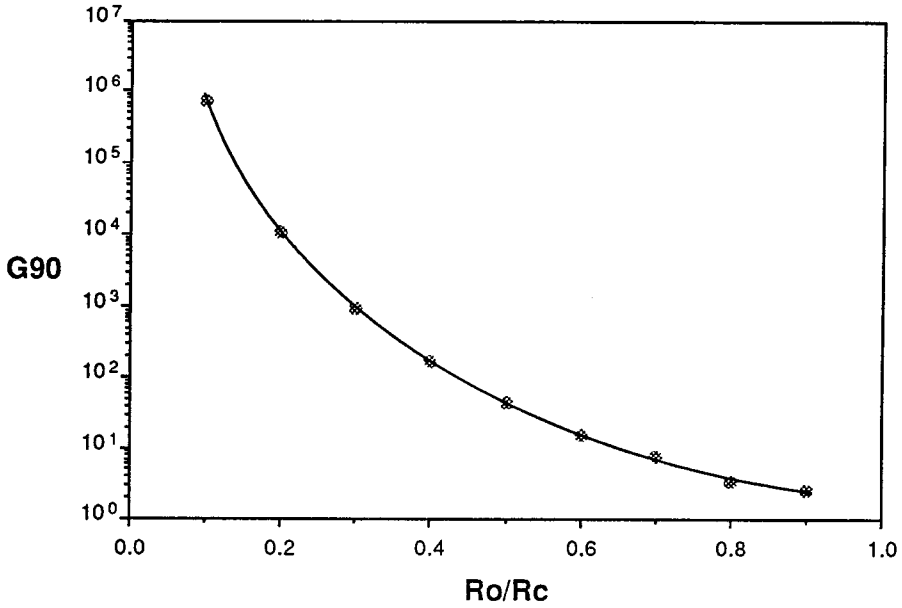

Figure 4-5: G for 90° divergence.

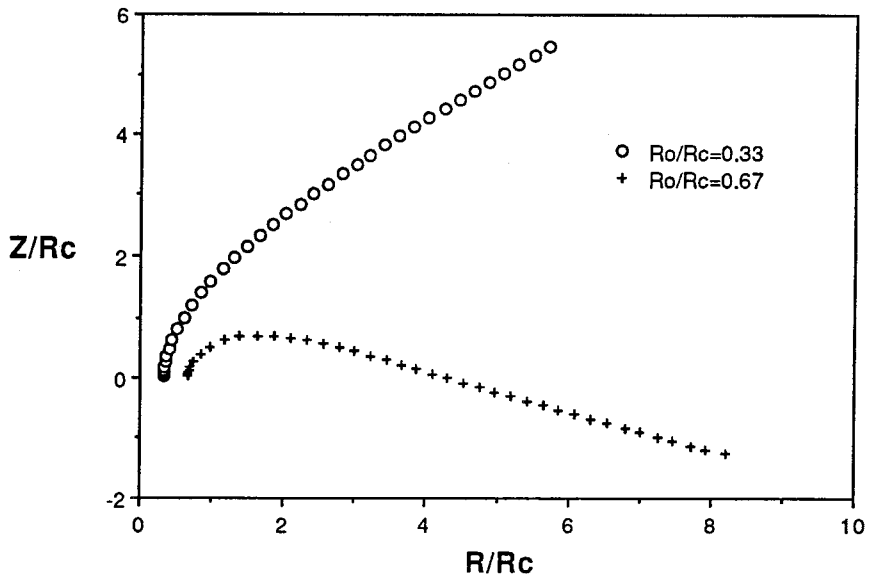

Figure 4-6: Trajectories for $G = 25$ at different initial radii.

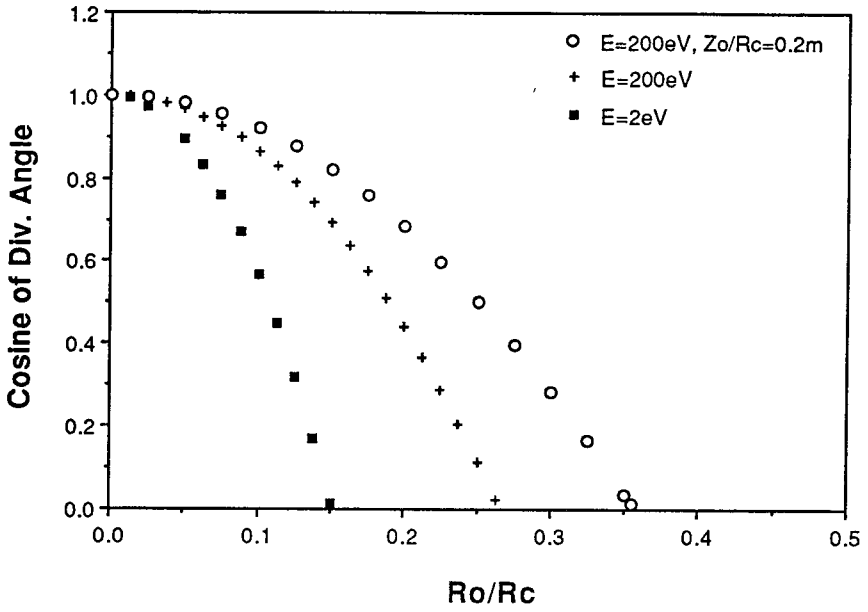

Figure 4-7: Cosine of the divergence angle.

downstream from the magnet. The magnetic field was also adjusted so that G was the same for both cases at 200 eV.

The increase in area under the highest curve is due to the straightening of the field lines downstream from the magnet. Consider the magnetic field at a distance z_0 downstream from the current loop. For every radius r the field lines passing through (r, z_0) have a larger radius of curvature than the field lines passing through $(r, 0)$. When the plasma is created farther downstream, the field lines associated with the each ring of plasma at its origin are straighter. Another benefit of moving the generation region downstream is that the mirror ratio between the solenoid and generation region is larger, resulting in a reduced upstream plasma loss cone.

Extending the idea of moving the plasma injection region downstream from the magnet, let us examine how the area of useful thrust varies with z. The radius at which the plasma is deflected by 90° (denoted R_{90}) is the border of the region useful for plasma generation, so R_{90} is the maximum possible radius for a thruster with

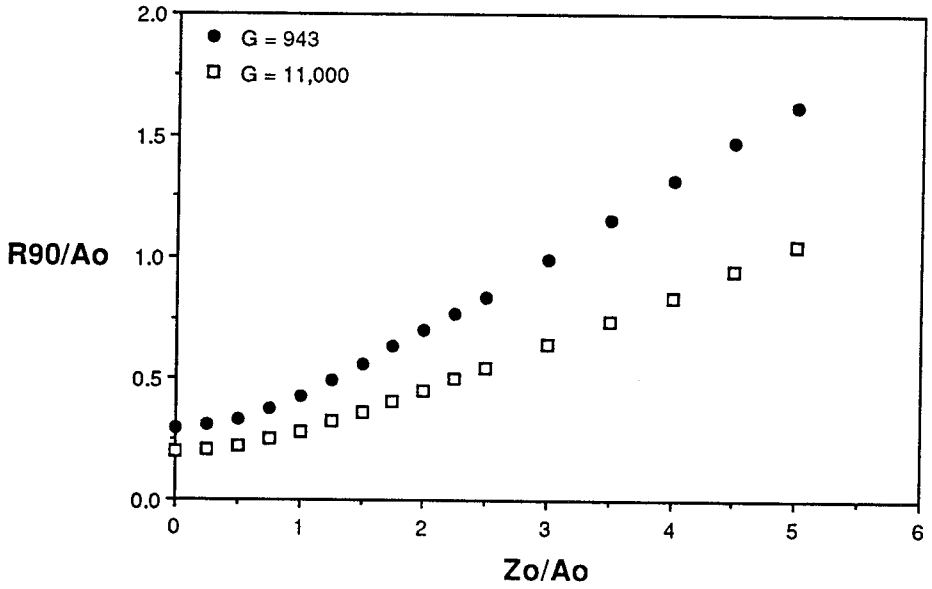

Figure 4-8: Radius of 90° divergence with varying initial axial position of the plasma ring.

the same conditions. In Figure 4-8, R_{90} is plotted for two values of G as the initial plasma position is moved downstream from the plane of the solenoid. The value of R_{90} increases roughly linearly, becoming unity at approximately 3 and 5 coil radii downstream for $G = 943$ and $G = 11,000$ respectively. The straightening of the field lines at greater axial positions allows plasma rings with greater initial radii to detach from the field and contribute to thrust. The cost of the increased thruster size is the extra current needed for the magnet. To maintain the same magnetic field strength in the plasma generation region, the magnet current must increase 2.83 times when the plasma initial position is moved from the plane of the magnet to 1 coil radius downstream and by another 3.95 times to increase the axial position from 1 to 2 coil radii.

Another possible means to position the ECR region in a region of straighter field lines is to add a secondary magnet coil of larger radius downstream from the main coil. The smaller main coil dominates the field near the origin of the plasma, providing the

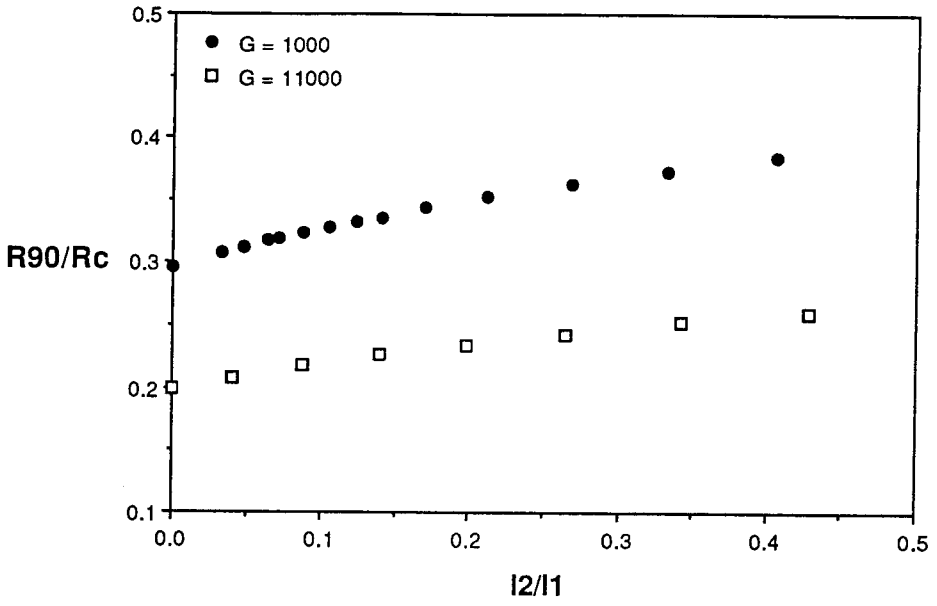

Figure 4-9: Radius of 90° divergence vs. ratio of coil currents.

ECR condition at the desired frequency. The secondary coil dominates the far-field, so in effect the plasma is generated at a decreased radius relative to the far field coil. In Figure 4-9, R_{90} is shown as a function of the ratio (main coil current/secondary coil current). The plasma was initiated in the plane of the main coil. All distances are normalized to the radius of the main coil. The secondary coil has 2 times the radius of the main coil and is 0.5 main coil radii downstream. As the figure shows, R_{90} increases as the ratio of currents increases. However, the increase is slight considering the extra weight that would be required for a second magnet. This scheme loses its utility when the current in the secondary coil becomes so large that the field in the plane of the secondary coil is equal to the field at the plasma origin. The plasma is then trapped in a magnetic bottle. While the improvement in performance due to adding a second coil is slight, a combination of multiple coils and initiating the plasma downstream may further enhance detachment over moving the plasma alone.

4.4 Conclusions

Collisionless detachment of plasma from a magnetic nozzle depends on several factors including the plasma energy, the magnetic field configuration, and the plasma initial position. Acceleration of the plasma due to the magnetic dipole force has a negligible impact on plasma trajectories, and most of the acceleration is complete after the ions have moved one magnet radius from their origin. The parameter G is a useful non-dimensional parameter which governs detachment behavior of the plasma. Plasma separation can be enhanced by manipulation of the nozzle configuration.

Chapter 5

Experimental Investigation of Plasma Detachment from a Magnetic Nozzle

5.1 Background and Purpose of Experiment

As we saw in Chapter 4, the plasma emitted from an ECR thruster or any other applied-field thruster must detach efficiently from the magnetic nozzle; otherwise it will follow the field back to the spacecraft and decrease the thrust. The conclusions of Chapter 4 and elsewhere [24, 31, 18, 37] suggest that divergence of the plasma plume caused by the magnetic nozzle may severely limit the performance of an ECR thruster. However, since the model used to calculate plasma trajectories assumed a collisionless, cold plasma, the effects of electrical resistivity, fluid friction, and plasma instabilities were not considered. These excluded effects may cause a real plasma to deviate significantly from the predictions of the collisionless model. Experimental confirmation is needed to determine the extent to which resistivity enhances detachment, friction hinders detachment, and to validate the collisionless model.

Due to the size of the vacuum tank, observation of plasma detachment would be quite difficult using the experimental apparatus from the ECR experiments described in previous chapters. The collisionless analysis of Chapter 4 predicts that very little separation between the plasma and the field lines will occur in the 3 m $\times$ 1.5 m dia. vacuum tank under the conditions attainable with the ECR thruster and magnet.

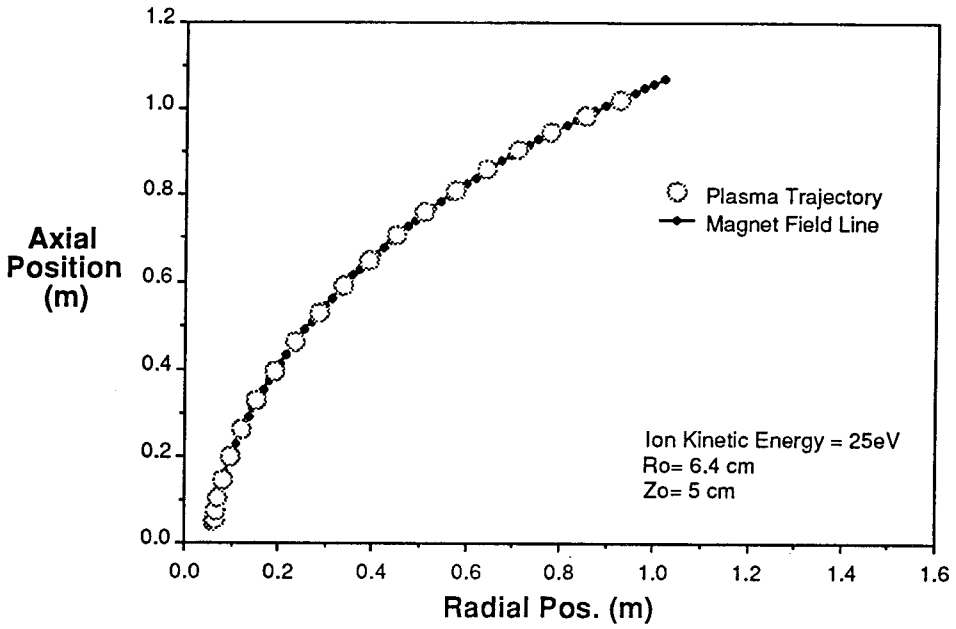

Figure 5-1: Calculated trajectory of outermost edge of laboratory ECR thruster.

Most of the detachment is expected to occur several meters from the thruster. As Figure 5-1 shows, the trajectory of the plasma at the edge of the ECR thruster would likely be indistinguishable from the magnetic field line. Visual observation of the laboratory plasma plume leads to the same conclusion. A sharp, curved boundary is seen at the edge of the plume approximately following the magnetic field line. Detachment could only be measured if collisional effects account for significant detachment near the thruster, and limited comparison to the model would be possible.

The ECR thruster also does not have the flexibility needed to provide a good means to explore detachment experimentally with the vacuum facility available. Recalling Equation 4.6

$$G \approx \frac{e^2}{2m_e}(B_{z_0}^2 r_0^2)\left(\frac{1}{\frac{1}{2}M_i u_0^2}\right),$$

we see that for a fixed initial radius of a plasma ring, to vary G over a range of values we would need to be able to change the plasma velocity, u_0, independent of the magnetic field, B, or fix the plasma velocity and change the magnetic field

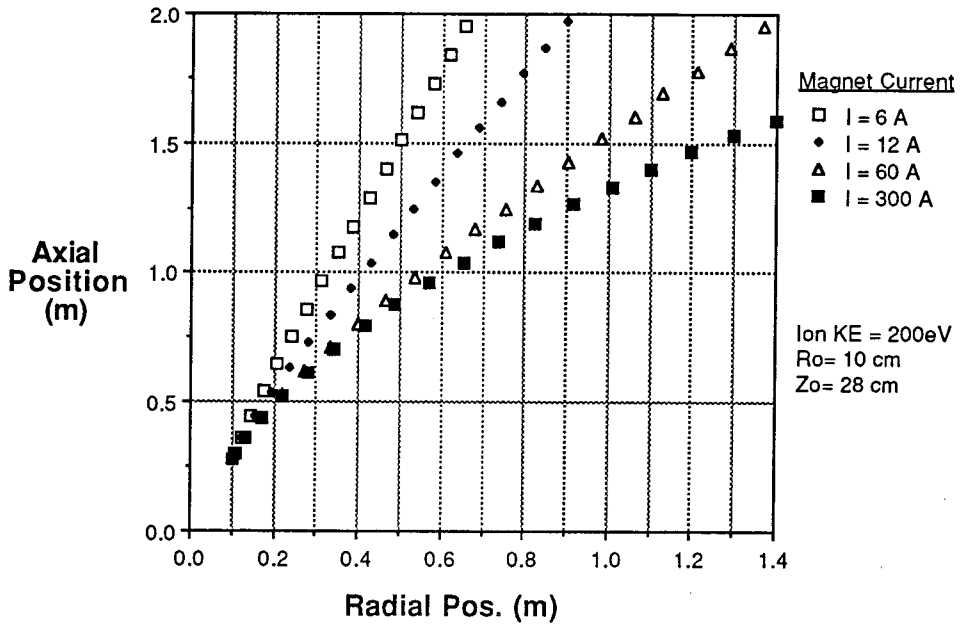

Figure 5-2: Calculated trajectories of plasma rings with initial position (r_0, z_0) as the magnet current is varied.

strength. Because the formation of the plasma in the ECR thruster is dependent on maintaining resonance between the fixed microwave frequency and the electron cyclotron frequency in the energizing zone, it is impractical to propose changing the magnetic field strength. In addition, as we saw in Section 3.2, the ion energy is nearly invariant with respect to flow rate and input power, so altering the plasma velocity is also not feasible, especially over a wide range of values necessary to fully investigate the effect of the G parameter.

A device such as an electrostatic ion engine would be a better choice for studies of plasma detachment because it produces a plasma of known and variable kinetic energy independent of any applied magnetic field. If we placed the ion thruster in an applied magnetic nozzle, the strength of the magnet could then be varied to explore a large range of values for G. For studies of detachment a useful experiment would be to extract an annular plasma from an ion engine and measure its trajectory in different magnetic fields and at different ion energies.

To further evaluate this idea, we use the model from Chapter 4 to calculate the trajectories of several plasma rings in a magnetic nozzle with properties attainable in the laboratory with the current magnet and an ion engine. To observe detachment we need to be able to observe maximum deflection in order to obtain the greatest contrast between the cases with and without the applied magnetic field. From the collisionless model, we know that for maximum deflection of the plasma from the magnetic field, the ions must have low kinetic energy while the magnetic field is as strong as possible. A typical ion engine can emit a beam of ions with measurable current density at a minimum kinetic energy of approximately 200 eV. Assuming such an ion thruster in the magnetic field of a solenoid similar to that found in the laboratory, we calculate the trajectories shown in Figure 5-2. As the magnetic field is increased, the plasma is deflected to a greater divergence angle. As the figure shows, at approximately 1 m, the maximum axial position reachable by the diagnostic arm, the difference between the radius of the plasma for low magnet current and for high magnet current is expected to be approximately 30 cm. If similar deflection is realized in the laboratory, the effect of the magnetic nozzle could be detected in maps of ion current similar to those in Section 3.1.

5.2 Experimental Apparatus

The existing magnet, vacuum equipment, and data acquisition system described in Chapter 2 was used in the experiments into detachment. In place of the ECR thruster an ion engine from the Advanced Propulsion Technologies Group at JPL was mounted in the vacuum tank as shown schematically in Figure 5-3. The face of the accel grid was 40 cm downstream from the center plane of the magnet, and the thruster was positioned coaxially with the magnet. A photograph of the ion engine in the tank is shown in Figure 5-4. The diagnostic arm used to map the plasma properties can also be seen in the foreground of the figure. The engine is mounted so that each

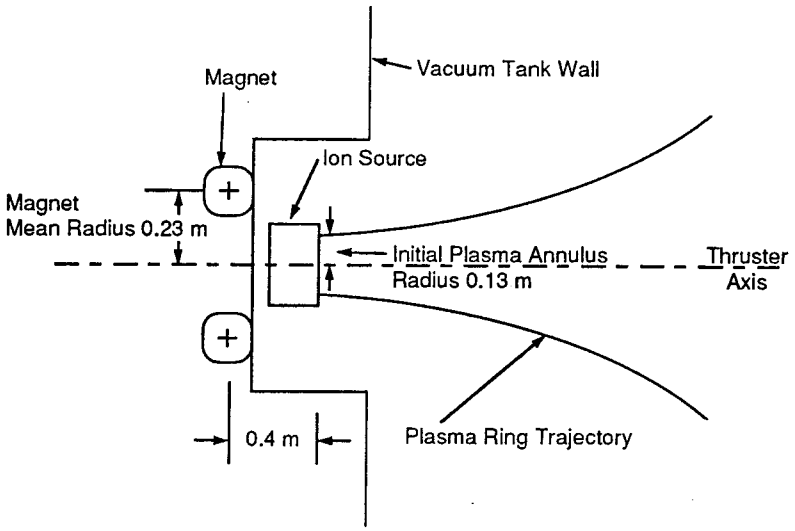

Figure 5-3: Schematic of experimental apparatus used in detachment studies.

diagnostic probe passes horizontally through the thruster axis as the arm moves across the plasma plume.

A schematic of the ion engine is shown in Figure 5-5. A hot filament cathode produces electrons inside the thruster. Permanent magnets establish a weak axial magnetic field to impede the electrons streaming to the anode. The electrons from the cathode collide with the neutral propellant gas and ionize it. The ions then accelerate through a potential drop between the screen and accel grids. The resulting ion beam is neutralized by electrons for a hot filament neutralizer. [6]

The propellant for the experimental ion thruster was argon, and the flow was controlled by the same mass flow controllers used in the previous experiments. Several power supplies were used to control the potentials on the ion engine as shown in Figure 5-5. Some typical voltages are shown on the power supplies in the figure in addition to the resulting potentials on several engine components. The voltages and currents across the power supplies were measured by the backplane and recorded

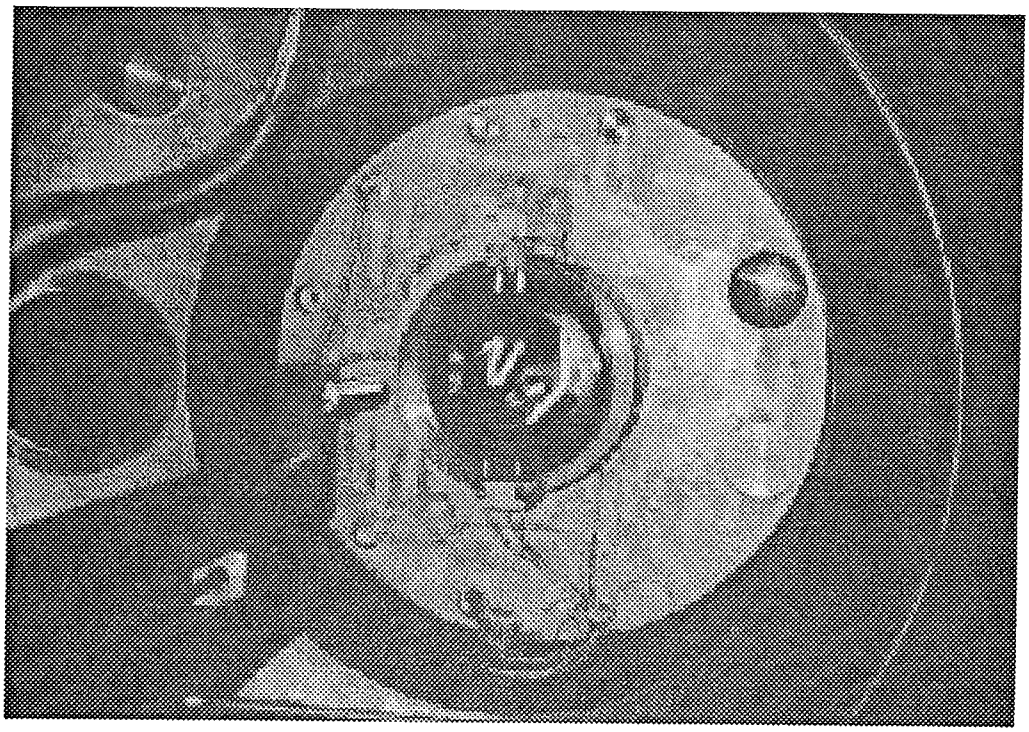

Figure 5-4: Photograph of masked ion engine mounted in vacuum tank.

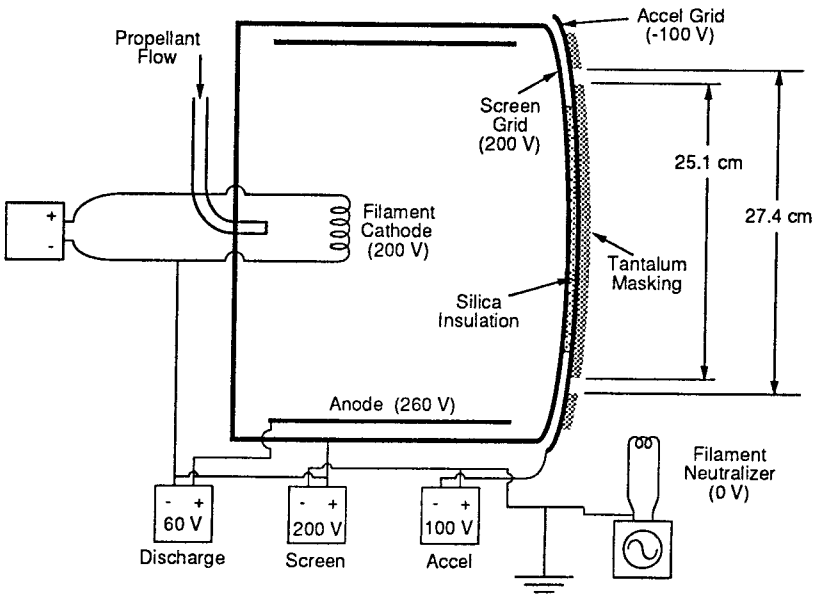

Figure 5-5: Schematic of ion thruster used in detachment experiment.

along with the data from the diagnostics.

For the detachment experiments the extraction grids were masked with tantalum foil spot-welded to both the screen and accel grids so that the open grid area was a ring of mean radius 13 cm and width 1.3 cm. A diagram of the masked grids is shown in Figure 5-6. Four neutralizer filaments are placed directly in the plasma beam. The plasma environment degrades the filaments rapidly, so redundancy is needed to make longer experiments possible. The neutralizers are placed at the top and bottom of the thruster to be out of the path of the probes and to maintain symmetry. As shown in Figure 5-6, the filament cathode is coiled in a circle with diameter approximately 10 cm. Initial attempts were made to operate the thruster in the presence of the magnetic nozzle with a small single filament similar to the neutralizers. These initial trials failed because instead of moving to the anode and ionizing the propellant, the electrons from the cathode were guided directly to the center of the screen grid by the axial magnetic field. The tantalum masking melted through at the point of intersection with the electron beam. The cathode was subsequently lengthened and oriented in a circle to increase the number of electrons available to ionize the propellant and to spread out the electrons streaming to the screen when the nozzle was in operation. Silica insulation was added between the screen and accel grids as shown in the figure to prevent electrical connection due to grid heat expansion or melting.

In addition to guiding the cathode electrons to the screen, the solenoid magnet changes the performance of the ion source. As described above, the increased axial magnetic field inside the engine hinders the electrons traveling from the cathode to the anode. As a consequence, the anode current decreases with increasing magnetic field strength and fewer ions are created. Therefore, the beam current decreases as the magnetic field strength increases. A consistent beam current is needed to compare results of experiments, so the beam current is held constant by increasing the anode voltage. Below, the beam current is constant whenever comparisons are

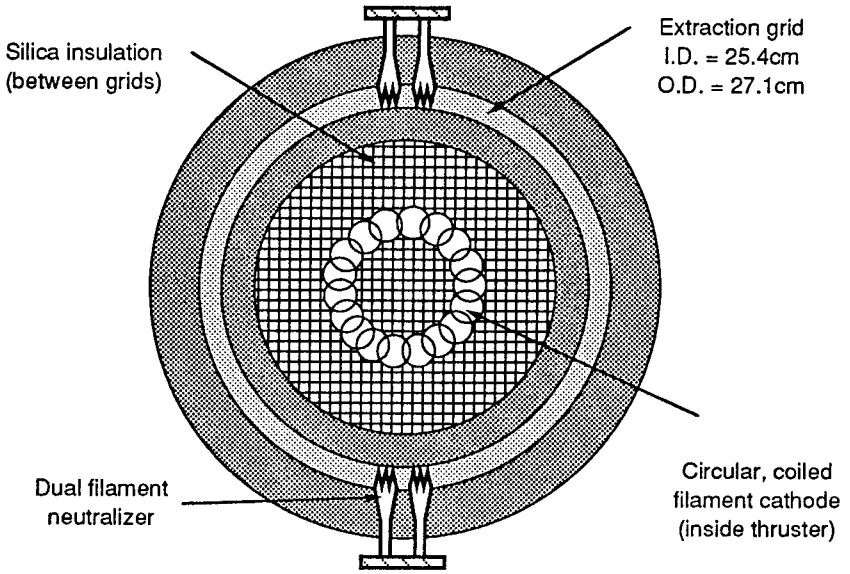

Figure 5-6: Schematic of masked grids, neutralizers, and coiled filament cathode.

made among experiments conducted in different magnetic fields although the anode voltage increases with the field strength.

5.3 Ion Flux Profiles

The ion current was measured for various operating conditions using the Faraday cup as discussed in Section 3.1. A map of the ion current density for the masked ion source is shown in Figure 5-7. The engine would be located at the top of the page with the annular plasma beam extending toward the bottom of the page. The operating conditions are as noted below the figure, and there was no magnetic nozzle applied. As shown in the figure, the plasma annulus increases in diameter slightly as it expands away from the thruster. The thickness of the annulus also increases slightly as the plasma moves axially. Even with this expansion, a clearly defined beam can be seen in the figure at a distance of 60 cm from the face of the ion source (axial position -100 in Figure 5-7).

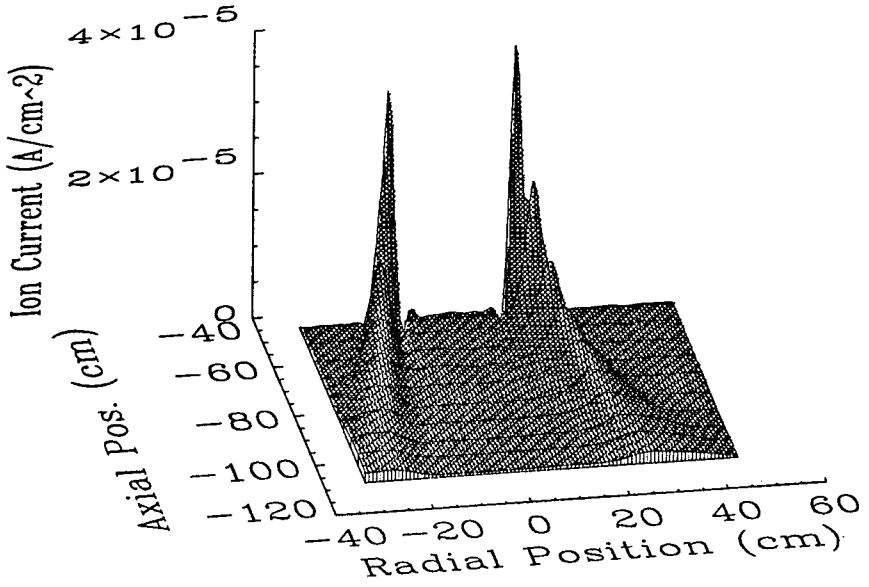

Figure 5-7: 3-D plot of ion flux density for 4 sccm, 200 eV ions, no applied magnet current.

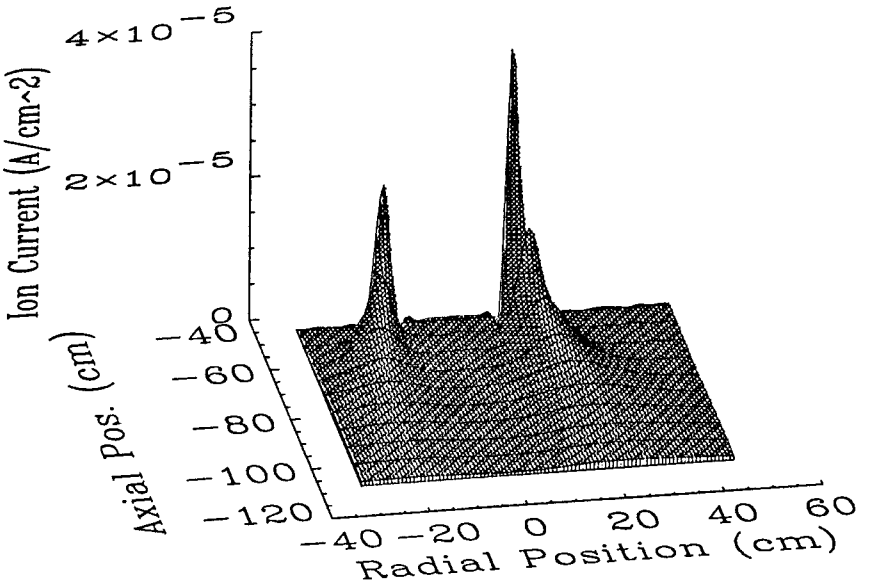

Figure 5-8: 3-D plot of ion flux density for 4 sccm, 200 eV ions, 100 A magnet current.

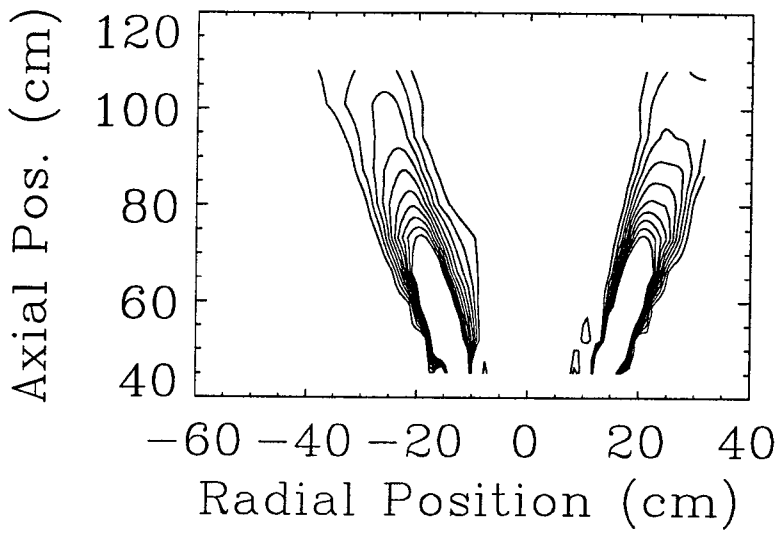

Figure 5-9: Contour plot of ion flux density for 4 sccm, 200 eV ions, no applied magnet.

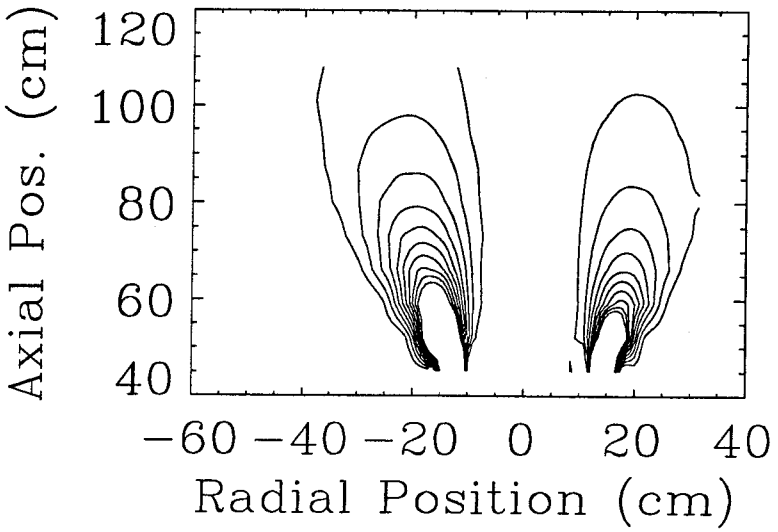

Figure 5-10: Contour plot of ion flux density for 4 sccm, 200 eV ions, 100 A magnet current.

In Figure 5-8 the operating conditions are the same as in Figure 5-7, but a magnetic nozzle is applied with 100 A of current in the magnet, resulting in a field strength of approximately 30 gauss on axis at the ion source face. Again the annular ion beam increases in radius and the thickness of the ring increases with axial distance downstream. However, in contrast to the case with no applied magnetic nozzle, the beam becomes diffuse at large distances from the thruster. At 60 cm from the ion source face, the thickness of the rings is so great that the ion flux density is distributed nearly evenly across the entire plume. The annulus has also become asymmetric with more plasma flow on the right side in Figure 5-8 than on the left. It is believed that the effect of the applied magnetic field on the cathode electrons inside the ion thruster causes an asymmetric plasma annulus to be emitted through the masked grids. As the magnetic field strength is increased, the asymmetry is intensified. Several unsuccessful attempts were made to correct the asymmetry by manipulating the cathode and adjusting the beam current and anode voltage.

This accelerated thickening of the plasma annulus with the applied magnetic field can be seen more clearly in the contour plots in Figures 5-9 and 5-10. Without the magnet the plasma remains in a thin annular beam which increases in radius slightly as it moves into the vacuum tank as seen in Figure 5-9. When the magnetic nozzle is applied, the rings become noticeably thicker in only a short distance downstream from the thruster as shown in Figure 5-10.

In addition to altering the thickness of the plasma annulus, the magnetic field affects the plasma trajectory. The effect of the magnetic nozzle on the trajectory of the plasma beam can be seen in Figure 5-11 which is a plot of the ion current density at a fixed axial position. The peaks in the two curves represent the radial position of the annular plasma beam at 66 cm from the face of the ion source. The increased width of the peaks in the curve with the magnetic nozzle shows the same spreading of the beam observed in the figures above. However, the relative positions of the peaks are contrary to what we predicted using the collisionless model. The plasma annulus

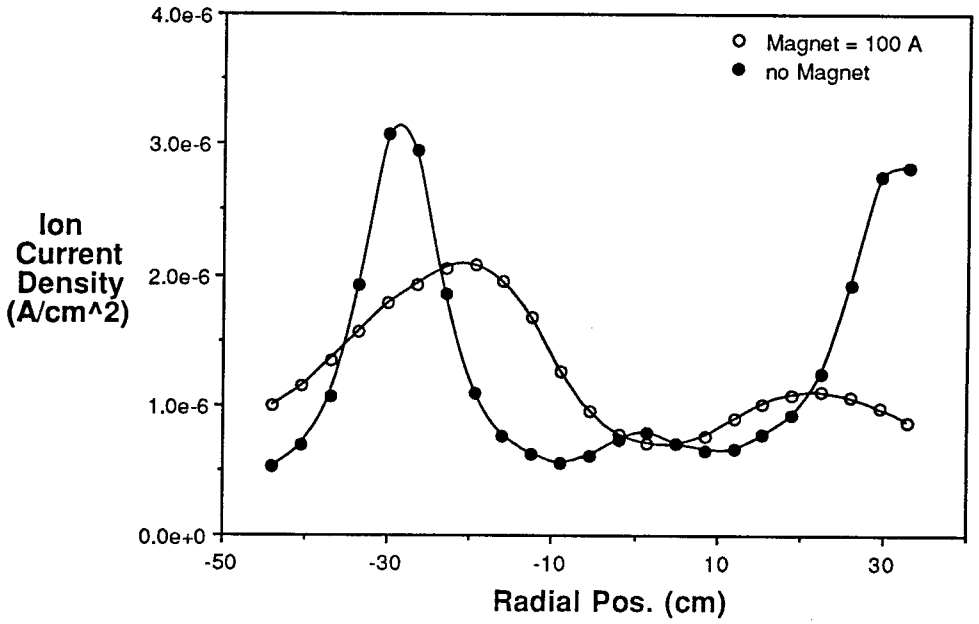

Figure 5-11: Effect of applied magnet on radius of plasma annulus at 66 cm from the ion source face.

has a greater radius without the magnetic nozzle than with it. Instead of deflecting the ion beam away from the thruster axis as we expected, the magnetic field causes the beam to converge toward the axis.

The vacuum tank pressure also affects the ion flux density profile. In Figure 5-12 the ion flux density profile is shown for the same thruster conditions as Figures 5-10 and 5-9, but the propellant flow rate was increased from 4 sccm to 12 sccm. The increase in flow rate resulted in a tank pressure increase from 3.4×10^{-5} torr to $10. \times 10^{-5}$ torr. Comparing Figure 5-12 to Figure 5-10 we see that although the magnetic field strength is the same for both cases, the plasma annulus is thicker with the lower flow rate. However, the beam in Figure 5-12 is not as well defined as in Figure 5-9. For the case with the higher flow rate, the magnetic field still causes the ion beam to spread out, but it seems that the additional pressure causes the beam to remain more collimated even with the magnetic field in operation.

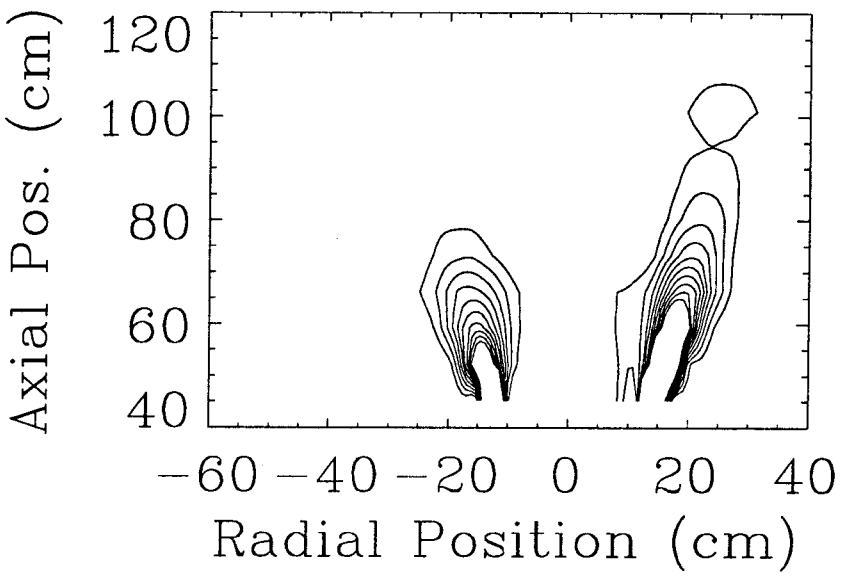

Figure 5-12: Effect of increased propellant flow and tank pressure on ion flux density. Conditions: 12 sccm, 200 eV ions, 100 A magnet current.

5.4 Plasma Potential Measurements

To attempt to determine the cause of the spreading of the plasma annulus seen in the ion flux profiles, the emissive probe described in Section 2.3 was used to map the plasma potential in the plume of the ion engine. In Figure 5-13 the plasma potential profile is shown with no magnetic nozzle applied to the ion thruster. The plasma potential is highest near thruster in the upper part of the figure and falls slowly in the axial direction as the plasma moves away from its source. There is very little radial variation in the plasma potential inside the region bounded by the plasma annulus. The potential drops fairly sharply to a nearly constant value outside the edges of the plasma annulus. The area enclosed by the plasma annulus can be seen as the region of higher plasma potential against the constant potential of the background.

The magnetic nozzle was applied to the ion thruster with 100 A passing through the solenoid, and the map of the plasma potential was repeated in Figure 5-14. The profile is very different from the case with no applied magnetic field. The figure shows two peaks corresponding to the locations where the circular ion beam exits the thruster. The maximum potential is approximately 5 V greater with the magnet than without it, and axial rate of decrease is greater when the magnet is applied. In the radial direction the plasma potential is highest at the annulus, and falls as we move away from the ring of plasma. The plasma potential map appears much like the maps of ion current density shown in the section above, representing a ring of high plasma potential with lower potential outside the ring. As the ion beam moves axially away from the thruster, the plasma potential becomes more uniform in the radial direction. The peaks in the profile disappear at approximately 50 cm from the ion source face (axial position -90 in Figure 5-14).

The potential gradients seen in Figure 5-14 represent electric fields in the plasma beam caused by the applied magnetic field. The field is strongest at the inner and outer edges of the plasma ring where it emerges from the thruster. The axial component of the field will accelerate the ions slightly in the axial direction, but the radial

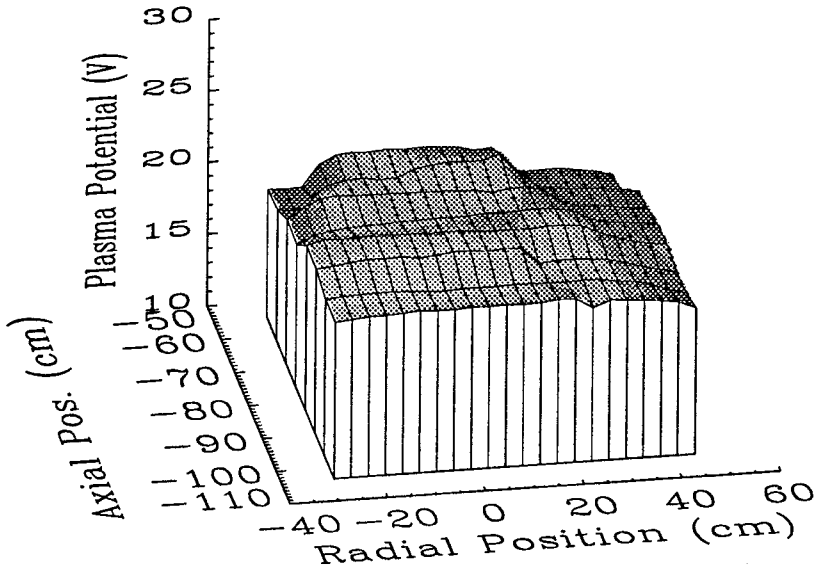

Figure 5-13: Plasma potential profile for 5 sccm, 200 eV ions, no applied magnet.

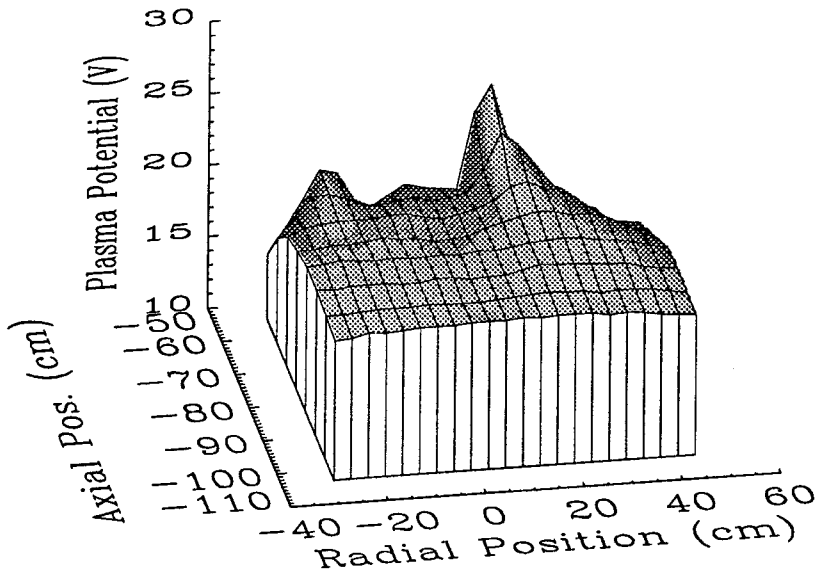

Figure 5-14: Plasma potential profile for 5 sccm, 200 eV ions, 100 A applied magnet current.

component of the field will change the ions' trajectories after they leave the thruster. The changing of trajectories is of more concern for an investigation into the effect of a magnetic nozzle on plasma beam trajectories.

Shown in Figure 5-15 is the formation of the radial electric field as the strength of the applied field increases. The figure shows the radial variation in the plasma potential across the plume at a fixed axial position of 14.3 cm from the ion source face. The curves are normalized to the common point for clarity. With no applied magnetic field we again see a flat profile in the top curve extending across the beam and falling off outside the area enclosed by the plasma annulus. As we observed in the figures above, peaks in the potential on the plasma ring form as the magnetic field increases in strength. The magnitude of the potential peaks increases as the strength of the magnetic nozzle increases. Similarly to what occurred with the ion flux profile, the magnetic field causes the potential profile to become asymmetric with the right peak in Figure 5-15 higher than the peak on the left. This asymmetry is also evident in Figures 5-14 and 5-14. Again, the asymmetry is believed to be due to the effect of the applied magnetic field on the plasma inside the ion thruster.

As with the ion flux measurements in the section above, the pressure in the vacuum tank affects the plasma potential profile. In Figure 5-16 a map of the plasma potential is shown for the same thruster conditions as in Figures 5-13 and 5-14, and the magnet current is 100 A as in Figure 5-14. However, the propellant flow in Figure 5-16 was increased from 4 sccm to 12 sccm with a corresponding increase in pressure from 3.5×10^{-5} torr to 10.8×10^{-5} torr. The profile in Figure 5-16 shows smaller peaks in the plasma potential than in Figure 5-14 although the magnetic field strength is the same. Also, the peaks in Figure 5-16 disappear in a shorter axial distance than the peaks in Figure 5-14. Comparing Figures 5-13, 5-14, and 5-16, the additional pressure seems to have reduced the effect of the magnetic field on the plasma potential.

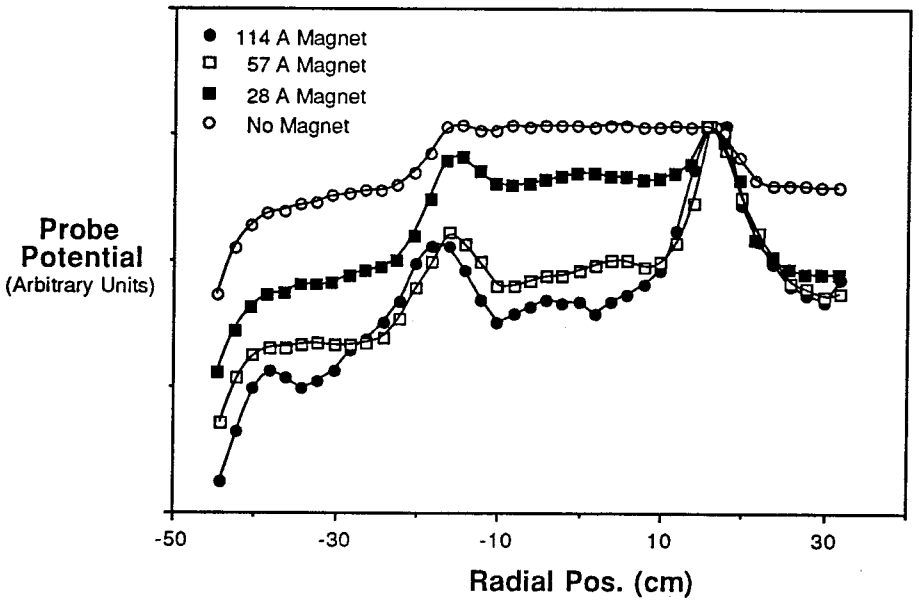

Figure 5-15: Formation of radial potential gradient at 58 cm from the magnet centerplane as applied magnet current is increased.

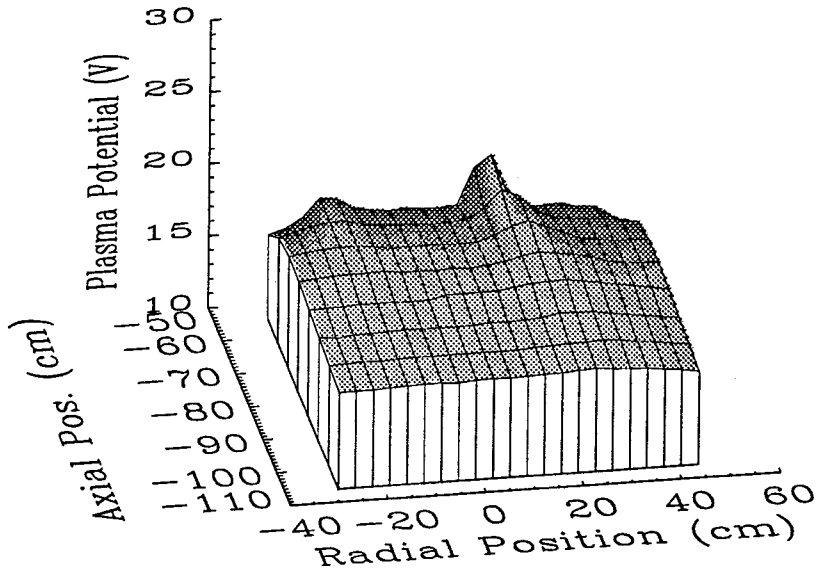

Figure 5-16: Effect of increased propellant flow and tank pressure on plasma potential. Conditions: 12 sccm, 200 eV ions, 100 A magnet current.

5.5 Ion Energy Measurements

The retarding-grid ion energy analyzer was used to measure the ion energy in the plasma plume. In addition to providing insight about the character of the ion beam for these detachment studies, the measurements presented here provide calibration for the ion energy analyzer. Because the kinetic energy of the ions is the same as the potential drop between the screen and neutralizer, the measured ion energy should be the same as the screen potential. Measurements at ion energy levels from 200V to 1000 V indicate that the results of the ion energy analyzer data are accurate to approximately 5% of the full screen potential. Because of the nature of the ion engine, the ion energy distribution function for its plasma beam is very narrow, so ion energy measurements are quite accurate. Measurements of the ion energy in the ECR experiments are inherently less accurate due to the relatively large width of the peak in the ion kinetic energy distribution function. The ion energy data presented in Section 3.2 should be considered measurements of the average energy of the ions in the ECR device while the data presented below can be regarded as representative of the energy of entire ion beam.

A spatial map of the ion energy for the masked ion thruster in the absence of a magnetic field is shown in Figure 5-17. The energy of the annular beam of ions is nearly constant in the axial direction indicating that little energy is lost to the background neutral gas. Compare this to Figure 3-10 for the ECR thruster at the same flow rate. The ions in the ECR plasma, with initial energy of approximately 10% of the ions in Figure 5-17, lose a much larger fraction of their energy to collisions as they travel through the background neutral gas. Examining the radial variation in Figure 5-17 we see that the ion energy decreases away from the annular ring of the plasma. Extremely low ion current along the thruster axis made measurements of ion energy unobtainable, so the energy in this region was set to zero in the figure. On the left side of the figure, the region of high ion energy is wider than on the right, probably due to slight deflection of the ions at the edges of the masking. Enough ions

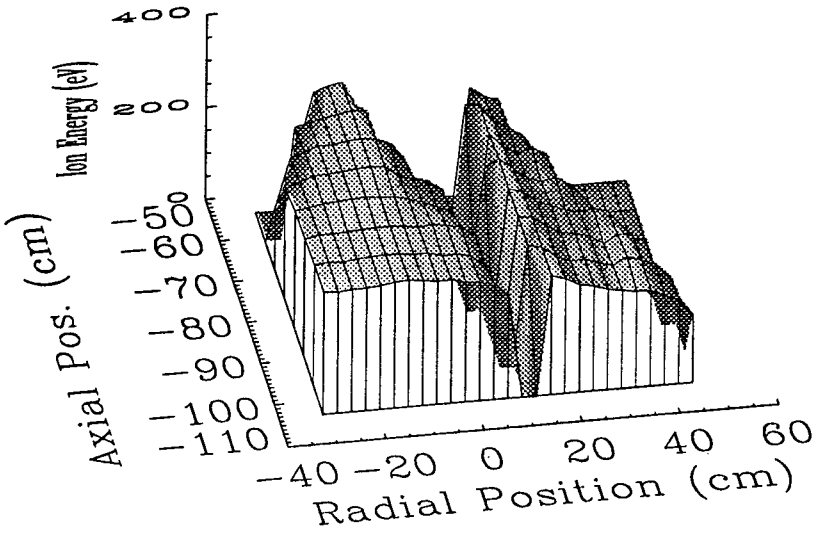

Figure 5-17: Ion energy map 6 sccm, 250 eV ions, no applied magnet.

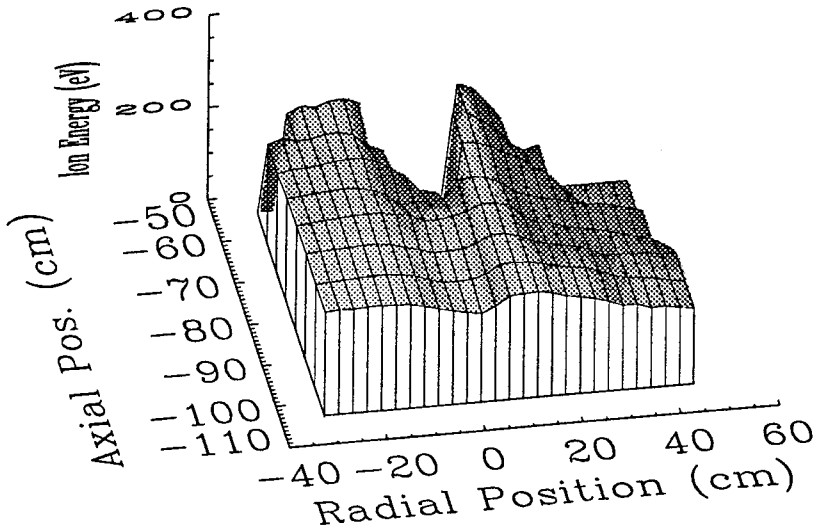

Figure 5-18: Ion energy map 6 sccm, 250 eV ions, 80 A magnet current.

are directed outside the annular beam to make ion energy measurements possible away from the main ring. Only a small fraction of the ions are deflected in this way as demonstrated by the ion flux maps which show a highly defined ion beam when there is no applied magnetic field.

In Figure 5-18 the ion energy profile is shown for the same thruster conditions as in Figure 5-17, but the magnetic nozzle is activated with 80 A of current applied to the magnet. The profile is quite similar to that in Figure 5-17, but there is only a small region near the center of the thruster where the ion energy is unobtainable. The thickening of the plasma annulus in the presence of the magnetic field that we saw in Section 5.3 causes enough ions to populate the area inside the plasma annulus to make ion energy measurements possible. As with the field-free case, the ion energy is fairly constant over the entire plume of the thruster with a slight drop off outside the area enclosed by the plasma annulus. The notable difference, however, is in the region along the thruster axis in which the ion energies are now measurable. The ion energy is lower on the axis than in the ion beam. With the magnetic nozzle turned on, lower energy ions seem to be selectively drawn toward the center of the plasma annulus.

5.6 Conclusions

The experiment did not satisfy its primary goal of providing insight into plasma detachment from a magnetic nozzle. However, the physics that contributed to its failure is quite interesting. It is believed that the radial electric field, seen in the plasma potential data presented above, appeared because the applied magnetic field inhibited neutralization of the ion beam. The electric field then deflected the ions extracted from the ion thruster causing the plasma trajectories to deviate from the model's predictions.

When the magnetic field is absent, there is nothing to prevent the electrons from

the neutralizer from traveling to neutralize the ion beam. With the field activated, the radial motion of the electrons is restricted by the field, and the electrons are apparently unable to neutralize the beam. As a result a potential gradient forms due to the inadequately neutralized beam. Instead of a neutral beam of ions and electrons traveling under the influence of the magnetic field, the partially-neutralized ion beam travels under the influence of the electric field.

The spreading of the ion beam seen in Figures 5-8, 5-10, and 5-11 is explained by the potential profiles in Figure 5-14 and 5-15. The unmagnetized ions are deflected away from their original trajectory as they fall through the potential gradient in the radial direction, and the well-defined annular flow widens into a diffuse plume. Because the magnetic field prevents electrons from moving to the ions, the ions move to the regions of lower potential. The lower energy ions are deflected through the greatest angle ($\tan\theta$ = radial potential drop/axial ion energy) resulting in the region of low energy ions along the thruster axis in Figure 5-18.

When the propellant flow rate is increased, the radial electric field strength decreases along with the thickness of the plasma annulus as shown above in Figures 5-16 and 5-12. It appears that with higher pressure in the vacuum tank radial mobility of the electrons increases due to collisions. With increased mobility, the electrons are better able to neutralize the ion beam.

In an attempt to remedy the neutralization deficiency, additional neutralizers were added (a maximum of four were used as shown in Figure 5-6) and were positioned directly in the plasma flow. However, minimal change was observed in the plasma potential and ion flux profiles with the added neutralizers. It may be that secondary electrons from the metal surfaces in the tank participate in neutralization of the thruster. Decreased radial electron diffusion would then prevent these secondary electrons from traveling to the ion beam. It may also be that due to severely reduced electron mobility within the beam itself, a sufficient number of electrons were unable to escape from the filament.

Chapter 6

Summary and Conclusions

6.1 Review of Results and Conclusions

As the cost of launching satellites into orbit has increased, electric propulsion (EP) has drawn considerable interest because electric rockets can accomplish some of the same missions as chemical rockets with less fuel. Many conventional electric propulsion devices have electrodes which erode in the presence of plasma and limit the life of the thrusters. An ECR thruster is one type of EP device which may be capable of longer missions because it is electrodeless. A circularly polarized microwave beam ionizes a propellant gas in an energizing region where the microwave frequency equals the electron cyclotron frequency in a coaxial magnetic nozzle. The electrons absorb energy from the microwave beam in their orbital motion around the magnetic field lines and accelerate due to the force of the diverging magnetic field on the dipole moment of the electrons. The unmagnetized ions accelerate with the electrons due to the ambipolar electric field.

However, even though there are advantages to using electrodeless plasma propulsion with ECR, several challenges must be overcome before ECR thrusters can be considered for propulsion applications. An efficient thruster must be developed with performance comparable to that of electrostatic ion engines. One serious problem for ECR and other applied-field thrusters is that the magnetic nozzle deflects the plasma

and decreases thrust.

To learn more about the ECR plasma and to evaluate the concept as a thruster, several plasma diagnostics were used to measure various plasma properties. The diagnostics were mounted on a movable arm which was used to make measurements at many points in the plasma plume. Profiles were obtained which show the spatial variation of the plasma characteristics.

A Faraday cup was used to measure the ion current density in the plasma plume. The ion flux profiles show that the plasma is annular at low pressures. As the vacuum tank pressure increases, the annular profile is converted to one that has maximum flux density on the thruster axis. The reason for the annular flux seems to be that radial diffusion is retarded at low pressures by the magnetic field. Electrons from the thruster walls are necessary to maintain the plasma at low pressures but are not able to diffuse to the thruster axis. The result is a ring of plasma at the ECR region which propagates as the plasma accelerates away from the thruster. As the pressure increases, radial diffusion increases due to more frequent collisions, and the plasma is able to form across the entire ECR region. Therefore, at higher pressures, the ion flux density is maximum at the thruster axis.

The ion flux density was integrated across the plume to obtain the total ion flux. As anticipated, the integrated ion flux increases with flow rate and input power. In come cases at high flow rates and power levels, the total flux of ions exceeded the total inflow of argon atoms indicating that background gas is ionized along with the propellant in the ECR region. Background gas may also be entrained and ionized downstream from the ECR region. For some cases the total ion flux actually increased as the probe moved away from the thruster.

A retarding energy analyzer was used to measure the axially directed kinetic energy of the ions. In the plasma the ions attained energies in the range of 25 eV. The ion KE was highest at the thruster axis and decreased in both the axial and radial directions apparently due to friction with the background neutrals. The ions'

energy was unaffected by the input microwave power, but as the pressure in the tank increased, the ion energy decreased. Collisions at higher pressures caused the ions to lose energy.

From the ion flux and energy measurements, the thrust, specific impulse, and propulsive efficiency were calculated for the laboratory thruster. The thrust was a few millineutons at an I_{sp} of approximately 1×10^4 m/s. The thrust and efficiency increased with tank pressure and input power. However, entrainment of the background gas artificially increased the thrust and efficiency by increasing the flux of ions. Compared to a small ion thruster, the performance of the laboratory ECR device was poor especially considering that the performance was enhanced by the additional ion flux. Further tests of the ECR concept in a vacuum facility with a greater pumping capacity are necessary to provide a better projection of thruster performance in a space environment. The propulsion parameters seem to be largely effected by the background pressure in the vacuum tank, and the results for a thruster in space would likely be quite different.

To further investigate the ECR plasma thruster, an emissive probe was used to measure the plasma potential over a range of thruster operating conditions. The magnitude of the measured plasma potentials was several tens of volts. In the spatial profiles the plasma potential decreased monotonically in the axial direction but showed little radial variation. The axial decrease in plasma potential is not proportional to the magnetic field strength. It is suspected that collisions cause the plasma potential to deviate from proportionality to the magnetic field. Increases in applied microwave power have a negligible effect on the plasma potential, but the plasma potential decreases throughout the plume as the pressure in the vacuum tank increases. More frequent collisions due to the added background gas at elevated pressures cause a reduction in the plasma potential and therefore reduce ion acceleration and thrust.

Two cylindrical Langmuir probes oriented perpendicular to each other were used to measure the parallel and perpendicular components of the electron temperature

(T_e) over a range of thruster operating conditions. The electron temperature reacted similarly to the plasma potential and ion energy when operating conditions were varied. Increased input power had negligible effect on electron temperature, but increases in pressure caused both components of T_e to decrease. The perpendicular component of T_e was greater than the parallel component near the ECR region, but the two temperatures equilibrated as the plasma moved away from the thruster. Since the plasma potential and electron temperature increase as the pressure decreases, the ion velocity would increase for the ECR thruster in an improved vacuum facility or space environment.

Measurements of transmitted and reflected microwave power were completed. For the transmission studies a microwave antenna was mounted on the diagnostic arm, and microwave absorber was positioned inside the vacuum tank to prevent distortion due to reflection from the tank. The absorption material raised the tank pressure due to outgassing. The microwave power measured at the antenna was higher than expected in the presence of the plasma. The plasma may focus additional microwave power to the antenna. As a result of the increased pressure and excessive power density measurements, the transmission data are useful only qualitatively. Despite these limitations, the results showed that as the propellant flow rate increases, a smaller percentage of the input microwave power is transmitted to the antenna. At high flow rates it appears that only a small fraction of the microwave beam is transmitted through the ECR region.

The reflection of microwave power was measured during thruster operation at a directional coupler in the waveguide. At low pressures and flow rates, less than 5% of the input power was reflected back through the waveguide, but as the propellant flow rate, and therefore pressure, increased, a sharp increase in reflection occurred at approximately 1×10^{-4} torr. As the pressure increased above this level, the reflected power reached more than 20% of the input power. It may be that the plasma frequency reaches the microwave frequency at 1×10^{-4} torr. Considering the results of both

studies, it seems likely that much of the microwave power is not absorbed by the plasma in the ECR region. Since much of the power is reflected from the plasma at high flow rates, and since the energy of the plasma is not noticeably affected by the increase in reflection, it seems that transmission through the plasma at low flow rates may be similar to the maximum amount reflected at high flow rates. In view of these results, it seems likely that inefficient absorption of microwave power accounts for significant energy loss.

Plasma detachment from the magnetic nozzle was identified as a critical issue for ECR and other applied-field thrusters [25, 37, 18]. To investigate detachment and plume divergence, a simplified collisionless model was used to calculate the trajectories of plasma rings. The code predicted that the plasma will detach under certain conditions and that the acceleration due to the force on the electrons' dipole moments is inconsequential to the plasma trajectory. It was shown that electron inertia is the mechanism for collisionless detachment (See Appendix A). The parameter G was identified as a useful non-dimensional parameter which helps determine whether the plasma will detach. The radii of 90° deflection were calculated for several plasma initial conditions, and it was shown that the nozzle configuration can be manipulated to reduce beam divergence and increase the useful radius of the thruster. Detachment of the plasma is still seen as a critical obstacle for ECR and other thrusters. This collisionless analysis must be augmented by experiments to determine the effect of collisional processes on plasma trajectories.

An attempt was made to experimentally verify the collisionless model using an ion thruster in an applied magnetic nozzle. The ion kinetic energy could then be fixed, and the magnetic field could be varied independently of the ion energy. The grids of the thruster were masked to extract only a thin ring of plasma coaxial with the magnetic nozzle. The ion flux density profile was then measured to determine the effect of the magnetic field on the trajectory of the annular plasma. Contrary to expectations, instead of deflecting the plasma away from the axis, the magnetic

field caused the annulus to spread and decrease in radius. A radial electric field was established in presence of magnet that directed the ions away from the plasma ring. The lower energy ions in particular were deflected out of the well-defined plasma annulus. It is believed that the radial electric field developed because the applied magnetic field hindered neutralization of the ion beam. The effects of the magnetic nozzle were reduced when the pressure increased. The experiment did not satisfy its goal of providing insight into plasma detachment from a magnetic nozzle, but the data exposed some interesting effects of a magnetic nozzle on an externally-neutralized annular ion beam.

6.2 Suggestions for Possible Future Work

The laboratory device proved to be an inefficient thruster. However, further studies are needed to fully evaluate ECR thrusters for spacecraft propulsion. Studies at low pressures would be particularly useful to eliminate the effects of the surrounding background neutrals. The annular flow exhibited at low pressures deserves further inquiry, and the microwave absorption conditions should be studied at lower pressures. Detachment of the plasma from the magnetic nozzle is still seen as a major issue for applied-field thrusters. However, experimental verification of detachment conditions may be difficult because of the size of the vacuum tank needed to observe detachment.

Overall, it appears unlikely that ECR thrusters will play a role in space propulsion in the near future. Electrostatic and electrothermal thruster have developed sufficiently that they may soon be used in many applications. Electromagnetic devices such as the SPT and TAL (Anode Layer Thruster) are also extremely attractive for near-term application. The development of these technologies is of more urgent concern. However, the question of lifetime remains for all thrusters with electrodes, especially for long-term interplanetary missions.

For the long term development of ECR for propulsion, a fundamental understand-

ing of the detachment process is required. Since experimental investigations may be impractical, a logical next step would be to model a plasma beam in a magnetic nozzle using a three-fluid code (See Appendix B) which could capture the electrical resistivity and fluid friction effects on plasma detachment.

Appendix A

Lagrangian Analysis of Collisionless Plasma Detachment [1]

Hooper has presented an analysis of plasma detachment from a magnetic nozzle, and has shown that a dimensionless parameter G (defined below) controls detachment behavior in the cold-plasma, collisionless limit [18]. Here we review the physics which gives rise to collisionless plasma detachment, and show that the importance of the G parameter can be seen from considerations of energy and canonical momentum conservation.

Consider an axisymmetric magnetic nozzle as shown in Figure A-1, and a ring of plasma created at r_0 and z_0. Following Hooper [18], we neglect acceleration forces and simply start the plasma with a velocity $\mathbf{u}_0$ along $\mathbf{B}$. (For the ECR thruster, trajectory calculations discussed below show that acceleration occurs primarily early in the trajectory, before separation begins.) The initial plasma azimuthal velocity is zero, and we assume that the Debye length is small, and that collisions may be neglected. We also assume there are no cross-field radial or axial currents flowing ($j_r = j_z = 0$).

[1] Based on unpublished notes by D. Goodwin, 1992.

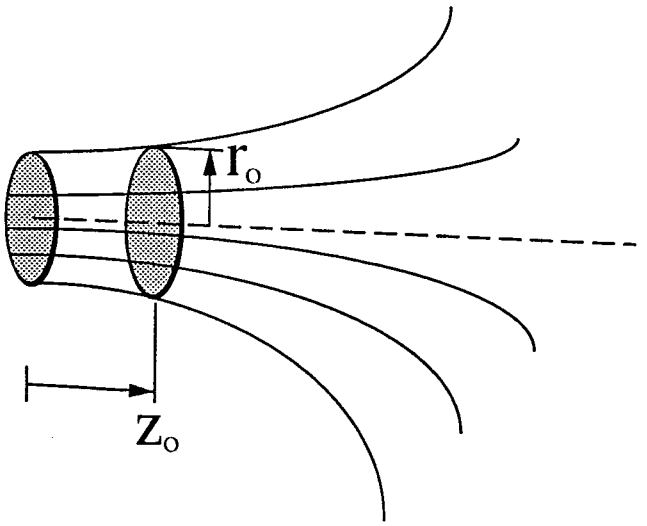

Figure A-1: Magnetic nozzle.

The Lagrangian for a single charged particle in a specified electromagnetic field is

$$L(\mathbf{r}, \dot{\mathbf{r}}, t) = \frac{1}{2} m \dot{\mathbf{r}}^2 - e\Phi(\mathbf{r}, t) + e\dot{\mathbf{r}} \cdot \mathbf{A}(\mathbf{r}, t), \tag{A.1}$$

where $\mathbf{r}$ is the particle's position, m is its mass, $\mathbf{A}$ is the vector potential, and Φ is the scalar potential. We will assume that there are N electrons and N ions, distributed uniformly over the ring, which interact only through the local space charge field. Furthermore, since $B_\theta = 0$ and $\mathbf{B} = \nabla \times \mathbf{A}$, only A_θ is non-zero. Then the total Lagrangian for the N electrons is

$$L_e = \frac{N}{2} m_e (u_r^2 + u_\theta^2 + u_z^2) + Ne\Phi - Neu_\theta A_\theta, \tag{A.2}$$

where u_r, u_θ, and u_z are the radial, azimuthal and axial components of velocity, respectively. None of the quantities u_r, u_θ, u_z, Φ, or A_θ depend explicitly on θ. Therefore, the Lagrangian is independent of θ (i.e., θ is a cyclic coordinate). The

canonical momentum conjugate to any cyclic coordinate is a constant of the motion, so $p_{\theta,e} = \partial L_e/\partial\dot{\theta}$ is constant. Now $u_\theta = r\dot{\theta}$, so the canonical angular momentum

$$p_{\theta,e} = m_e r^2\dot{\theta} - erA_\theta \tag{A.3}$$

is conserved as the electrons move.

Introducing a magnetic flux function $\Psi = rA_\theta$, we have

$$B_r = -(1/r)(\partial\Psi/\partial z) \tag{A.4}$$

and

$$B_z = (1/r)(\partial\Psi/\partial r), \tag{A.5}$$

and the flux threading the plasma loop is $2\pi\Psi$.

We may rewrite Eq. (A.3) as

$$p_{\theta,e} = m_e r u_{\theta,e} - e\Psi. \tag{A.6}$$

If we denote Ψ at (r_0, z_0) by Ψ_0, then conservation of canonical angular momentum gives [since $u_{\theta,e}(r_0, z_0) = 0$]

$$m_e u_{\theta,e} = -e(\Psi_0 - \Psi)/r. \tag{A.7}$$

Similarly for the ions, we may write an analogous Lagrangian (substituting e for $-e$ and M_i for m_e), and derive an equivalent expression for $u_{\theta,i}$:

$$M_i u_{\theta,i} = e(\Psi_0 - \Psi)/r. \tag{A.8}$$

Adding these equations, we have

$$m_e u_{\theta,e} + M_i u_{\theta,i} = 0. \tag{A.9}$$

Eqs. (A.7) and (A.8) show that an azimuthal current density $j_\theta = e(u_{\theta,i} - u_{\theta,e}) \approx -eu_{\theta,e}$ must be generated if the plasma crosses the flux surface. This current generates a centrifugal $\mathbf{J} \times \mathbf{B}$ restoring force, which hinders separation. Eq. (A.7) shows that if $m_e = 0$ (as assumed in ideal MHD), then these $\mathbf{J} \times \mathbf{B}$ forces hold the plasma to the flux surface, since then the only possible trajectories are those for which $\Psi = \Psi_0$.

However, non-zero m_e allows trajectories with $\Psi \neq \Psi_0$ to exist. Thus, collisionless plasma detachment may be attributed to electron inertia effects. Another mechanism arises if the plasma has a finite resistivity (resistive MHD). Schoenberg and co-workers [31] have recently analyzed the case of resistive plasma separation.

Since the fields in the Lagrangian are time-independent, the Hamiltonian of the system is also the total energy, and is a constant of the motion. For this system the Hamiltonian is simply the total kinetic energy of the electrons and ions:

$$H = \frac{N}{2}\left[(m_e + M_i)(u_r^2 + u_z^2) + m_e u_{\theta,e}^2 + M_i u_{\theta,i}^2\right] \tag{A.10}$$

Substituting for the azimuthal velocities from Eqs. (A.7) and (A.8), we have

$$H = \frac{N}{2}(m_e + M_i)\left[u_r^2 + u_z^2 + \frac{e^2}{m_e M_i r^2}(\Psi_0 - \Psi)^2\right] \tag{A.11}$$

Defining a non-dimensional meridional velocity by $v^2 = (u_r^2 + u_z^2)/u_0^2$, and a non-dimensional flux function $\psi = \Psi/\Psi_0$, we may write the Hamiltonian as

$$H = \frac{N}{2}(m_e + M_i)u_0^2\left[v^2 + G\frac{(1-\psi)^2}{(r/r_0)^2}\right], \tag{A.12}$$

where

$$G = \frac{e^2\Psi_0^2}{m_e M_i r_0^2 u_0^2}. \tag{A.13}$$

The non-dimensional parameter G, first introduced by Hooper [18], is a fundamental parameter governing collisionless plasma detachment from a magnetic field. Since the total kinetic energy is conserved, the term in brackets in Equation (A.12)

must be unity. Thus, since $v \leq 1$, it is clear that as $G \rightarrow \infty$, $\psi \rightarrow 1$ and no detachment can occur. However, as we show in Chapter 4, there is no unique G value above which detachment cannot occur; instead, the largest G value at which detachment occurs depends strongly on r_0 and the field configuration, and in fact for small r_0 even $G > 10^7$ can result in separation from the magnetic nozzle.

Appendix B

Resistive Detachment Simulations with the Mach2 MHD Code

Here we describe modeling efforts using the MHD simulation code, Mach2, written by Mission Research Corporation [33, 12]. Several modifications to the original code have been made to accommodate the magnetic nozzle of a current loop and to enable the JPL Cray to compile the extensive code. The goal of this work was to simulate the annular plasma flow observed at low pressures in Section 3.1 and to evaluate whether increased resistivity at higher pressure is sufficient to cause the ion flux to be maximum at the thruster axis or whether other processes are involved. Unfortunately, the code was not properly suited to this application, and the results did not satisfy the goals of the work.

B.1 Mach2 MHD Code

The Mach2 code is a two-dimensional MHD simulation program which calculates three components of velocity while allowing plasma parameters to vary in only two dimensions. The simulation region may have either planar or axisymmetric geometry. It is convenient for use on complex geometries because the calculation region is determined by an input file, and no program modifications are needed to change the configuration. The code sets the calculation mesh sizes and computation timestep in

the problem domain to ensure that errors are within user-specified limits.

Mach2 is a single-fluid MHD code which assumes local thermal equilibrium, meaning that ions, electrons, and neutrals are constrained to have the same temperature. The plasma is modeled as quasi-neutral and has several models for the ionization fraction. Three components of vector quantities are calculated, but no quantity is allowed to vary in the direction perpendicular to the computational plane or azimuthal direction for planar and axisymmetric simulations, respectively. The fluid is modeled as compressible, and an ideal gas equation of state is used [33]. Analytic models calculate electrical resistivity, thermal conductivity, and other transport quantities. The code was designed to use tabular models based on the *SESAME* tables at Los Alamos National Laboratory for much of the physics, but these tables were unavailable for the simulations presented here.

The geometry and some of the physics for each problem are controlled by an input file (See Appendix C) which is read by Mach2 at the beginning of the simulation. The user is able to set many physics and computational variables. The geometry is specified by defining the corners of several blocks which make up the problem region. Results are returned in output files in graphic and numerical format. The time and spatial frequency of the output is specified by the user. The physics and calculation mesh generation characteristics are described in detail in the Mach2 manual [33].

B.2 Results of the Simulations

The intent of the Mach2 simulations was to model the annular flow observed at low pressures in Section 3.1. It was hoped that the code would provide some insight into the mechanism which caused the annular flow to disappear at higher pressures. The input file shown in Appendix C was created to model an axisymmetric plasma jet entering a region with a background density similar to that in the laboratory experiments on the ECR thruster. The simulated plasma jet had the same initial

radius as the ECR plasma, and the data from the ECR experiments were used to set the plasma conditions in the input file. The initial jet velocity was 350 m/s, and the code accelerated the flow. The shape of the computational zone (The jet entered a region bounded by a 0.5 m radius $\times$ 0.5 m long cylinder which expanded to a 1 m radius $\times$ 0.5 m long cylinder.) was defined to approximate the geometry of the vacuum tank in the laboratory. The magnetic field of a current loop was imposed on the calculation region coaxially to the plasma jet using the same method described in Chapter 4, and the current and radius were chosen so that the magnetic field was similar to that in the experiments.

The calculated mass density contours for the lower pressure simulation ($P \approx 5 \times 10^{-5}$ torr) are shown in Figure B-1. The figure is an axisymmetric view with the plasma jet entering the region in the bottom left portion of the figure. The axis of the region is the vertical line on the left. The flow direction of the plasma jet is from bottom to top. As the figure shows, the density is greatest near the plasma jet, and the density decreases as the plume diverges in to the vacuum region. The density profile is maximum on the axis and is similar to the ion flux profiles seen in Section 3.1 for the higher pressure cases. Since an annular flow was not initiated in this simulation, the annular flow displayed in the experiment was not anticipated here. The density variations away from the plasma jet are assumed to be numerical errors. Several attempts failed to eliminate such errors in this and other simulations.

In Figure B-2 the calculated temperature contours for the plasma jet are shown. The plume can be seen as the region of high temperature to the left of the figure. As expected and as observed in the experiments, the temperature decreases away from the plasma initiation region in the axial and radial directions. The ionization fraction of the plasma is set to be linear in the temperature. The region of temperature variation near the boundary outside the plasma plume is again assumed to be due to numerical error. We were unable to eliminate these errors in temperature, and in some

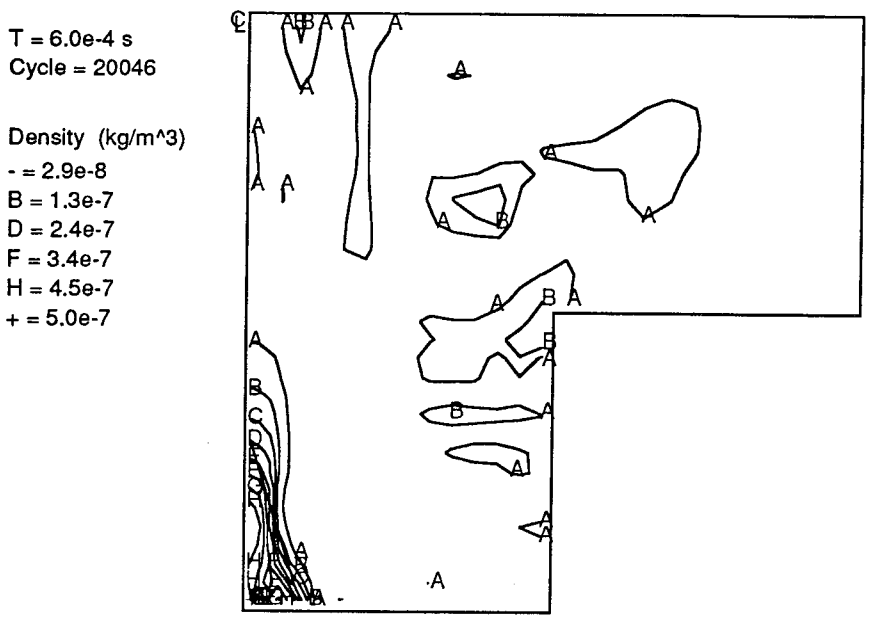

Figure B-1: Calculated density contours for uniform plasma jet.

simulations the errors grew sufficiently over the simulation duration to obscure the plasma plume. The errors typically originated at the boundaries of the computational space.

The calculated meridional velocity vectors are shown in Figure B-3. The size of the vectors is proportional to the velocity. Near the magnet current loop at the bottom of the computation region, the velocity vectors curve around the point of maximum magnetic field. Note the high velocity in the positive radial direction at the bottom of the figure along the boundary. The velocity here is greater than could be attained by ions in a plasma jet with an initial temperature of 13 eV and an initial velocity of 350 m/s. The kinetic energy of the ions traveling at the maximum calculated velocity in Figure B-3 would be 1.4×10^4 eV. We were unable to correct this elevated velocity at the boundary. When simulations were conducted with a higher background density, the maximum velocity decreased at the lower boundary. Another problem with the calculated velocities is that the streamlines do not follow

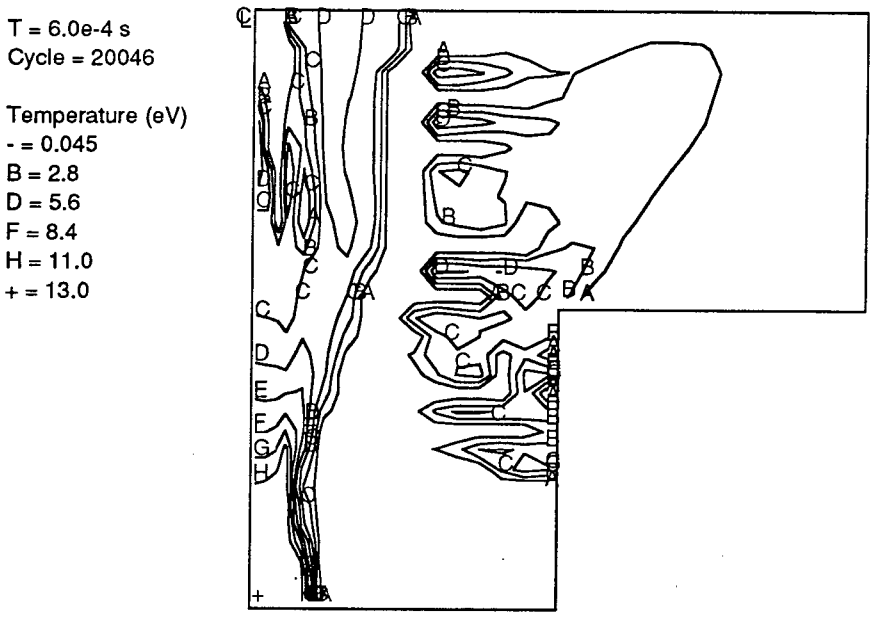

Figure B-2: Calculated temperature contours for uniform plasma jet.

the magnetic field lines even when the plasma electrical resistivity is set to zero. The suspected reasons for these problems is discussed below.

A plot of magnetic field lines is shown in Figure B-4. Although the same program was used to calculate the field lines for this figure as in Chapter 4, the field lines here are distorted at the boundaries. In addition the "A" and "B" lines enclose a negative magnetic flux. It appears that the magnetic boundary conditions change the applied magnetic field. The Mach2 code was originally used to model transient problems with a duration of a few microseconds, and the magnetic boundary conditions are such that they prevent the magnetic field from penetrating the boundaries. Mikellides claims that while these boundary conditions are acceptable short duration problems, for steady-state problem such the simulation attempted here, such boundary conditions are not appropriate [28].

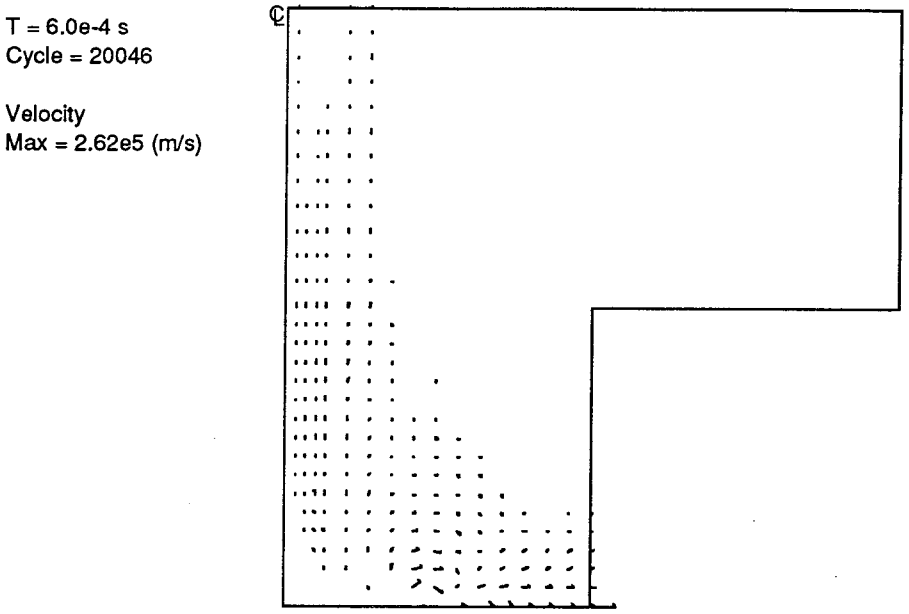

Figure B-3: Calculated velocity vectors for uniform plasma jet.

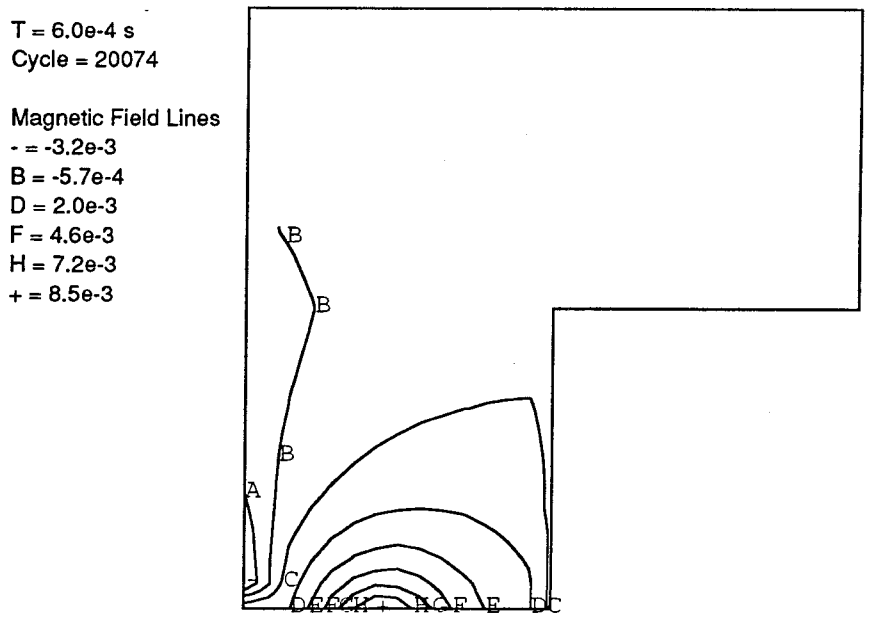

Figure B-4: Calculated magnetic field lines displaying distortion at boundaries.

B.3 Conclusions

Due to the errors noted in the results shown above, it appears that Mach2 is unsuitable for this application. The magnetic boundary conditions seem to be a likely cause for some of the problems experienced with the code. The distortion of the field lines at the boundaries may cause the plasma velocity to deviate from the original magnetic field because of the change in magnetic flux near the axis of the plasma jet. The aberrant radial velocity experienced at the bottom boundary may also be a result of the distorted magnetic field. Others have had similar problems with the magnetic boundary conditions for steady state simulations [28].

The nature of the code may also contribute to the errors. Only thermal energy is conserved at the boundaries. For this reason, the code is not designed to model plasmas with significant kinetic energy. Also, because Mach2 is a single-fluid thermal equilibrium code, ions, electrons, and neutrals have the same temperature and radial and axial velocity. In a real ECR plasma, the plume is only weakly ionized, and the ions and neutrals have different velocities. It is also expected that the electrons and ions in the laboratory plasma are not in thermal equilibrium.

The analytic physics models may also be inaccurate in this application. The electrical and thermal conductivity greatly affect the plasma trajectories [31], and the models for these quantities in Mach2 assume thermal equilibrium. The ionization fraction is necessarily higher in the model, and there is no means to conserve the flux of ions due to the ionization model which depends on temperature alone. For an estimate of the ionization fraction in the real plasma, we can calculate an approximate ion density using a typical measured ion current from Section 3.1 and a typical ion energy from Section 3.2. For a plasma plume with 20 eV ions and an ion current of 5×10^{-4} A, the plasma density is 3.2×10^{15} m^{-3}, and for the vacuum tank at 5×10^{-5} torr, the neutral density is 1.6×10^{18} m^{-3} resulting in an ionization fraction of 2.0×10^{-3}. The reason for the weak ionization in the plume is that the plasma accelerates from approximately zero axial velocity at the ECR region to 20 eV in the

plume. Assuming negligible ionization and recombination outside the ECR region, by continuity, the ionization fraction must drop as the plasma diverges into the tank.

An ideal code for modeling the ECR plasma plume would be a particle-in-cell (PIC) code which allows electrons, ions, and neutrals to interact independently. Unfortunately, because of the size of an ECR thruster, a PIC model is unrealistic due to computing time constraints. Another possibility that may be able to yield results in a reasonable time is a three fluid model which calculates the interactions among electron, ion, and neutral fluids.

Appendix C

Mach2 Input File for ECR Plasma Plume Simulations

This is the Mach2 input file used to produce the figures in Appendix B. It was adapted from the input file that appears in the Mach2 users manual [33].

```
-       Uniform plasma, linear ionization, 5e-5 torr
ecr8.4un5

!!!!!!!!!!!!!!!!!!!!!!!!!!!!!!!!!!!!!!!!!!!!!!!!!!!!!!!!!!!!!!!!!
 $contrl
! run to 200 microseconds
    twfn = 2.e-4,
! begin at time = 0
    t = 0.,
! initial and maximum timesteps
    dt = 1.0d-12,
    dtmax = 30.d-9,
! run a maximum of 60 minutes of CPU time
```

```
    imns = 3600,
! cylindrical symmetry
    cyl = 1.,
! time centering enabled
      theb = 0.5d0,
! begin setting the physics simulation switches:
    eoson = .true.,
! single material model
      con2on = .false.,
! single temperature model
    tsplit = 0,

!  maximum relative error in temperature
tdtol = 1.e-9,

! compute MHD
    hydron = .true.,

      courmax = 2.,
      rofvl = 5.d-8,

! keep temperature below 33 eV (2.4e8 J/kg) and above
! (1.855e5 J/kg) Argon, enforce cap for densities
! below 1.e99 kg/m^3
      sieflr = 1.62e5,
      siecap = 7.3e7,
      rofsiecp = 1.d99,
! artificial viscosity
```

```
      mu = 0.d0,
!  maximum relative error in hydrodynamics
      eps = 1.0d-9,

! absolute floor on the mass density
! (9.e-9 kg/m^3 is 5e-5torr @ 2.55e-2 eV)
      rof = 2.9e-8,
! don't read or write initial density file -- dndump
      idnflg = 0,
! compute an "ideal" mesh
    meshon = .true.,
      nsmooth = 4,
      wrelax = 0.25,
! no material strength model
    strength = .false.,
! radiation model requires sesame tables
    radiate = .false.,
! thermal diffusion
    thmldif = .true.,
! include anisotropic thermal conduction due to magnetic fields
    anisot = .true.,
!  factor limiting thermal flux
       flxlmt = 0.,

! method of iteration on hydro and temperature
mgmode = 'vcycle',
mgmodet = 'vcycle',
```

```
! no external circuits are connected to the problem domain
    ciron = .false.,
! magnetic fields exist...
    magon = .true.,

      brbzon = .true.,
      itpot = 4,
      potrelx = 0.1,

! magnetic diffusion
      bdiff = .true.,
! vacuum resistivity model: set the electric diffusivity to 10^5 m^2/s
!  in all cells for which the density is below 5.e-8 kg/m^3
      aresvac = 7.5d4,
      rofanom = 5.d-8,

      jouhtmlt = 0.,
      rofjoule = 5.d-8,
      rdrelax = 0.5d0,
      rdtol = 1.0d-6,

! use multigrid for solving the diffusion equation
    multgrd = .true.,

! Hall effect on
    hallon = .true.,

! coil radius in meters for calculation of magnetic field in bfield
```

```
     scrtch(1) = 0.23,
! coil current in Amps for calculation of magnetic field in bfield
     scrtch(2) = 29425.,

 $end

!!!!!!!!!!!!!!!!!!!!!!!!!!!!!!!!!!!!!!!!!!!!!!!!!!!!!!!!!!!!!!!!
 $ezgeom
!  define corners of blocks
    nblk = 5,
    npnts = 11,
    pointx(1) = 0.0,
    pointy(1) = 0.05,
    pointx(2) = 0.064,
    pointy(2) = 0.05,
    pointx(3) = 0.5,
    pointy(3) = 0.05,
    pointx(4) = 0.0,
    pointy(4) = 0.55,
    pointx(5) = 0.064,
    pointy(5) = 0.55,
    pointx(6) = 0.5,
    pointy(6) = 0.55,
    pointx(7) = 1.0,
    pointy(7) = 0.55,
    pointx(8) = 0.0,
    pointy(8) = 1.05,
    pointx(9) = 0.064,
```

```
    pointy(9) = 1.05,
    pointx(10) = 0.5,
    pointy(10) = 1.05,
    pointx(11) = 1.0,
    pointy(11) = 1.05,

    corners(1,1) = 4,5,2,1,
    corners(1,2) = 5,6,3,2,
    corners(1,3) = 8,9,5,4,
    corners(1,4) = 9,10,6,5,
    corners(1,5) = 10,11,7,6,

 $end

!!!!!!!!!!!!!!!!!!!!!!!!!!!!!!!!!!!!!!!!!!!!!!!!!!!!!!!!!!!!!!!!!!!!!!!
 $ezphys
! specify the global physics model
! argon EOS including the low-density values derived by MRC
    matnameg = 'ar-mrc  ',
      ang = .8,
      awg = 40.,
! initial density in kg/m^3, 9.e-9 @ 5e-5 torr, 2.55e-2 eV
    roig = 2.9e-8,
! initial temperature in eV
    tempig = 0.0255,
! ideal gas EOS
    eosmodlg = 'idealgas',
```

```
! linear ionization model
      nfemodlg = 'linear',
! ionization state below tvapg
      nfeig = 1.e-99,
! temperature that ionization starts
tvapg = .2,
! temperature for full ionization
tionizeg = 16.,

! use current loop for magnetic flux, see the end of the "contrl"
! namelist for coil radius and current
      binitg = 'curloop',

! Eulerian (stationary) grid relaxed 99% to ideal grid
gdvlg = 0.99,

! concentrate grids in regions of high density and velocity
      velgrwtg = 1.0,
      dnsgrwtg = 1.0,

! van Leer transport
    donorg = .false.,
! electron-ion electron-neutral collisions used to calculate
!       resistivity
    resmodlg = 'neutral ',
! plus anomalous resistivity
    arsmodlg = 'omegape ',
```

```
! radiation model requires sesame tables
    radmodlg = 'none    ',
 $end

!!!!!!!!!!!!!!!!!!!!!!!!!!!!!!!!!!!!!!!!!!!!!!!!!!!!!!!!!!!!!!!!!!!!!!!!!!!
 $output
! time between writing plots
    dtp = 1.e-4,
! time between writing data to number
    dtn = 2.e-4,
! time between restart dumps
    dtrst = 2.e-4,
! cycle interval between writing data to history file
        ncychist = 6600,

! the plot-region of each block
    kpltreg(1) = 1,
    kpltreg(2) = 1,
    kpltreg(3) = 1,
    kpltreg(4) = 1,
    kpltreg(5) = 1,

! log scaling of contours
    contyp = 'linear',

! print one-sided plots
    pflip = .false.,
!internal block boundaries are not drawn
```

```
    intbound = .false.,

! number of contour levels
    kcon(1) = 10,
! vector scaling factor
    vsclmlt(1) = 0.05,
! true scaling
    pltscale = 'none    ',

!!!!!!!!!!!!! PLOTS !!!!!!!!!!!!!!!!!!!!!!!!!!!!!!!!!!!!!!!!!!!!
fichfram = 21,

    plot(1)  = 'velocity',
    plot(2)  = 'speed   ',
    plot(3)  = 'velocity',
plottype(3) = 'contour',
plotcomp(3) = 'vectory',

    plot(4)  = 'te      ',
    plot(5)  = 'sie     ',
    plot(6)  = 'nfe     ',
    plot(7)  = 'lumnosty',

    plot(9)  = 'bline   ',
    plot(10) = 'accelb  ',
    plot(11) = 'ecyclo  ',

    plot(12) = 'pressure',
```

```
     plot(13) = 'totpress',


     plot(14) = 'momden  ',
     plot(15) = 'momden  ',
 plottype(15) = 'contour',
 plotcomp(15) = 'vectory',
     plot(16) = 'kinden  ',

     plot(17) = 'density ',
     plot(18) = 'ni      ',
     plot(19) = 'ne      ',

     plot(20) = 'diffusiv',
     plot(21) = 'debyel  ',
!!!!!!!! END PLOTS !!!!!!!!!!!!!!!!!!!!!!!!!!!!!!!!!!!!!!!!!!!!

      intty(1) = 'timencyc',
      intty(2) = ',100;tim',
      intty(3) = 'estep,10',
      intty(4) = '0;enrgyn',
      intty(5) = 'ow,100;p',
      intty(6) = 'erform,1',
      intty(7) = '00;badce',
      intty(8) = 'lls,100;',
      intty(9) = 'blank,10',
     intty(10) = '0       ',
 $end
```

```
!!!!!!!!!!!!!!!!!!!!!!!!!!!!!!!!!!!!!!!!!!!!!!!!!!!!!!!!!!!!!!!!!!
 $inmesh

! block number 1
    icells(1) = 4,
    jcells(1) = 16,

!apply injection bc last
      ibcseq(1,1) = 4,2,1,3,

! inject flow into tank
velbc(3,1) = 'specfied',
probc(3,1) = 'specfied',
      hydbc(4,1) = 'axis',

! temperature of inflowing gas in eV
        tflow(3,1) = 13.,
! density of inflowing gas in kg/m^3
        roflow(3,1) = 3.5e-8,
! velocity of inflowing gas in m/s
        vflow(3,1) = 350.,

magzbc(3,1) = '        ',
magzbc(4,1) = 'axis    ',

magxybc(3,1) = '        ',
magxybc(4,1) = 'axis    ',
```

```
! thermal bc for axis
      thrmbc(4,1) = 'axis    ',

!!!!!!!!!!!!!!!!!!!!!!!!!!!!!!!!!!!!!!!!!!!!!!!!!
! block number 2
    icells(2) = 12,
    jcells(2) = 16,

velbc(2,2) = 'none    ',
probc(2,2) = 'contnutv',
      hydbc(3,2) = 'wall',

magzbc(2,2) = '        ',
magzbc(3,2) = '        ',

magxybc(2,2) = '        ',
magxybc(3,2) = '        ',

!!!!!!!!!!!!!!!!!!!!!!!!!!!!!!!!!!!!!!!!!!!!!!!!!!!!!!!!!!!!!!!!!
! block number 3
    icells(3) = 4,
    jcells(3) = 12,


velbc(1,3) = 'none    ',
probc(1,3) = 'contnutv',
      hydbc(4,3) = 'axis',
```

```
magzbc(1,3) = '        ',
magzbc(4,3) = 'axis    ',

magxybc(1,3) = '        ',
magxybc(4,3) = 'axis    ',

! thermal bc for axis
      thrmbc(4,3) = 'axis    ',

!!!!!!!!!!!!!!!!!!!!!!!!!!!!!!!!!!!!!!!!!!!!!!!!!!!!!!!!!!!!!!!!!
! block number 4
    icells(4) = 12,
    jcells(4) = 12,

velbc(1,4) = 'none    ',
probc(1,4) = 'contnutv',

magzbc(1,4) = '        ',
magxybc(1,4) = '        ',

!!!!!!!!!!!!!!!!!!!!!!!!!!!!!!!!!!!!!!!!!!!!!!!!!!!!!!!!!!!!!!!!!
! block number 5
    icells(5) = 12,
    jcells(5) = 12,

velbc(1,5) = 'none',
probc(1,5) = 'contnutv',
```

```
velbc(2,5) = 'none    ',
probc(2,5) = 'contnutv',
velbc(3,5) = 'none    ',
probc(3,5) = 'contnutv',

magzbc(1,5) = '        ',
magzbc(2,5) = '        ',
magzbc(3,5) = '        ',

magxybc(1,5) = '        ',
magxybc(2,5) = '        ',
magxybc(3,5) = '        ',

 $end
!!!!!!!!!!!!!!!!!!!!!!!!!!!!!!!!!!!!!!!!!!!!!!!!!!!!!!!!!!!!!!!!!!!!!!!!!!
```

References

[1] Courtesy of the Advanced Propulsion Technology Group, Jet Propulsion Laboratory.

[2] Electric propulsion. *Aerospace America*, 41(12):52, December 1993.

[3] Olin aerospace company innovative arcjet propulsion successful on AT&T's new Telstar 401 satellite. Olin News, March 1994.

[4] C. Bohm and J. Perrin. Retarding-field analyzer for measurements of ion energy distributions and secondary electron emission coefficients in low-pressure radio frequency discharges. *Review of Scientific Instruments*, 64(1):31–44, January 1993.

[5] J.R. Brophy. Stationary plasma thruster evaluation in russia. Summary Report JPL 92-4, NASA-Jet Propulsion Laboratory, March 1992.

[6] J.R. Brophy, C.E. Garner, and L.C. Pless. Personal communcation.

[7] J.R. Brophy, L.C. Pless, J. Mueller, and J.R. Anderson. Operating characteristics of a 15 cm dia. ion engine for small planetary spacecraft. 23rd International Electric Propulsion Conference, 1993. IEPC-93-110.

[8] F.F. Chen. *Plasma Diagnostic Techniques*, chapter Electric Probes. Academic Press, 1965.

[9] F.F. Chen. *Introduction to Plasma Physics and Controlled Fusion.* Plenum Press, 1984.

[10] G.F. Crimi. *Investigation of a Microwave Generated Plasma in a Non-Uniform Magnetic Field.* Ph.D. thesis, University of Pennsylvania, 1967.

[11] M. Dahimene and J. Asmussen. The performance of a microwave ion source immersed in a multicusp static magnetic field. *Journal of Vacuum Science and Technology*, B 4(1):126–130, Jan./Feb. 1986.

[12] M.H. Frese. Mach2: A two-dimensional magnetohydrodynamics simulation code for complex experimental configurations. Technical Report AMRC-R-874, Mission Research Corporation, Albuquerque, NM, September 1986.

[13] R.A. Gerwin, G.J. Marklin, A.G. Sgro, and A.H. Glasser. Characterization of plasma flow through magnetic nozzles. Technical Report AL-TR-89-092, Air Force Astronautics Laboratory, 1990.

[14] H. Hendel, T. Faith, and E.C. Hutter. Plasma acceleration by electron cyclotron resonance. Technical Report 2, RCA Review, June 1965.

[15] N. Hershkowitz. *Plasma Diagnostics*, chapter How Langmuir Probes Work, pages 113–183. Academic Press, Inc., San Diego, 1989.

[16] A.C. Hindmarsh. ODEpack, a systematized collection of ODE solvers. In R. S. Stepleman et al., editors, *Scientific Computing*, pages 55–64. North-Holland, Amsterdam, 1983.

[17] E.B. Hooper. Plasma detachment from a magnetic nozzle. AIAA/SAE/ASME 27th Joint Propulsion Conference, 1991. AIAA-91-2590.

[18] E.B. Hooper. Plasma detachment from a magnetic nozzle. *Journal of Propulsion and Power*, 9(5):757–763, Sept./Oct. 1993.

[19] E.B. Hooper et al. Analysis and experiments of a whistler-wave plasma thruster. 23rd International Electric Propulsion Conference, September 1993. IEPC-93-038.

[20] J. Hopwood et al. Langmuir probe measurements of a radio frequency induction plasma. *Journal of Vacuum Science Technology*, 11(1):152–156, Jan./Feb. 1993.

[21] J.D. Jackson. *Classical Electrodynamics*. John Wiley and Sons, New York, 2nd edition, 1975.

[22] R.G. Jahn. *Physics of Electric Propulsion*. McGraw-Hill, Inc., New York, 1968.

[23] D.A. Kaufman and D.G. Goodwin. Experimental studies of an ECR plasma thruster. AIAA 29th Joint Propulsion Conference, June 1993. AIAA 93-2108.

[24] D.A. Kaufman, D.G. Goodwin, and J.C. Sercel. Plasma separation from magnetic field lines in a magnetic nozzle. AIAA 31st Aerospace Sciences Conference, 1993. AIAA-93-0817.

[25] H.G. Kosmahl. Three-dimensional plasma acceleration through axisymmetric diverging magnetic fields based on dipole moment approximation. Technical Note NASA TN D-3782, NASA, 1967.

[26] B. Lipschultz, I. Hutchinson, B. LaBombard, and A. Wan. Electric probes in plasmas. *Journal of Vacuum Technology*, 4(3), May/June 1986.

[27] J.A. Martin and R.A. Wallace. Columbus - to Mars with solar-electric propulsion. *Journal of Spacecraft and Rockets*, 31(2):341–342, 1994.

[28] P.G. Mikellides and P.J. Turchi. Application of the Mach2 code to magnetoplasmadynamic arcjets. AIAA 28th Joint Propulsion Conference, July 1992. AIAA 92-3740.

[29] D.B. Miller, G.W. Bethke, and G.F. Crimi. Investgation of a microwave generated plasma in a non-uniform magnetic field. Final report, NASA, 1965. NASA CR-54746.

[30] C.O. Morain, P. O'Keeffe, S. Den, and Y. Hayashi. Large-diameter plasma profile monitoring system using Faraday cup and Langmuir probe arrays. *Measurement Science Technology*, pages 1484–1488, 1993.

[31] R.W. Moses, Jr., R.A. Gerwin, and K.F. Schoenberg. Resistive plama detachment in nozzle based coaxial thrusters. *AIP Conference Proceedings 246*, 1992. 9th Symposium, Space Nuclear Power Systems.

[32] R.M. Perez. Personal communcation.

[33] R.E. Peterkin, Jr. et al. *Mach2: A Reference Manual.* Mission Research Corporation, Albuquerque, NM, 5 edition, 1991.

[34] S. Samukawa, Y. Nakagawa, and K. Ikeda. Ion current density and ion energy distributions at the electron cyclotron resonance position in the electron cyclotron resonance plasma. *Japanese Journal of Applied Physics*, 30(2):423–427, February 1991.

[35] S. Samukawa, T. Nakamura, T. Ishida, and A. Ishitani. Uniform electron cyclotron resonance plasma generation for precise ULSI patterning. *Japanese Journal of Applied Physics*, 31(6B):774–776, June 1992.

[36] J.C. Sercel. Electron cyclotron resonance (ECR) plasma thruster research. AIAA/SAE/ASME 24th Joint Propulsion Conference, 1988. AIAA-88-2916.

[37] J.C. Sercel. A simple model of plasma acceleration in a magnetic nozzle. AIAA/DGLR/JSASS 21st International Electric Propulsion Conference, 1990. AIAA-90-2597.

[38] J.C. Sercel. *An Experimental and Theoretical Study of the ECR Plasma Engine Concept.* Ph.D. thesis, California Institute of Technology, 1993.

[39] J.C. Sercel and D.J. Fitzgerald. ECR plasma thruster research: Preliminary theory and experiments. AIAA/ASME/SAE/ASEE 25th Joint Propulsion Conference, 1989. AIAA-89-2379.

[40] J.R. Stone and G.L. Bennett. The NASA low thrust propulsion program. NASA Technical Memorandum 102065, NASA Headquarters, 1989. AIAA 89-2492.

[41] J.D. Vedder, J.L. Tabor, and D.C. Rustin. Orbital debris hazard for nuclear electric propulsion earth-escape trajectories. *Journal of Astronautical Sciences*, 41(3):299–317, 1993.

[42] P.J. Wilbur, R.G. Jahn, and F.C. Curran. Space electric propulsion plasmas. *IEEE Transactions on Plasma Science*, 19(6):1167–1179, December 1991.

[43] J.L. Wilson, J.B.O. Caughman II, P.L. Nguyen, and D.N. Ruzic. Measurments of time varying plasma potential, temperature, and density in a 13.56 Mhz radio-frequency discharge. *Journal of Vacuum Technology*, 7(3), May/June 1989.